

# POLITECNICO DI TORINO

Master's Degree in Nanotechnologies for ICTs



Master's Degree Thesis

## Modeling the interaction of light with single-molecule junctions

Supervisors

Prof. Mariagrazia GRAZIANO

Prof. Gianluca PICCININI

Engr. Fabrizio MO

Candidate

Alberto BOTTACIN

December 2021

# POLITECNICO DI TORINO

Master's Degree in Nanotechnologies for ICTs



Master's Degree Thesis

## Modeling the interaction of light with single-molecule junctions

### **Supervisors**

Prof. Mariagrazia GRAZIANO

Prof. Gianluca PICCININI

Engr. Fabrizio MO

### **Candidate**

Alberto BOTTACIN

December 2021



*“There is a crack in everything.  
That’s how the light gets in.”*

- Leonard Cohen



# Summary

In the last years, scaling down of conventional CMOS technology decelerated due to several reasons such as increase of power density and appearance of non-idealities. Molecular electronics is one emerging nanotechnology that attracted the attention of the scientific community because molecules represent the ultimate limit of miniaturization and molecular devices are potentially faster than CMOS transistors. However, a crucial problem of this technology is the too low ON current and the great process variability that affects conduction properties. The undeniable potential of molecular electronics pushed a lot of researchers to bet on this field and one of the most theoretically studied topic is the interaction between light and molecular junctions. Studying illuminated junctions is of particular interest for several reasons. Using light it is possible to characterize process variability retrieving also additional information on vibrational activity of the junction. Moreover, Light can potentially control transport mechanisms, enhancing or suppressing determined conduction channels. In the optical frequency range, Localized Surface Plasmons (LSPs) can be excited in the electrodes, thus adding complexity to the system, but giving also the possibility to exploit other physical phenomena. The purpose of this thesis is twofold. Firstly, a literature review is provided in order to give to future readers an exhaustive introduction on this topic. Furthermore, an in depth analysis of photo-assisted tunneling (PAT) is done by considering two approximated models: Tien-Gordon and Floquet. In particular, a computationally efficient MATLAB<sup>®</sup> simulator, called EE-BESD-PAT, has been developed to implement these models. Then the results are compared to those of more sophisticated available commercial tools and are validated on experimental measurements.

The first chapter gives an introduction of the topic to the reader, justifying the reasons behind studying the interaction between light and single-molecule junctions. This field developed through different branches over the years and the most relevant ones are described. First, Raman scattering is introduced, giving essential notions to understand Raman spectroscopy. Then the sub-field of photochromic switches is described providing an accurate historical reconstruction of the studies on photoisomerization of the molecular channel. Eventually the main topic of this thesis is introduced, that is photo-assisted tunneling in single-molecule junctions with

possible localized surface plasmons excitation.

The second chapter aims to describe most studied and used models to understand photo-assisted tunneling in molecular junctions. In particular three models are presented showing their assumptions and limits of validity: Tien-Gordon, Floquet and NEGF-SCBA. The first is the simplest one, but most used in experimental papers because easier to apply. Increasing complexity, there is Floquet model, that is the most studied model for molecular wires coupled with an electromagnetic radiation in tight-binding approximation. Instead, the last model is the most complex and general based on first order Born Approximation in the frame of NEGF theory, which is implemented in the commercial software *QuantumATK* developed by SYNOPSIS®.

Eventually, the third chapter describes the implementation of Tien-Gordon and Floquet model starting from EE-BESD: an efficient and effective model for nanocomputing design, used to evaluate the current in molecular junctions with smaller computational time. Then the simulator, named EE-BESD-PAT, is validated by comparison with experimental results, obtained from a Suspended Wire Molecular Junction (SWMJ) based on octane (C8), and with *QuantumATK* simulations of a terthiophene (3TT) molecular junction. The main result of the comparison is that Floquet model performs better than Tien-Gordon one. In particular, the shape and order of magnitude predicted for 3TT junction is the same of *QuantumATK*, but with the advantage of much shorter computational time (minutes compared to days/weeks). Concerning the experimental validation, again Floquet performs better than Tien-Gordon predicting the same current enhancement of the experiment in a certain range of bias voltages.

In conclusion, this thesis gives an important introduction to the field often named ‘single-molecule optoelectronics’ and provides an efficient simulator that can be used for photocurrent prediction allowing a possible fast prototyping of optoelectronic molecular devices. Moreover EE-BESD-PAT has the potential to be embedded in a circuit level simulator, thus paving the way to photonic circuits in which some component can be a molecular device.

# Acknowledgements

Durante il periodo delle scuole medie iniziai a dire di voler diventare ingegnere nella vita, sicuramente inconscio di cosa significasse praticare questa professione. Al liceo il primo incontro con la fisica mi fece solamente intuire quanto è complesso, ma altrettanto bello il mondo in cui viviamo. Devo ringraziare il prof. V. Rampado per avermi trasmesso la passione per la matematica e la fisica che mi ha portato a scegliere come università il Politecnico di Torino, facendo così il primo passo per realizzare il ‘sogno’ che già avevo da ragazzino . Ho iniziato il primo anno della triennale di ingegneria fisica con l’intento di proseguire gli studi seguendo il corso di laurea magistrale in nanotecnologie. E così è stato. Sono giunto al termine di questo impegnativo, ma gratificante percorso e le persone da ringraziare sono moltissime. Il primo grazie va a Fabrizio, il mio correlatore, con cui periodicamente mi sono confrontato per la tesi. Ha sempre avuto le parole giuste per incoraggiarmi, ma anche commenti costruttivi che mi hanno aiutato a sviluppare il lavoro di tesi. Un ringraziamento doveroso va ai miei amici, senza i quali questi cinque anni non sarebbero stati gli stessi. Mi hanno aiutato a vivere la vita con leggerezza, senza però perdere di vista i propri obiettivi. Per questo motivo mai potrò rifiutare un caffè alle macchinette con Francesco, Claudia, Matteo, Giovanni, Alessandro, Marta, Davide, Giulio o Mary. Un grazie speciale va alla famiglia, in particolar modo ai miei genitori. Hanno sempre creduto in me, senza mai avere dubbi sulle mie scelte e sulle mie capacità. Inoltre sono coloro che più hanno dovuto sopportarmi in questi ultimi mesi coincidenti con la stesura finale della tesi. Mi scuso per il mio nervosismo quotidiano e spero che possano essere orgogliosi di me. L’ultimo grazie va all’ultima persona che è entrata nella mia vita, stravolgendola. Mi è stata vicino dal primo all’ultimo giorno di tesi, incoraggiandomi quando più ne avevo bisogno e aiutandomi concretamente nella stesura, dato che una parte delle figure presenti in questa tesi sono state realizzate da lei. Grazie Gaia per essere la mia persona girasole, indicandomi sempre dov’è la luce che illumina le bellezze della natura.



# Table of Contents

<b>List of Tables</b>	XI
<b>List of Figures</b>	XIII
<b>Acronyms</b>	XIX
<b>1 Introduction</b>	1
1.1 Raman Spectroscopy . . . . .	5
1.2 Photochromic switching . . . . .	9
1.3 Photo-assisted transport in molecular junctions . . . . .	13
1.3.1 Localized Surface Plasmons . . . . .	14
1.3.2 Indirect modulation . . . . .	18
1.3.3 Direct modulation . . . . .	20
<b>2 Photo-assisted tunneling models</b>	35
2.1 Conduction in 0D-systems . . . . .	35
2.2 Tien-Gordon model . . . . .	48
2.3 Floquet model . . . . .	62
2.4 SCBA for electron-photon interaction . . . . .	75
<b>3 Photo-assisted tunneling simulator</b>	87
3.1 EE-BESD . . . . .	87
3.2 EE-BESD-NEGF . . . . .	92
3.3 EE-BESD-PAT . . . . .	98
3.3.1 Simulation parameters . . . . .	99
3.3.2 Example: illuminated 3TT junction . . . . .	105
3.3.3 Validation . . . . .	117
<b>4 Conclusions</b>	129
<b>A Dirac formalism</b>	131

<b>B Proof of equation 2.122</b>	135
<b>Bibliography</b>	139

# List of Tables

2.1	Convention adopted by <i>QuantumATK</i> for dark current and photocurrent computation. . . . .	84
3.1	Units used to express the molecular electric dipole. . . . .	100
3.2	Total energy of 1TT, 2TT and 3TT expressed in Hartree (H) and in eV . . . . .	104
3.3	Settings used for the LCAO calculator to compute the electronic structure of 3TT junction at equilibrium. . . . .	118
3.4	Setting of “IVCharacteristics” object used to compute the <i>IV</i> curve of 3TT junction. . . . .	118
3.5	Settings of “Photocurrent” object considered to compute the current of the illuminated 3TT junction for different photon energies. . . . .	119
3.6	Setting of “IVCurve” object used to compute the <i>IV</i> curve of C8 junction. . . . .	124



# List of Figures

1.1	Example of MC-BJ exploited to perform Raman spectroscopy for studying adsorption site variability. The electrodes are deposited over a flexible substrate (in orange) making an almost point-contact conductance (ideally one atom is in common between them). A rod under the platform pushes the sample against the counter supports in order to induce stress and create the nanogap that will welcome the desired molecule (benzenedithiol in this case). Irradiating the junction (red cylinder) is possible to perform Raman spectroscopy at the same time of conductance measurements. . . . .	3
1.2	Jablonski diagram describing different scattering processes for a system having discrete energy levels (as a molecule is). In Rayleigh scattering no collective vibration (generally called “phonon”) of the molecule is involved and the scattered field has the same frequency of the incident one. In Stokes scattering the interaction with the system leads to emission of phonons that reduces the energy of the reemitted photons. On the other hand, the Anti-Stokes scattering concerns the absorption of phonons by the incident photons, therefore their final energy is higher than their starting one. For more information see the text. . . . .	6
1.3	Feynman diagrams of Raman inelastic scattering events. . . . .	7
1.4	Molecular switch between two Au electrodes. The photochromic unit is a dithienylcyclopentane (DTC) connected by a thiophene ring and a thiol group to both sides. Conduction through the molecule occurs via an alternation of single-double carbon bonds, which extends throughout the whole molecule. By exposing the junction to visible light is possible to switch from closed to open form. The reversed process, verified in the isolated molecule, is induced by UV radiation, but in this case is not observed due to quenching of the excited state in the presence of the electrodes [8],[9],[10]. . . . .	10

1.5	Potential energy of a DTP molecule. $S_0$ and $S_1$ are the potential energy of the ground state and excited state depending on the reaction coordinate (different for every type of molecules). A and B are the ground state of closed and open conformation. Electrons absorbing UV light are excited to state $S_1$ . Then, along the reaction coordinate, they can relax towards A. The reverse process is the opposite, from A to B. The position of C point, related to a relative minimum of $S_1$ , determines the possible inhibition of closing process, favoring the relaxation of the excited closed form towards B. . . . .	12
1.6	Representation of hot carriers generation by Landau damping and consequent system relaxation in a metallic NP. (a) LSP is excited by external incident radiation. (b) Through Landau damping process hot electron-hole carriers are generated and give rise to a highly non-thermal distribution. (c) Electronic population relaxes, through electron-electron scattering events, to a thermal distribution characterized by a temperature higher than the one of the lattice. (d) The electronic system comes back to the initial equilibrium condition by means of electron-phonon scattering. The exceeding energy is transferred as heat to the surrounding. . . . .	16
1.7	Indirect modulation processes. (a) Hot electrons generated by photon absorption in the electrodes can tunnel through higher unoccupied molecular orbitals (smaller arrow), thus contributing to the overall current. (b) Thermal expansion due to local increase of temperature around the electrodes changes the coupling between the molecule and the electrodes, with a consequent variation of junction characteristics. (c) A Temperature gradient across the junction unbalances the electronic distribution inside the contacts and hence increases the electron flux from one side of the junctions to the other (equivalent to an enhancement of the current). . . . .	19
1.8	Photo-assisted tunneling mechanisms. (a) In adiabatic PAT the energy of electrons inside the leads is adiabatically modulated, inducing the absorption or emission of energy quanta, which can lead to elastic tunneling through available molecular orbitals. (b) In non-adiabatic PAT internal molecular transitions are allowed, thus transport mechanism changes from elastic to inelastic. During tunneling electrons can absorb or emit photons with consequent change of transmission channel. . . . .	22

1.9	Non-radiative damping processes. (a) Landau damping is responsible of hot electrons generation, which can then tunnel through the junction increasing the total current. (b) Chemical Interface Damping (CID) is responsible of charge transfer from the electrode to the molecule by absorption of plasmonic quanta. This process is similar to adiabatic PAT, but here the process is triggered by plasmonic response of the system. (c) Plasmon-Induced Resonance Energy Transfer (PIRET) corresponds to energy transfer from the LSP to the molecule through dipole-dipole interaction. In this way electrons in occupied molecular orbitals can be excited in unoccupied ones and then tunnel through the electrodes. This process is equivalent to a non-adiabatic PAT, but here energy quanta are supplied by a plasmon mode. . . . .	23
1.10	Scattering processes representing an electron with energy $E$ transmitted through the junction after absorbing $n$ energy quanta. In the panels are described also symmetry related processes (red dashed lines) corresponding to (a) time-reversal symmetry, (b) time-reversal parity and (c) generalized parity. . . . .	25
1.11	Emission processes depicted on an energy levels diagram of a molecular junction studied with STM. Process (A) corresponds to direct excitation of localized surface plasmons in the tip. (B) refers to transitions between electronic/vibrational levels inside the bias window that correspond to emitted photons with energy $\hbar\omega \leq eV$ . The emitted radiation can couple to plasmon modes of the tip that are therefore indirectly excited. (C) Hot carriers tunneling across the junction can also emit photons similarly to process (B) but their energy can be $\hbar\omega > eV$ . . . . .	30
1.12	Diagram summarizing main processes involved in excitation and decay of localized surface plasmons. . . . .	31
2.1	Band diagram for a single conducting energy level where in (a) is discrete (unphysical situation since the level is strongly coupled with the electrodes) and in (b) broadening is taken in consideration. . . .	37
2.2	Capacitive model of a 0D-system. . . . .	40
2.3	Scheme summarizing the self-consistent procedure. After convergence is achieved, the SCF is used to compute the DOS, transmission and current. . . . .	43
2.4	Representation of the two equivalent configurations of AC voltage drop. In (a) the total drop is partitioned among the two interfaces, therefore is symmetric, while in (b) the drop is just at one interface, thus is asymmetric. . . . .	50

2.5	Graphical interpretation of eq. 2.34 reported in [45] by J. R. Tucker and M. J. Feldman. . . . .	53
2.6	Bessel's functions of first kind. . . . .	53
2.7	Example of 0D-system used to show the results of TG model. . . . .	56
2.8	PAT results using TG model. The left panel (a) shows the $IV$ curve under illumination of the 0D-system chosen as example, while panel (b) represents how the transmission spectrum is modified by the additional sidebands. . . . .	57
2.9	Comparison between the approximated expression of transmission spectrum under illumination with the one formally obtained in the framework of TG model. . . . .	58
2.10	Theoretical prediction of CDT is shown in panel (b) that depicts the $IV$ curve for $\alpha/2$ equal to a zero of Bessel's function $J_0$ . In (a) are reported reference $IV$ characteristics for which $\alpha/2$ does not correspond to a zero. . . . .	59
2.11	$IV$ characteristic computed with TG considering a symmetric (a) or asymmetric (b) AC potential drop at the two interfaces. As it is clear, the two results are not equal that means they could correspond to two different physical situations. Nevertheless the system under study is symmetrical and should not develop a net current under short-circuit condition as in (b). For this reason only case (a) will be considered in the following. . . . .	60
2.12	Graphical representation of gauge transformation from TG case study to typical problem analyzed with Floquet model. . . . .	61
2.13	Diagram that summarizes the SCBA procedure (inner loop) considering also direct iteration between NEGF and Poisson's equation (outer loop). Near the name of the equations there are the corresponding numeric labels referred to those reported in the text. . . . .	81
3.1	Schematic summary of the algorithm implemented in EE-BESD. . . . .	89
3.2	Flow chart of the fitting procedure adopted in this thesis. . . . .	90
3.3	Comparison between the transmission spectra computed with EE-BESD and <i>QuantumATK</i> at equilibrium. . . . .	90
3.4	Variation of EE-BESD transmission spectrum by an applied $V_{DS}$ . . . . .	91
3.5	Comparison between the $IV$ curves obtained with EE-BESD and <i>QuantumATK</i> . . . . .	92
3.6	EE-BESD-NEGF flow chart. The outer light gray block corresponds to the $V_{DS}$ loop necessary to evaluate the current for each value of bias. Instead, the inner dark gray block represents the energy loop used to evaluate the transmission probability for each value of the defined energy grid. . . . .	94

3.7	Comparison between transmission spectra computed with EE-BESD and with EE-BESD-NEGF which do not consider the fitting procedure.	95
3.8	<i>IV</i> characteristics comparison between <i>QuantumATK</i> , EE-BESD and EE-BESD-NEGF.	95
3.9	Comparison between EE-BESD and EE-BESD-NEGF transmission spectra when fitting procedure is included in both models.	97
3.10	<i>IV</i> characteristics comparison between <i>QuantumATK</i> , EE-BESD and EE-BESD-NEGF when the fitting procedure is exploited to compute the Green's functions.	98
3.11	Incident electric fields required to have a fixed value of $U_{AC}$ and $eV_{AC}$ .	101
3.12	Power density and photon flux required to have a fixed value of $U_{AC}$ and $eV_{AC}$ .	102
3.13	Incident electric fields required to have a fixed value of $U_{AC}$ and $eV_{AC}$ when field enhancement is considered.	102
3.14	Summary of the optical parameters and of their relations needed to compute $U_{AC}$ and $eV_{AC}$ .	103
3.15	<i>IV</i> curves of 3TT junction illuminated by different fluxes of photons having energy $\hbar\omega = 0.5$ eV.	106
3.16	<i>IV</i> curves of 3TT junction illuminated by different fluxes of photons having energy $\hbar\omega = 1$ eV.	107
3.17	Transmission spectra of illuminated 3TT junction when the flux is varied considering $\hbar\omega = 0.5$ eV and $V_{DS} = 0.4$ V. The light-blue rectangle represents the BW defined by the applied bias.	108
3.18	Transmission spectra of illuminated 3TT junction when the flux is varied considering $\hbar\omega = 1$ eV and $V_{DS} = 0.4$ V. The light-blue rectangle represents the BW defined by the applied bias.	109
3.19	Current computed with TG and Floquet varying the photon energy for different values of bias. The rectangle in orange highlights the region close to $\hbar\omega = 0$ eV where the TG model shows a limitation.	110
3.20	Transmission spectra for $V_{DS} = 0.4$ V considering different photon energies. In light-blue is highlighted BW corresponding to $V_{DS}$ .	111
3.21	Transmission spectra for $V_{DS} = 0.4$ V. Panel (a) is related to the special case $\hbar\omega = 0$ eV for which TG shows some limitations. Instead panels (b), (c) and (d) are referred to transmission spectra corresponding to current peaks clearly evident in fig. 3.19. In light-blue is highlighted BW corresponding to $V_{DS}$ .	112
3.22	Photocurrent of the irradiated 3TT junction computed with TG and Floquet for different values of bias.	113

3.23	Simulated current of illuminated 3TT junction using TG and Floquet when the incident photon flux is varied. The region highlighted by the orange rectangle corresponds to incident electric fields that induce the electrical breakdown of air. . . . .	114
3.24	Transmission spectra of illuminated 3TT junction referred to a photon flux that increases from panel (a) to panel (f). The light-blue box corresponds to the BW determined by the applied bias $V_{DS} = 0.4$ V. . . . .	116
3.25	In panel (a) it is shown the comparison between the $IV$ characteristics computed with <i>QuantumATK</i> , EE-BESD and the one obtained from the Lorentzian fitting. An example of the fitting procedure is depicted in panel (b) where it is shown the fitted transmission spectrum for $V_{DS} = 0.3$ V. . . . .	119
3.26	Comparison between the photocurrents computed with <i>QuantumATK</i> , Tien-Gordon and Floquet. The photon energy is varied between 0 eV and 2.5 eV while the photon flux is fixed to $1 \text{ \AA}^{-2} \text{ s}^{-1}$ . . . . .	120
3.27	Projected Device Density Of States of the 3TT junction computed with <i>QuantumATK</i> . . . . .	121
3.28	SWMJ based on C8-SAM that has been studied by Arielly <i>et al.</i> [20].	122
3.29	Incident power density as a function of the parameters $U_{AC}$ and $eV_{AC}$ . The field amplification is fixed to $k_{enh} = 550$ . The shown data tip is referred to approximately the experimental incident power density. . . . .	123
3.30	$IV$ characteristics of the C8-SAM junction measured in dark and illumination conditions by Arielly and coworkers [20]. . . . .	124
3.31	Comparison between the <i>ab-initio</i> and EE-BESD results for the single-molecule junction based on C8. In panel (a) it is evident that the EE-BESD characteristics well reproduce the one computed with <i>QuantumATK</i> . Instead in panel (b) it is reported a comparison between the transmission spectra computed at equilibrium. Also in this case EE-BESD gives a result in agreement with <i>QuantumATK</i> . . . . .	125
3.32	In panel (a) are depicted the experimental and simulated $IV$ characteristics in dark and illumination condition for a molecular junction based on C8. The field amplification is fixed and equal to $k_{enh} = 550$ . Panel (b) shows the relative variation of current, with respect to dark condition, depending on the applied bias. . . . .	126
3.33	In panel (a) are depicted the experimental and simulated $IV$ characteristics in dark and illumination condition for a molecular junction based on C8. The field amplification is fixed and equal to $k_{enh} = 1100$ . Panel (b) shows the relative variation of current, with respect to dark condition, depending on the applied bias. . . . .	127

# Acronyms

**1FZ** First Floquet Zone

**3TT** Terthiophene

**BDT** Benzenedithiol

**BJ** Break Junction

**BW** Bias window

**C8** Octane

**CDT** Coherent destruction of tunneling

**CID** Charge Interface Damping

**CNT** Carbon nanotube

**DFT** Density functional theory

**DOS** Density Of States

**DTC** Dithienylcyclopentane

**DZP** Double Zeta Polarized

**EE-BESD** Efficient and Effective model based on Broadening level, Evaluation of peaks, SCF and Discrete levels

**EHT** Extended Hückel theory

**GNR** Graphene nanoribbon

**HLG** HOMO-LUMO Gap

**HOMO** Highest Occupied Molecular Orbital

**IETS** Inelastic Electron Tunneling Spectroscopy

**LCAO** Linear Combination Atomic Orbitals

**LSP** Localized Surface Plasmon

**LUMO** Lowest Unoccupied Molecular Orbital

**MoIFET** Molecular Field Effect Transistor

**NEGF** Non-Equilibrium Green's Function

**NP** Nanoparticle

**NPoM** Nanoparticle on mirror

**NSOM** Near-field Scanning Optical Microscopy

**OFET** Organic Field-Effect Transistor

**OLED** Organic Light Emitting Diode

**OLET** Organic Light Emitting Transistor

**OPE** Oligo(phenylene-ethynylene)

**PAT** Photo-Assisted Transport (or Tunneling)

**PIRET** Plasmon-Induced Resonance Energy Transfer

**SAM** Self-Assembled Monolayer

**SBJ** Squeezable Break Junction

**SCBA** Self-consistent Born approximation

**SCF** Self-Consistent Field

**SERS** Surface-Enhanced Raman Spectroscopy

**SIS** Superconductor-Insulator-Superconductor

**STM** Scanning Tunneling Microscopy

**SWMJ** Suspended Wire Molecular Junction

**TERS** Tip-Enhanced Raman Spectroscopy

**TG** Tien and Gordon (referred to the model)

**UPS** Ultraviolet Photoelectron Spectroscopy

**WBL** Wide Band Limit

**XPS** X-ray Photoelectron Spectroscopy



# Chapter 1

## Introduction

In December 1959, R. D. Feynman delivered his famous speech “There’s Plenty of Room at the Bottom” [1] that have inspired through the decades scientists and engineers to study smaller and smaller physical systems up to the manipulation of single atoms. In 60 years, the vision of this brilliant and inspiring person has been concretized since we actually live in a world where the electronics around us is based on transistors with nanoscale dimensions.

One of the emerging nanotechnology inspired by Feynman’s speech is molecular electronics that attracted the attention of the scientific community for several reasons. In the last years the scaling of the conventional CMOS technology slowed down since shrinking allows to increase the number of transistors per chip but with an inevitable increase of the power density that must be dissipated. Moreover, the reduction of size of a CMOS transistor implies a lot of non-idealities that can affect the behavior of the device such as Short Channel Effect, threshold voltage roll-off, Drain Barrier Lowering (DIBL) and quantum mechanical effects (like quantum confinement and tunneling through the gate dielectric). Nowadays these effects are dealt by the current transistor design, the FinFET, but further reducing the size of the electronic channel towards the physical limit of 8 nm, imposed by the De Broglie wavelength at room temperature, is a fatal step leading to a complete loss of control over the electrons flowing in the channel [2].

The Semiconductor Industry is facing a wall that must be overcome to move toward a better technology that is faster, cheaper and with lower power consumption. One possible path is to rethink the conventional CMOS solution and try to implement alternative technologies. The molecular one belongs to the set of proposals that have the aim to go “beyond CMOS”, trying to solve the critical issues and adding new characteristics to a future electronics.

Molecular devices are based on conduction of single molecules placed in a gap between two contacts that, in common cases, are metals or graphene nanoribbons. This type of junction can be smaller than conventional CMOS devices since the

channel dimension is basically determined by the size of the molecule. To have an idea, one of the first and most studied junction is the one with benzene ring that has a characteristic length of the order of 1 nm. Molecules represent the ultimate limit of miniaturization [2] and their small size can lead to a huge scalability. Moreover, the MolFET (MolecularFET) are potentially faster than CMOS transistors, due to a low number of electrons moving through the junction, with a smaller current density. Nevertheless, all that glitters is not gold: these advantages come with other critical points that must be solved before a possible introduction of molecular technology in a large scale production.

One point is about the small ON current leading often to a too low  $I_{ON}/I_{OFF}$  ratio (few tens). Also the charge transport is much more difficult: coherent tunneling regime is involved and accurate simulations, computationally expensive *ab-initio* methods, are required to model it. In addition to this, the crucial problem of this technology concerns mainly the fabrication: it is true that ideally an infinite number of molecules could be studied and synthesized with a considerable low cost due to Self-Assembled Monolayer (SAM) techniques, however they are not easy to manipulate and integrate on a substrate. Scanning Tunneling Microscopy (STM) is the main tool to have a selective control of matter at the nanoscale, but it is not easy to employ it in a high-volume production. Despite this, the major issue to deal with is the high process variation that is crucial for the performance of a molecular device. For instance, the variability of adsorption sites on the contacts should be controlled with high precision since is one important factor involved in the hybridization of molecular orbitals with the frontier ones of the contacts. Different adsorption sites can lead to different coupling with the contacts and therefore a different *IV* characteristic of the device. Break-Junction (BJ) platforms (as the one in fig. 1.1) are the instrument used to develop the gap aimed to accept the molecule. Depending on the specific physical process used to generate the gap, it is possible to distinguish between Mechanically Controlled BJ (MC-BJ), Feedback Controlled Electromigration BJ (FCE-BJ) or other BJ in combination with STM (STM-BJ). Nowadays, using these techniques, the maximum yield reachable for molecular devices is in the order of 25% ÷ 40% [2] that is too low for a potential short-term solution alternative to CMOS.

The undeniable potential of molecular electronics pushed a lot of researchers to bet on this field, with the hope to find ways which can ameliorate and make it mature as a long-term solution. In particular, a lot of research is focused on how external agents can influence the charge transport through the junction. Such external influence could be of different nature. For example, the action of a gate (back or frontal) can electrostatically control the current and increase the ON-OFF ratio. Instead, other type of interactions lead to sensoristic application: an external compound in proximity of the molecular junction can bond to the molecule altering the characteristic, thus varying the electrical output which could be a clear signal

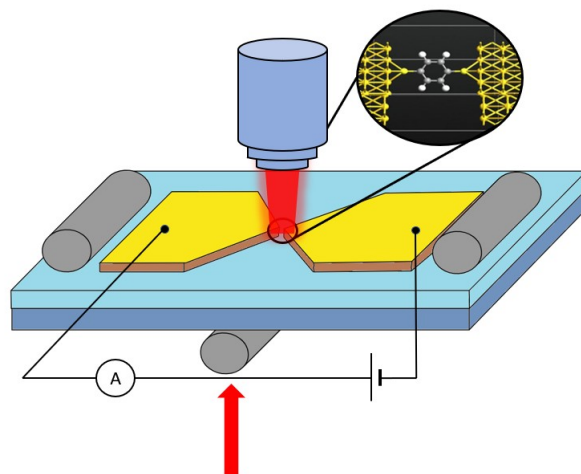


**Figure 1.1:** Example of MC-BJ exploited to perform Raman spectroscopy for studying adsorption site variability. The electrodes are deposited over a flexible substrate (in orange) making an almost point-contact conductance (ideally one atom is in common between them). A rod under the platform pushes the sample against the counter supports in order to induce stress and create the nanogap that will welcome the desired molecule (benzenedithiol in this case). Irradiating the junction (red cylinder) is possible to perform Raman spectroscopy at the same time of conductance measurements.

of the presence of a certain chemical species. Another stimuli, that is the focus of this thesis, is the interaction of light with a single-molecule junction. With respect to other agents, the influence of light on transport properties of the junction has been studied in a large variety of contexts, especially in the last two decades. In a review dated April 2012 [3], M. Galperin and A. Nitzan, two experts in the field, pointed out three main reasons why the interaction of molecular junctions with light has long been perceived as “an obviously needed development”:

- i. *Characterization:* As said above variability is a problem that has to be dealt with. Sometimes even the existence of the molecular bridge between the leads (the terminal parts of the contacts over which the molecule is bonded) is uncertain. Optical techniques, as Raman spectroscopy, can be used to characterize the junction and can be implemented with a Near-field Scanning Optical Microscope (NSOM). This technique can supply the same information of the Inelastic Electron Tunneling Spectroscopy (IETS), the main characterization tool in molecular electronics, but with the advantage of a higher resolution derived from the different frequency of the incident radiation and the scattered one by the junction.
- ii. *Control:* Light is potentially a control tool that can affect the transport properties of the junction by inducing photophysical or photochemical processes

that change the junction electronic structure and/or conformation. The possibility to control the junction with light could be a valid alternative to the common use of a gate contact, which is less efficient in systems of nano-dimensions. Complementary to this application is the emission of light owing to conduction. Thinking about it, emission of light from organic devices is not so strange since OLED (Organic Light Emitting Diode) displays are well established today. However, an OLED is constituted by an active “organic” region that is much more extended than a junction made by a single molecule where the emission derives from a hopping charge transport and not from a tunneling one. Nevertheless, experimental evidences exist for single-molecule junctions and research is moving also in this direction.

- iii. *Complexity*: The dimensions of the leads are characteristic of systems that sustain Localized Surface Plasmons (LSP), i.e. collective electronic oscillations localized at the metal-dielectric interface of nanostructures, which have dimensions smaller or comparable with the wavelength of the exciting field. These plasmons, oscillating coherently with the field, can give rise to strong focusing (implying strong intensity enhancement) and sub-wavelength resolution of electromagnetic effects. The interaction between plasmons and molecules is the base of the so called molecular plasmonics. The excitation of LSP adds complexity to the conductive properties of the junction but at the same time gives the possibility to study new physics and take advantage of new phenomena, as it is the case for Raman Spectroscopy (see section 1.1)

The crossover between molecular electronics and molecular plasmonics gives rise to an emerging field that could be named “single-molecule optoelectronics”, whose boundaries are not well defined since represents the union of the two fields. However, the main goal is clear: study and develop single-molecule devices that can be controlled by, or control, the electromagnetic field. As underlined in [3], although experimental results concerning key-arguments exist, theoretical works greatly exceeds the experimental ones both in number and in variety of considered phenomena. The reasons could be the difficulties in realizing reproducible observations and the rare availability in a laboratory of the adequate instrumentation to perform measurements of molecular electronic transport. This is a limitation that must be overcome since, without a large amount of data, is difficult to validate models and make further steps towards a solid technological application.

In the following sections I will briefly present the main topics, already mentioned above, and results concerning the interaction of light with molecular junctions in order to give the reader an exhaustive, as far as possible, landscape of what research has been focused on in the last two decades. Then, in the next chapter, I will focus more on what really has been the topic of this work, i.e. the modeling of photo-assisted tunneling (PAT) in molecular junctions.

## 1.1 Raman Spectroscopy

In this section I will introduce Raman Spectroscopy and I will argue why is important in molecular electronics. The theoretical part follows the notes I have taken in 2019 attending F. Giorgis’s course “Materials and characterizations for Micro and Nanotechnologies” at Politecnico di Torino.

Raman Spectroscopy is part of optical characterization techniques which acquires the dynamic fingerprint information of molecules in real-time under ambient conditions. This technique is based on the acquisition and spectral analysis of the field scattered by a sample (which can be for example a crystalline system, micro-crystals in an amorphous matrix or molecules). When photons impinge on the sample there is a certain probability they interact with the vibrational activity of the analyzed system. In fig. 1.2 it is possible to see a simplified Jablonski diagram used to represent the energy states of a discrete levels system. Three possible interactions can happen: one elastic scattering and two possible inelastic scattering. The first one is called Rayleigh scattering and it is the most likely to happen (corresponding to biggest arrows in fig. 1.2) since collective vibrations (generally called “phonons”) are not involved. The impinging photons are scattered back (that implies a change in momentum) with the same amount of energy of their initial state. Considering photons in infrared or optical spectrum, their energy is lesser than the one needed to excite the electrons, that means photons are not absorbed and then emitted back because their energy is not sufficiently large. Nevertheless, it is possible to describe the scattering process defining what are usually called “virtual states”. These states are not proper of the system, but allow to describe scattering in two steps considering a fictitious transition to a state with following de-excitation. On the other hand, when phonons interact with the incident radiation, something different can happen. Phonons are quasi-particles that carry a certain amount of momentum and energy with them, therefore when interacting with photons (see fig. 1.3), the conservation of momentum and energy must be respected. When a phonon is created from the initial photon the process is called Stokes scattering and the final energy of the photon is smaller than the initial one. On the contrary, when a phonon is absorbed from the vibrational environment of the system the process is called Anti-Stokes scattering and the final energy is greater than the initial one. These scattering events are less probable since they are multi-body interactions with the involvement of an additional particle with respect to the elastic case. For this reason, the arrows representing Stokes and Anti-Stokes event in fig. 1.2 are smaller than the ones for Rayleigh. Moreover, the arrows referred to Stokes are bigger than the one for Anti-Stokes because the absorption of phonons is related to their thermal distribution. In other words: there must be present phonons for absorption (not possible at zero temperature) while emission is always possible and therefore it has a bigger probability to happen.

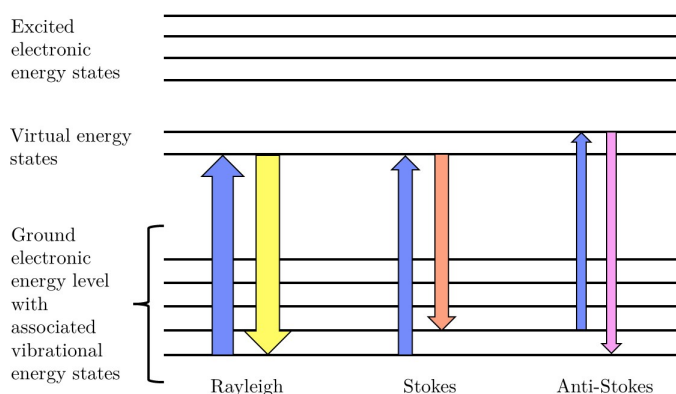


**Figure 1.2:** Jablonski diagram describing different scattering processes for a system having discrete energy levels (as a molecule is). In Rayleigh scattering no collective vibration (generally called “phonon”) of the molecule is involved and the scattered field has the same frequency of the incident one. In Stokes scattering the interaction with the system leads to emission of phonons that reduces the energy of the reemitted photons. On the other hand, the Anti-Stokes scattering concerns the absorption of phonons by the incident photons, therefore their final energy is higher than their starting one. For more information see the text.

Analyzing the frequency of the inelastic scattering field by means of a notch filter, that removes the Rayleigh component (not meaningful in Raman spectroscopy), it is possible to retrieve information about the vibrational activity of the system. In particular, for the case of molecules, different bonds can have different stretching, scissoring or rocking activity. Knowing the “Raman” shift of the analyzed field, i.e. the variation of photon energy, it is possible to recognize different types of bonds and related activities. It is worth underlining that the registered intensity of the shift is generally very low but exist ways to increment the signal. One way is to consider an incident photon energy large enough to excite electrons, i.e. make them absorb the incident radiation. In this case virtual states are not needed and we talk about of “resonant” Raman spectroscopy. There exist also other ways to enhance the inelastic scattering in which plasmons play a crucial role and they will be described below.

Coming back to molecular electronics, how is this technique applied? The incident field is focused on the junction by means of an objective lens. The junction is created on a BJ platform thanks to which electrical measurements can be performed simultaneously with the optical spectroscopy analysis (fig. 1.1). However, obtaining the optical signals from the junction is difficult for several reasons:

- mismatch between the optical diffraction limit and the length scale of molecules;
- injection of light in nanogaps is challenging;

- scattered field could be damped by the metallic contacts.

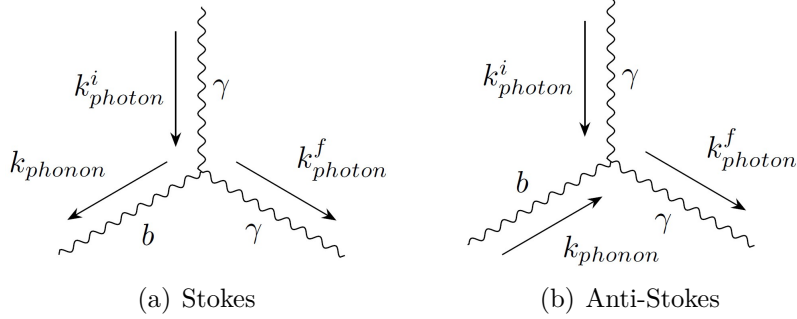


**Figure 1.3:** Feynman diagrams of Raman inelastic scattering events.

Although seems difficult to inject light directly in the junction due to its diffraction limit, it is possible to overcome these limitations either exploiting the same geometry of the junction or using a more sophisticated experimental setup. Both solutions are based on the excitation of localized plasmons: in the first case the impinging laser excites the LSP in the leads while in the second case the excitation happens on a tip (made of, or coated with, a metal) of a STM. Due to the resonance of plasmons, a huge intensity enhancement of the field in a localized point of space is observed: in this way light for Raman spectroscopy can be injected into the nanogaps between the electrodes.

These two characterization techniques are called Surface-Enhanced Raman Spectroscopy (SERS) and Tip-Enhanced Raman Spectroscopy (TERS). The LSP couples with the field only if the frequency is below the plasma frequency: in this case the generated enhancement of the local field can be huge reaching the order of  $10^{10}$ . This value can be controlled by the shape and size of the metallic nanostructures and the distance between them. Moreover, the polarization of light is important to have an efficient coupling to the LSP of the leads (generally obtained with a polarization parallel to transport direction). In addition to this effect, a chemical enhancement can also take place: it accounts for resonant Raman scattering resulting from the charge transfer resonance taking place between the metal and the molecular orbitals. This effect contributes with an enhancement in the order of  $10^3$ . Overall, these contributions leads to a remarkable sensitivity up to single molecule detection that is an outstanding result for a non-destructive characterization technique.

A hybridized electrical-spectroscopic technique for characterizing current-carrying junctions can feasibly be developed. It is worth reporting that strong temporal correlation between the Raman response and the conductance measurement was found in nanogaps, confirming single molecule sensitivity of the

nanogaps. An example is reported in [4] where a single-molecule junction made of benzenedithiol (BDT) and gold contacts is studied using a MC-BJ as the one in fig. 1.1. Temporal measures of the vibrational activity and conductance are taken into consideration. Before creating the gap, the value of conductance is around  $G_0 = 2q^2/h \approx 7.748 \times 10^{-5} \text{ S}$  that is the conductance quantum for a perfect atomic contact. In this time interval the Raman shift is related to weak background signals. After the creation of the gap and consequent adsorption of benzene, the conductance drops to  $10^{-2}G_0$  and the optical response increases (corresponding to evident peaks in the Raman spectrum). These are clear signals that adsorption occurred and exists a certain temporal correlation between optical and electrical measurements. This correlation can be utilized to study adsorption sites whose variability is a crucial point as commented above. In fact, in this paper, S. Kaneko *et al.* assert that the Raman activity they observed was related to a specific site, the “bridge” type, i.e. when the two sulfur atoms are strongly bonded with terminal gold atoms of the contacts. In this way it could be possible not only to know the creation of the junction but also its type, with related electrical properties, just using optical techniques. This result is a good starting point for future researches dealing with variability and underlines how important is knowing the details of interaction of light with molecular junctions.

It is worth saying that there exists a number of papers focused on possible practical application of Raman spectroscopy, thought not only as a simple characterization tool. For example, S. Kaneko *et al.* [5] observed the possible dependence of Raman response from the applied voltage. In [5] an aminobenzethiol molecule is taken in consideration: Increasing the applied bias from 0 to 0.2 V, an additional peak in the Raman spectrum appears (at  $\sim 1142 \text{ cm}^{-1}$ ) and it is related to a bending mode of the C-H bond. This can be explained taking into consideration charge transfer resonance between the contacts and molecular orbitals. In this case, increasing the voltage, the LUMO (Lowest Unoccupied Molecular Orbital) decreases in energy and, considering the broadening of the level consequent to hybridization with frontier orbitals of the contacts, it becomes available for charge transfer (from the contact to the molecule) increasing in this way Raman response. The appearing of a new peak depending on the applied bias could be exploited as a possible “optical switch”: light intensity at a certain frequency is generated only if a threshold voltage is applied to the junction. Of course this is not easy to be integrated in a circuit, but this did not stop other groups to work on this topic. In [6], H. Bi *et al.* made a study similar to the one reported above but choosing a tetramethylated-terphenyl-dithiol as molecule under analysis. The four methyl groups make the molecule highly sterically hindered with non planar configuration. This reduces the polarizability of the molecule, proportional to the overlapping of  $\pi$ -orbitals, which is strictly correlated to Raman response. Applying a voltage

of 1 V, transient charging effects induce conformational changes and increase  $\pi$ -conjugation with a consequent restore of Raman activity. They proved a ratio of nearly two orders of magnitudes between the signal in the ON state and the one in OFF state (with no applied bias). This result is similar to the one commented above even if the physical explanation behind the measures is different.

These examples are just the beginning of a branch concerning the interaction between light and molecular junction. Only in recent years, papers regarding logic gates, implemented using Raman activity, started to come out. A recent example [7], dated 2020 and signed again by H. Bi, shows how logic operations, and not only a simple switch, can be optically induced. Similar to a standard gate, they considered as inputs (A, B and C) the light coming from three corresponding near-field microscopes and focused on a junction with oligo(phenylene-ethynylene) (OPE-3). Signal A and B comes from the sides whereas C from the top. Depending on the combination of the signals, the junction is illuminated with a different symmetry that influences the optical response. They realized that, with no signal C, the peak in the Raman spectrum at  $1400\text{ cm}^{-1}$  was present only if the light from input A and B was turned on. This is equivalent to an AND gate and, it turned out, that they were able to prove also other functions as OR, XNOR, TRUE and NOT, just combining different inputs and considering specific peaks in the spectrum. This work tells us again that there is a strong interest in studying in deep the interaction of light with molecular junctions. It is clear that these attempts to exploit the optical response are less manageable, thinking about a possible insertion in an integrated circuit. Moreover, they are less “conventional”, i.e. they are not similar to solid-state optoelectronic devices that are well known. An optically controlled molecular switch can be obtained also with other mechanisms, much more feasible for practical implementations. In the following section an other branch of molecular optoelectronics is described and it seems to be among the most promising proposals in the field.

## 1.2 Photochromic switching

In molecular electronics the active region of a device is a single molecule connected to two contacts. The molecules used in this context consist of a molecular backbone and anchoring groups on both ends used to bond the molecule to the leads (determining in this way the coupling characteristic of the interface). The molecular backbone can be composed by a photochromic unit, i.e. a molecule that undergoes structural changes (called *isomerization*) upon irradiation with light, at a specific frequency, in isolation condition. The resulting *isomer* has a different conformation since the covalent bonds rearrange and the conjugation throughout the molecule can be turned on and off [8]. Because of the change in quantum

confinement, the electronic structure of the molecule will also be modified, resulting in a change that is reflected by different properties such as absorption spectrum, energy states, dielectric constant and redox potential under light irradiation [9]. Photo-isomerization can also be reversible using an electromagnetic field at another frequency. Nevertheless, things become less trivial when photochromes are put inside a gap between contacts: photo-isomerization can be reversible or not depending on the type of molecule and on the coupling strength. The most promising photoswitching molecules are diarylethene, azobenzene, dihydropyrene and spiropyran [9]. These molecules are of great interest since they have two isomers with opposite conducting properties. The goal is to exploit light in order to switch between these two conformations. The “closed” form is conjugated delocalizing  $p$ -orbitals, whereas the “open” form is nonconjugated with localized  $p$ -orbitals [9]. Therefore, The HOMO-LUMO gap (HLG) and the related electrical conductance are modified depending on the isomer. The closed form is identified with the ON state, whereas the open form is related to the OFF state. In this way is possible to open or close the conduction channel irradiating the junction with light with two specific wavelengths.

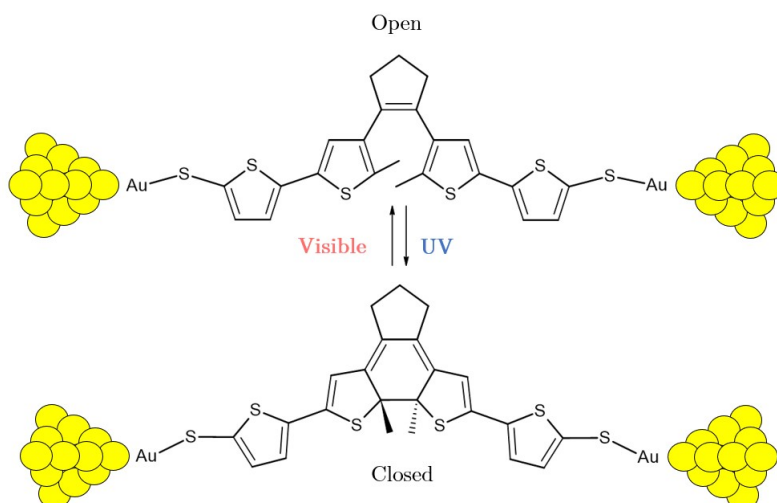


**Figure 1.4:** Molecular switch between two Au electrodes. The photochromic unit is a dithienylcyclopentane (DTC) connected by a thiophene ring and a thiol group to both sides. Conduction through the molecule occurs via an alternation of single-double carbon bonds, which extends throughout the whole molecule. By exposing the junction to visible light is possible to switch from closed to open form. The reversed process, verified in the isolated molecule, is induced by UV radiation, but in this case is not observed due to quenching of the excited state in the presence of the electrodes [8],[9],[10].

Photoswitches made with diarylethenes are the most studied because of their additional attractive properties: they have a fast photoresponsibility, excellent

thermal stability, fatigue resistance, high photoreaction quantum yield (i.e. the effectiveness of light absorption to induce photoisomerization) and good performances in both solution and solid phases [11]. Moreover, their length change upon isomerization is negligible. This allows for minimal mechanical stress when a molecule between two electrodes changes conformation. On the other hand, molecules like azobenzenes have isomers, even more than two, with different length [12] and this affects the resulting coupling, making it less controllable.

Focusing on the first class, diarylethene is the general name of a class of compounds that have aromatic groups bonded to each end of a carbon-carbon double bond [13]. The most employed molecules belonging to this class are dithienylethenes, i.e. alkenes with a thiophene ring on either side [13] (shown in fig. 1.4). A common alkene used for this application is cyclopentane that give rise to dithienylcyclopentane (DTC) which is a photochromic molecule under study for photoswitching. In 2003, D. Duric' *et al.* [8] demonstrated the one-way response of the photoswitch depicted in fig. 1.4. Using a MC-BJ and irradiating the junction with light in the visible range ( $\lambda = 546$  nm) it was possible to pass from the conducting state to the insulating state. The reversed process, normally induced by UV light ( $\lambda = 313$  nm) on the isolated molecule, was not observed for the photochrome located in the gap. This one-way response was attributed to quenching of the excited state (or limited photoexcitation) in the presence of the electrode [10]. Such limitation occurred through strong interface couplings produced, in this case, by the covalent bond between the thiol groups and the gold contacts. This behavior was explained by taking in consideration potential curves, related to the isolated molecule, of the ground and excited state depending on the distance between the carbon atoms (i.e. the reaction coordinate) responsible for the ring closure [8]. When electrons in a ground state absorb a certain energy from light, they are excited. Subsequently, the electrons relax to another ground state and the molecular form is changed [9]. This mechanism is shown in fig. 1.5 and it is referred to the result obtained in [8] but can be related to a generic photoswitch. D. Duric' *et al.* justified the absence of closing process observing that the position of C point, along the potential curve  $S_1$  of the excited state, is in proximity of the gold Fermi level. As a consequence, an efficient hybridization of the gold states with the first excited molecular one is taking place at the right side of the ground state maximum [8]. This quenching does not allow the relaxation from the excited closed form to the open ground state (point A), but it could be possible for different positions of point C.

Later, in 2005, J. He *et al.* found that the photo-isomerization is reversible for DTC molecules when H atoms in cyclopentane are substituted by six F atoms (fluorinated-DTC) [14]. Also other types of electrodes were considered, in particular carbon-based contacts since they have extraordinary and modulable electronic properties, in addition to natural compatibility with molecules for creating stable bonds [15]. In order to change molecule-electrode interface and obtain reversible

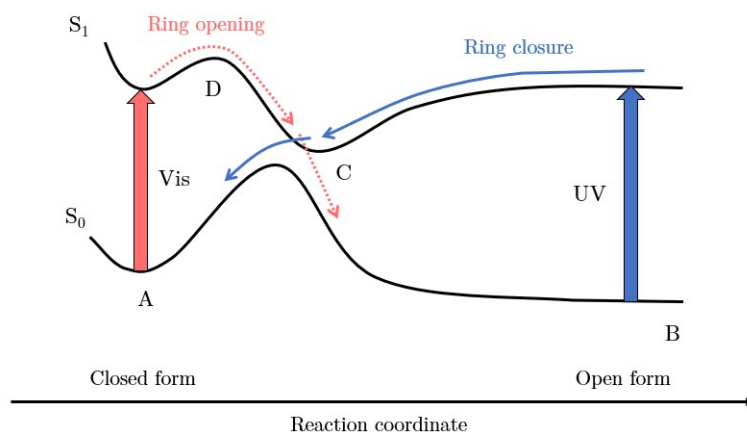


**Figure 1.5:** Potential energy of a DTP molecule.  $S_0$  and  $S_1$  are the potential energy of the ground state and excited state depending on the reaction coordinate (different for every type of molecules). A and B are the ground state of closed and open conformation. Electrons absorbing UV light are excited to state  $S_1$ . Then, along the reaction coordinate, they can relax towards A. The reverse process is the opposite, from A to B. The position of C point, related to a relative minimum of  $S_1$ , determines the possible inhibition of closing process, favoring the relaxation of the excited closed form towards B.

isomerization, electrodes as graphene nanoribbons (GNR) or carbon nanotubes (CNT) have been investigated [16],[17]. It turned out that considering DTC, connected to GNR by means of two phenyl rings and terminal amine groups, the opposite unidirectional switching (from the open to the closed form) is observed [16]. Also in this case a quenching results from the coupling produced by the covalent amide linkages. In 2016, C. Jia *et al.* proved that changing the interface between the central unit and the electrodes, proposed in their previous work [16], could allow reversible photoswitching between the two isomers. As reported in [18], they decrease the coupling with GNR electrodes adding three methylene groups ( $\text{CH}_2$ ) to the molecular backbone. In this way, reversible photoswitching was achieved with an ON/OFF ratio  $\sim 10^2$ , stability over a year and high reproducibility with 46 devices with more than 100 cycles. Although this achievement is considered a keystone and a guidance for future diarylethene-based molecular junctions, it arrives with some drawbacks. Introducing methylene groups to break the conjugation between the photochrome and electrodes is a sword with two edges [11]. Decreasing the coupling reduces also the observed conductance since, as underlined by C. Jia and coworkers, the system moves from the Landauer regime to Coulomb blockade regime. This result is one of the most important concerning photoswitching with diarylethenes and confirms again how crucial is the role played by the molecule-electrode coupling strength in determining the performance of the device.

Applications involving photochromes are multiple and many of them are reported

in [11], [15], [19]. Concerning molecular information processing, AND and OR logic gates, implemented with Au-molecule-Au junctions, were demonstrated exploiting multiple external stimuli such as light/pH or light/electrochemical oxidation [11]. Photochromes can also be used for functionalization of other materials with the aim of modulating their properties (conductivity, absorption, magnetism, fluorescence etc.) with light. In this context, functionalized carbon-based materials are investigated for sensing application, solar thermal storage and memory device [15], whereas organic semiconductors functionalized with photochromes are studied to be employed in OLED (Organic Light Emitting Diode), OFET (Organic Field-Effect Transistor) and OLET (Organic Light Emitting Transistor) [19].

As already said, diarylethenes are the most promising photochromes, therefore further improvements and optimization are still needed to reach their full potential. Most reported diarylethenes are lacking of high photofatigue resistance to achieve the desired robustness. In general, they could undergo switching in 10-20 cycles or even less [11]. Photochromic quantum yield is another issue that decreases the working efficiency [11]. Moreover, photoisomerization using visible/near-infrared frequencies is a long-pursuing goal to reduce phototoxicity and the background signal [11].

In light of what just discussed, it is possible to say that photochromic switching is one of the most promising branch concerning control of electronic devices with electromagnetic fields. However, a better control of the interfacial electronic coupling is required, as already commented, since crucial for reversible isomerization and conducting properties. This field needs further insights since the same isomerization process is not fully understood. The nature of the barrier between the two stable states and the dynamics of the related barrier crossing process, in current carrying junctions, are not well known in every case [3], thus the possible reversibility of the photochrome cannot generally be predicted. Moreover, light is generally considered as an external trigger for the molecule without taking into account the influence that can have on the transport process since it is turned off after photoisomerization is complete. On the other hand, solid-state optoelectronic devices are normally subjected to a prolonged external stimulus and, since the main target is to develop single-molecule optoelectronic devices, it is required a study of photo-assisted transport in molecular junctions, that is the topic of this thesis and is introduced in the next section.

## 1.3 Photo-assisted transport in molecular junctions

The interaction of light with optoelectronic devices has been widely studied over the years, in particular the effects on transport properties which are the base of

nowadays light detectors and photovoltaic cells. The dimensions of these devices is crucial since determines the amount of radiation absorbed by the electronic environment. Decreasing sizes towards nanometric scale adds complexity to the system under study, not only for the analysis of transport properties, but also for what concerns the optical response of the device. Molecular junctions belong to this context since their dimensions are intrinsically nanometric and because their optical response, as already mentioned above, is complex and difficult to be determined. In the following I will show how light can influence charge transport in different ways. Each of them has a different weight on the overall current flowing through an illuminated molecular junction and, for this reason, it is important to elucidate which effect is the dominant one for the specific system under analysis. This is not easy to be done since depending on the photon energy, the incident power, the type of molecule and contacts there could be one dominant process or another or more of them.

The mechanisms involved in the modulation of current can be divided in two groups described as follows:

- i. *Indirect modulation*: Light can induce possible thermal effects which in turn influence transport properties. In this way light *indirectly* modulates transport.
- ii. *Direct modulation*: The electromagnetic radiation is *directly* involved in charge transport, therefore becoming photo-assisted.

It is not always easy to understand if the increase of current is caused by a thermal or an optical effect. In many experiments it is important to study how the variation of temperature in the leads can change the conductance of the junction, as it is done in [20], [21], [22]. Then, knowing the possible variation, it is possible to rule out thermal effects, if negligible with respect to the optical ones, or they can be identified as the main reason of conduction enhancement.

Before describing the main photo-induced thermal effects and introduce the PAT in the context of molecular junctions, in the next subsection I will describe in general localized surface plasmons since they play a fundamental role both in indirect and direct charge transport modulation.

### 1.3.1 Localized Surface Plasmons

As already mentioned above, localized surface plasmons are placed at the metal-dielectric interface of nanostructures, such as nanoparticles (NPs), which can be excited by electromagnetic radiation if its frequency is around the surface plasmon resonance  $\omega_{LSPR}$ . Around this frequency, the screening action of conduction electrons combined with the restoring force due to Coulombic attraction between electrons and nuclei, gives rise to collective electronic oscillations with frequency

equal to the one of the incident field [23]. This phenomenon implies two main results [23]:

- The electric field is enhanced near the surface of the nanostructure. In this way is possible to focus an electromagnetic field beyond the diffraction limit, thus reaching light injection with sub-wavelength resolution.
- The optical absorption has a maximum at  $\omega_{LSPR}$ . Differently from planar metal surfaces, for which most of the incident light is reflected (in the range of optical frequencies), nanostructures can efficiently absorb at the resonance frequency since they can collect light from an area larger than their physical size (antenna effect) [24].

Besides these impressive results, there is another advantage of using nanostructures. Their resonance frequency  $\omega_{LSPR}$  can be tuned changing the design and, in particular, the geometry. For example, if two metallic NPs are considered, it is possible to tune  $\omega_{LSPR}$  varying the shape, the distance between them or the dielectric permittivity of the surrounding. It is easy to understand that two NPs shaped as two bowtie antennas would enhance more the field in the gap between them than spherical NPs.

It is important to notice that, in the framework of molecular junctions, the molecule connecting two nanostructured contacts varies the apparent dielectric function of the environment [25]. Moreover the length of the molecule determines the gap size, i.e. the distance between the contacts. In the light of what said above, it is possible to state that changing the characteristics of the molecule placed inside the junction allows to tune  $\omega_{LSPR}$ , but also the coupling between plasmon modes (i.e. different allowed oscillating modes) and the electronic structure of the molecule. Indeed, as I will describe more in detail below, localized plasmons can be excited and can interact in more ways inside molecular junctions. The possibility to tune  $\omega_{LSPR}$  permits to easier observe phenomena depending on the coupling between molecule and plasmons. Of particular importance is the relation between the tunneling current and the plasmonic response of the contacts (for more details see subsection 1.3.3). The interest in studying plasmons in molecular junctions is justified also by the facts that the resonance frequency of most common metal NPs (such as Au-NPs or Ag-NPs) is in the visible range or near-IR that corresponds to typical excitation of molecules [25]. This field of research takes the name of *molecular plasmonics* which represents an important piece in the puzzle, for deeply understanding PAT in single-molecule junctions.

In order to analyze thermal effects, it is of great importance understand what happens after plasmon excitation. LSPs do not have a long timelife, i.e. they are subjected to unavoidable loss processes. Indeed they decay through different mechanisms, which can be *radiative* or *non-radiative*. These decay pathways dipphase

electronic oscillations and damps the population relative to plasmon modes. For what concerns radiative decay, the amplified electromagnetic field is attenuated by re-emission of photons in the far-field by means of scattering processes. This phenomenon can be crucial in experiments since allows to detect excited plasmons by placing objective lens in the proximity of the nanostructure. On the other hand, non-radiative decay can occur following different pathways. The principal mechanism is called Landau damping and is the most studied since involved in NPs. Other non-radiative pathways exist and are more relevant for photo-assisted transport in molecular junctions, thus they will be described later in subsection 1.3.3.

Landau damping is responsible of hot carriers generation and consequent thermal dissipation which are directly related to thermal effects involved in indirect charge transport modulation. For this reason, now an exhaustive description of the process will be given following the one of M. Brongersma and coworkers in [24]. The overall process can be divided in different steps (each one with a typical time scale) that are shown in fig. 1.6, taking as example a metallic NP, and described as follows:

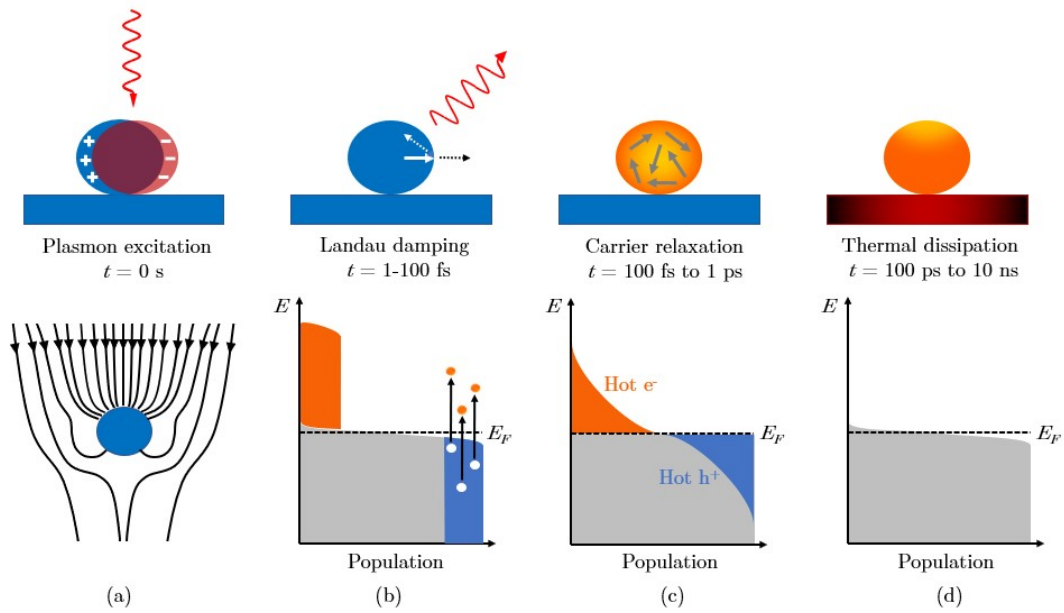


**Figure 1.6:** Representation of hot carriers generation by Landau damping and consequent system relaxation in a metallic NP. (a) LSP is excited by external incident radiation. (b) Through Landau damping process hot electron-hole carriers are generated and give rise to a highly non-thermal distribution. (c) Electronic population relaxes, through electron-electron scattering events, to a thermal distribution characterized by a temperature higher than the one of the lattice. (d) The electronic system comes back to the initial equilibrium condition by means of electron-phonon scattering. The exceeding energy is transferred as heat to the surrounding.

- a. At  $t = 0$  s a localized surface plasmon is excited and the near-field is enhanced. The excitation is represented in the top panel by the oscillating electronic cloud around the NP, while the enhancement is evident in the bottom panel from the higher density of flux lines.
  
- b. After excitation Landau damping takes place. The electromagnetic field enhanced by localized plasmonic oscillation is a time dependent perturbation which can induce electronic transitions inside the NP. The absorption of plasmon quanta leads to the generation of hot electron-hole pairs on a timescale  $\tau_L$  ranging from 1 fs to 100 fs. As a consequence, carrier distribution becomes highly non-thermal, as apparent in the bottom panel of 1.6(b). This distribution depends on different parameters such as the geometry, the resonance frequency (itself depending on geometry), plasmon mode and the electronic structure of the particle (i.e. the considered metal). In particular, since the hot electron-hole pairs generation depends on absorption, it is possible to tune in some way the hot carriers population by varying the imaginary part of the dielectric constant of the NP. This is important since it can reduce or increase the efficiency of hot electron injection from NP (or other nanostructured systems) to another nanometric system such as molecules adsorbed on the NP. The hot electron injection efficiency is particularly relevant for energy harvesting devices and, in the case of molecular junctions, for indirect modulation of transport (more details in subsection 1.3.2).
  
- c. For high photon energy, a small fraction of hot electrons can escape from the system, without energy loss, since they gain an energy greater than the working function of the metal. If detected, it is possible to obtain information on their kinetic energy and momentum (same principle of optical characterization techniques such as UPS or XPS). Nevertheless, this fraction of electrons is very small and in ‘standard’ plasmonic metals the working function is greater than the resonance frequency ( $W > \hbar\omega_{LSPR}$ ) therefore electrons cannot escape into vacuum. In this case what happens is a redistribution of energy in the hot electron population (which coarsely is  $E_{hot} \in [E_F, E_F + \hbar\omega_{LSPR}]$ ) by means of electron-electron scattering, such as Auger processes, between the hot carriers and the many lower energy electrons. This mechanism has been extensively studied in extended metal surfaces but not so much in nanostructures. For the first, time-resolved studies say that the characteristic timescale  $\tau_{e-e}$  for electron-electron scattering ranges from 100 fs to 1 ps. In this time interval the highly non-thermal distribution relaxes to a thermal one characterized by an (effective) temperature of the electronic population ( $T_{el}$ ) greater than the lattice temperature ( $T_{lat}$ ), therefore another relaxation process is needed to come back to initial equilibrium condition.

- d. Equilibrium between electrons and the lattice is achieved through inelastic scattering processes, such as optical electron-phonon scattering. This type of process has an efficiency (scattering rate) that decreases with the electron energy. Thanks to electron-electron scattering, hot carriers lose energy and, as a consequence, inelastic electron-phonon scattering rate increases. Over a timescale  $\tau_{ph}$  of some ps,  $T_{el}$  relaxes to the temperature of the lattice and so the electronic system is returned back to the situation before LSP excitation. The last step consists of heat transferred to the surrounding of the metallic structure. This process can happen in a time interval  $\tau_{heat}$  ranging from 100 ps to 10 ns depending on the NP characteristics, but also on the conduction properties of the surrounding environment.

It is worth to underline that the reasoning of this subsection are general and can be related to plasmon excitation in the contacts of molecular junctions. Furthermore, other phenomena involving localized plasmons exist, as already mentioned above, and they will be described later while describing direct interaction between photons and molecular junctions. On the other hand, what just explained about LSP is enough to well understand indirect modulation charge transport that will now be described.

### 1.3.2 Indirect modulation

All thermal effects, induced by an incident field on a junction, are related to the absorption of photons in the leads with possible plasmon excitation and related unavoidable loss mechanisms. In fig. 1.7 the most important indirect modulation processes are shown and they are described here following the review done by L. Chen *et al.* [10]:

- a. The left panel of fig. 1.7 describes the additional contribution from hot electrons to the tunneling current. Hot electrons are generated by absorption of light by the contacts and consequent electron-hole pair generation, that is by far more efficient at resonance frequency with related Landau damping. These electrons can tunnel through the unoccupied molecular orbitals located at higher energies, but only if they are sufficiently close to the junction (closer than the inelastic mean free path at the corresponding energy). This means they must tunnel before they have equilibrated with the bulk of the electron gas (so on the timescale  $\tau_L$ ). If the hot electrons are mainly generated by plasmons, the photocurrent should depend also on the polarization and wavelength of the plasmon excitations. It is worth notice that a net short-circuit current (i.e. a photocurrent due to hot electrons contribution) at zero bias is possible only if the hot carriers production is unbalanced between both sides of the junction, so that a net flow of electrons can appear. A net short-circuit hot electron

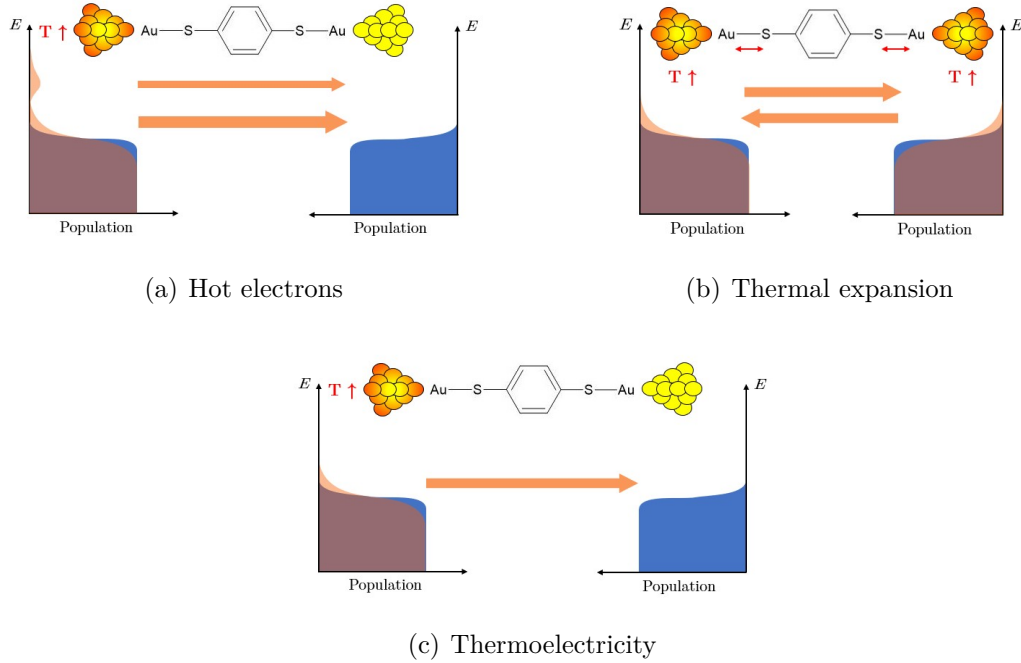


**Figure 1.7:** Indirect modulation processes. (a) Hot electrons generated by photon absorption in the electrodes can tunnel through higher unoccupied molecular orbitals (smaller arrow), thus contributing to the overall current. (b) Thermal expansion due to local increase of temperature around the electrodes changes the coupling between the molecule and the electrodes, with a consequent variation of junction characteristics. (c) A Temperature gradient across the junction unbalances the electronic distribution inside the contacts and hence increases the electron flux from one side of the junctions to the other (equivalent to an enhancement of the current).

current implies a photovoltage in open-circuit condition because carriers accumulate at the two sides of the junction developing a potential drop. This is a clear signal for possible energy harvesting applications exploiting molecular junctions. This reasoning about net short-circuit current is general and can be applied not only to hot carriers, but also to every other processes involved in photocurrent generation. There must be an asymmetric situation between the two contacts to see the appearing of a net short-circuit current. This concept will be resumed next in this work and is of fundamental importance for studying the interaction of light with any junction.

- b. In the right panel the effects of thermal expansion are taken in consideration. It occurs when optical absorption locally increases the temperature of the metal electrodes making them expand. This implies a decrease of nanogap size, but also a change of coupling between the molecule and the contacts. As a consequence, charge transfer rates between electrodes and molecules are

different, therefore modifying the current-voltage characteristic. Of course this process can also be triggered by simply heating the junction to modulate its characteristics. It is important notice that in this case the temperature variation is the same for the two electrodes, therefore a net short-circuit current is not developed.

- c. The bottom panel considers another effect that is thermoelectricity. Light illumination can unbalance the temperature across the junction due to different heating of the contacts and induce an additional contribution to current: the ensuing temperature change  $\Delta T$  induces a photothermoelectric effect on the junction conductance, creating a thermo-voltage and hence an additional tunneling current. Consequently, a photovoltage is generated in the open-circuit limit and can be expressed as  $\Delta V_{th} = -S\Delta T$ , where  $S$  is the Seebeck coefficient of the junction [26]. This mechanism would be extremely relevant for future molecular devices aimed to convert both thermal and optical energy in electrical one.

These processes have been theoretically tackled in different ways and, although the number of experimental papers on illuminated molecular junctions is limited, there are examples of measurements of these phenomena. In [21] E-D. Fung and coworkers analyzed the contribution of hot-electrons in a molecular junction made from 4,4'-bipyridine bound to Au electrodes. They confirmed that hot electron transport is the dominant mechanism when the radiation wavelength is absorbed by the contacts and the hot carriers relaxation time is long enough. Concerning instead photothermoelectric effects, P. Reddy *et al.* in [26] measured the Seebeck coefficient for 1,4-benzenedithiol, 4,4'-dibenzenedithiol, and 4,4''-tribenzenedithiol by applying a temperature bias (i.e. a gradient) and then measuring the consequent voltage drop. Lastly, thermal expansion effects are generally taken in consideration in experiments by characterizing the dark current of the junction for different temperature and verifying that the maximum thermal difference induced by the incident optical power does not significantly change the current.

Although photo-induced thermal effects have been extensively described in this subsection, in the following I will essentially neglect their contribution to focus more the attention on photo-assisted transport. Nevertheless is extremely important have them in mind and know when they can affect significantly the current. Next topic to analyze is the direct interaction of the radiation field with charge transport, that is introduced here following.

### 1.3.3 Direct modulation

Direct modulation effects are physical phenomena resulting from direct involvement of an incident radiation field on the charge transport of a molecular junction.

Depending on the photon energy with respect to the characteristic levels of the considered system, it is possible to divide the direct modulation transport mechanisms in *adiabatic* ( $E_{ph} < \text{HLG}$ ) and *non-adiabatic* ( $E_{ph} > \text{HLG}$ ).

### Adiabatic photo-assisted tunneling

Adiabatic processes are typically considered when the electromagnetic field is in the microwave range. In this situation the radiation frequency is well below the LSP resonance, therefore the field is mostly reflected due to collective screening action of electrons. Under these conditions, electronic excitation in the molecule may be disregarded, since the radiation frequency is too low, and the effect of the field is to adiabatically modulate the potential energy for each quasiparticle level in the leads, that means the energy levels are rigidly shifts over time while maintaining the same population across the levels. In other words carriers distribution remains the same. Studying charge transport considering these assumptions is equivalent to study tunneling transport through a time dependent potential barrier [3]. One of the most known and most studied solution of the problem was proposed by P. K. Tien and J. P. Gordon in 1963 [27] and predicts the following physical process: Electrons in the source can absorb or emit a certain number of energy quanta and then tunnel elastically across the junction through molecular orbitals (or better through transmission channels) that could have been not available for their starting energy. This mechanism is called adiabatic photo-assisted tunneling and is responsible for the opening of additional conduction channels in the single-electron transmission function [10] as it is depicted in fig. 1.8(a). The Tien-Gordon (TG) model will be accurately described in the next chapter since it is the most employed model in a large number of experimental papers. It is important to understand it and know its limitations. A crucial point to underline is that models like TG do not consider field quantization, therefore it is not correct to talk about absorption or emission of ‘real’ photons from electrons. It is better talking about absorption or emission of electromagnetic energy quanta which modulate the quasiparticle energy [28].

An other interesting observation on adiabatic processes is that they could be equivalently realized by mechanical perturbation, for instance acoustic waves, with oscillation frequency in the same range of microwaves. This is possible since only the potential energy of the quasiparticle states is involved in the process and it can be modulated in other ways in addition to the electromagnetic one.

It is worth underling that the subdivision between adiabatic and non-adiabatic processes is merely arbitrary because in molecular junction the molecular orbitals, due to strong coupling with the electrodes, hybridize with the frontier orbitals of the metal, with a consequent broadening of the molecular density of states. Electronic transitions in the molecule can happen also for photon energy smaller than the HLG and thus non-adiabatic phenomena should be consider also in the

low frequency regime if strong coupling is considered. On the other hand, this division can be considered more correct in the case of weakly coupled molecules.

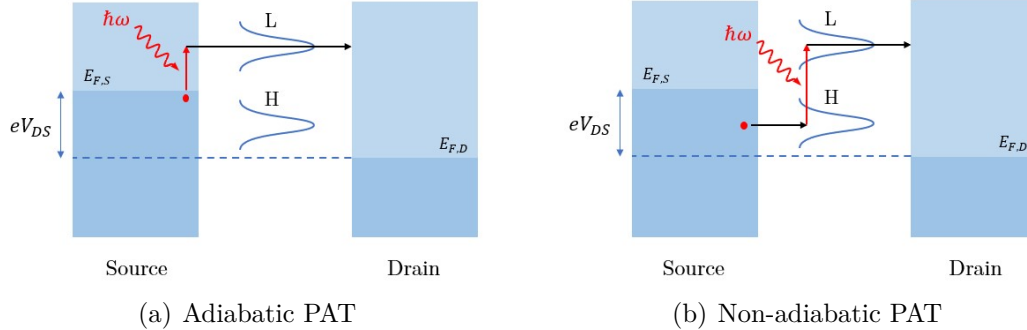


**Figure 1.8:** Photo-assisted tunneling mechanisms. (a) In adiabatic PAT the energy of electrons inside the leads is adiabatically modulated, inducing the absorption or emission of energy quanta, which can lead to elastic tunneling through available molecular orbitals. (b) In non-adiabatic PAT internal molecular transitions are allowed, thus transport mechanism changes from elastic to inelastic. During tunneling electrons can absorb or emit photons with consequent change of transmission channel.

### Non-adiabatic (resonant) photo-assisted tunneling

Non-adiabatic processes correspond to transport mechanisms in which inter-level transitions between molecular orbitals can happen, typically considering radiation frequency in the optical range. In fig. 1.8(b) this type of PAT is described. Initially an electron with energy corresponding to available states in the molecule can tunnel into it. Then, while crossing the gap between the electrodes, it can absorb (the case of fig. 1.8(b)) or emit photons with consequent transmission through another channel. This mechanism can lead in general to a ‘resonant’ current amplification due to opening of additional conduction channels. Resonant optical transitions can lead also to other effects depending on the symmetry of the junctions. These effects will be commented below after having described possible transmission symmetries of a molecular junction.

As said above, the photon energy involved in these processes is in the optical range, that is also the range of LSPs resonance excitation. The presence of a molecule near the LSPs inside the electrodes supplies additional channels for energy transfer by means of photo-assisted tunneling events. Therefore, in the case of molecular junctions, two additional damping mechanisms set in and complete the list of non-radiative damping processes, that are represented in fig. 1.9. Panel (a) depicts the already described Landau damping, while (b) and (c) are new processes described as follows:

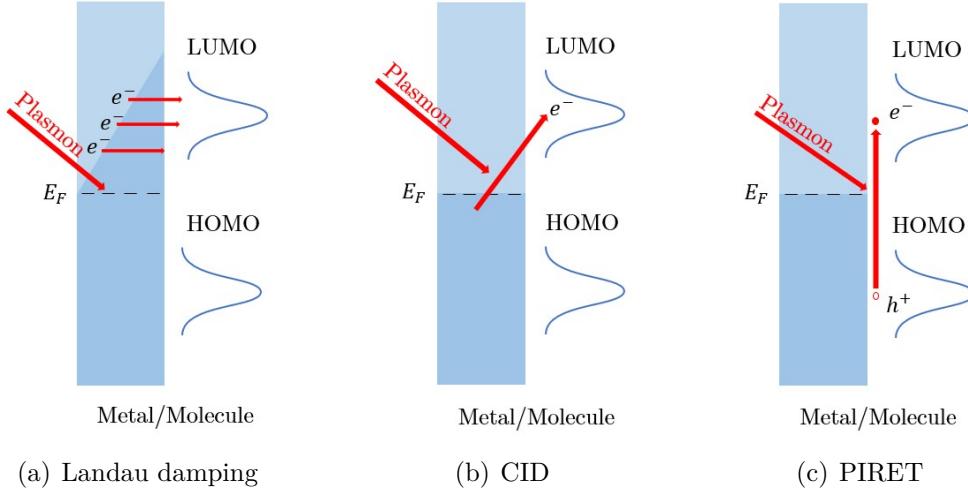


**Figure 1.9:** Non-radiative damping processes. (a) Landau damping is responsible of hot electrons generation, which can then tunnel through the junction increasing the total current. (b) Chemical Interface Damping (CID) is responsible of charge transfer from the electrode to the molecule by absorption of plasmonic quanta. This process is similar to adiabatic PAT, but here the process is triggered by plasmonic response of the system. (c) Plasmon-Induced Resonance Energy Transfer (PIRET) corresponds to energy transfer from the LSP to the molecule through dipole-dipole interaction. In this way electrons in occupied molecular orbitals can be excited in unoccupied ones and then tunnel through the electrodes. This process is equivalent to a non-adiabatic PAT, but here energy quanta are supplied by a plasmon mode.

- i. *Chemical Interface Damping (CID)*: Process similar to hot electron generation, but in this case carriers are directly excited, due to absorption enhancement at LSP resonance, into electronic levels of the attached molecule [29]. Then the excited electrons can tunnel elastically through the molecule at an energy greater than the one of their initial state. This process is similar to the adiabatic PAT, but in this case the transport mechanism is triggered by the plasmonic (local) field and not by the incident one.
- ii. *Plasmon-Induced Resonance Energy Transfer (PIRET)*: This mechanism results from the dipole-dipole interaction between the localized excited plasmon and the molecule. This interaction obeys a power law as a function of distance, thus it is expected to be more charge-transfer efficient than hot electron tunneling, contribution that decreases exponentially with distance [29]. More specifically, the energy exchanged between the excited plasmon and the molecule induces a transition for an electron to an unoccupied molecular orbitals at higher energy. Then this electron can tunnel towards the contacts contributing to the overall current. This process is analogous to non-adiabatic PAT which is here driven by the plasmonic response of the system. PIRET

becomes more important when there is an overlapping between LSP resonance and molecule absorption spectrum, considering a sufficiently slow decay of the LSP to maintain the collective behavior [29].

It is worth notice that CID and PIRET are bidirectional mechanisms since energy exchange can also happen from the molecule to the plasmonic mode. In these cases they are not damping processes but exciting mechanisms. For instance, if an electron inside the molecular channel is in an excited state due to absorption of photons from the incident field, de-excitation is possible due to coupling between the molecule and the LSP, that in this case is excited by the release of energy from the electron.

What just described concludes the discussion on LSP damping processes and underlines their important role in PAT. Although these phenomena should always be taken in consideration when analyzing a real system, in Chap. 2-3 only the effect of field amplitude amplification due to LSP resonance excitation is considered in order to simplify the description of charge transport.

## Symmetries

Before analyzing most studied applications exploiting PAT, an other important argument should be addressed that regards possible symmetries characterizing a system. It is known that in quantum mechanics a system is described by an Hamiltonian  $\hat{H}(\vec{x}, t)$  that depends on spatial and time variables. Considering under analysis a single-molecule junction, in the absence of radiation the system can be described in stationary condition by a single electronic transmission coefficient  $T(E)$ , that is identical for an electron transmitted from the left to the right electrode and vice versa. Instead, when an incident radiation is considered, the driven system cannot be described by a single transmission coefficient, but is characterized by two transmission spectra which depend on time: one for the electrons tunneling from left to right ( $T_{RL}(t, E)$ ) and one for electrons tunneling from right to left ( $T_{LR}(t, E)$ ). In general  $T_{RL}(t, E) \neq T_{LR}(t, E)$  and, depending on symmetry, a certain relation is established between them. As it will be later proved in Chap. 2, these transmission spectra can be expanded in Fourier series, thus transforming the time dependent problem to an independent one. The components of the expansion are expressed as  $T_{RL}^{(n)}(E)$ ,  $T_{LR}^{(n)}(E)$  that refers to processes involving  $n$  photons: absorption if  $n > 0$  or emission if  $n < 0$ . This procedure can be done only if the electron-electron interaction is considered by a mean field and not explicitly inside the Hamiltonian of the molecule (see [30]).

To understand how these coefficients vary with symmetry, three different operators acting on space and time variables are introduced:

- Parity operator  $\Rightarrow \hat{S}_P : \vec{x} \rightarrow -\vec{x}$

- Time-reversal operator  $\Rightarrow \hat{S}_T : t \rightarrow -t$
- Generalized time shift operator  $\Rightarrow \hat{S}_G : t \rightarrow t + t_0$

A system obeys a symmetry if its Hamiltonian is invariant under a symmetry operation  $\hat{S} = (\hat{S}^\dagger)^{-1}$ , i.e. if  $\hat{S}^\dagger \hat{H}(\vec{x}, t) \hat{S} = \hat{H}(\vec{x}, t)$  [30].  $\hat{S}$  can be one of the operators described above or can be a combination of them. In particular, three symmetries are described here below and related transmission processes are depicted in fig. 1.10.

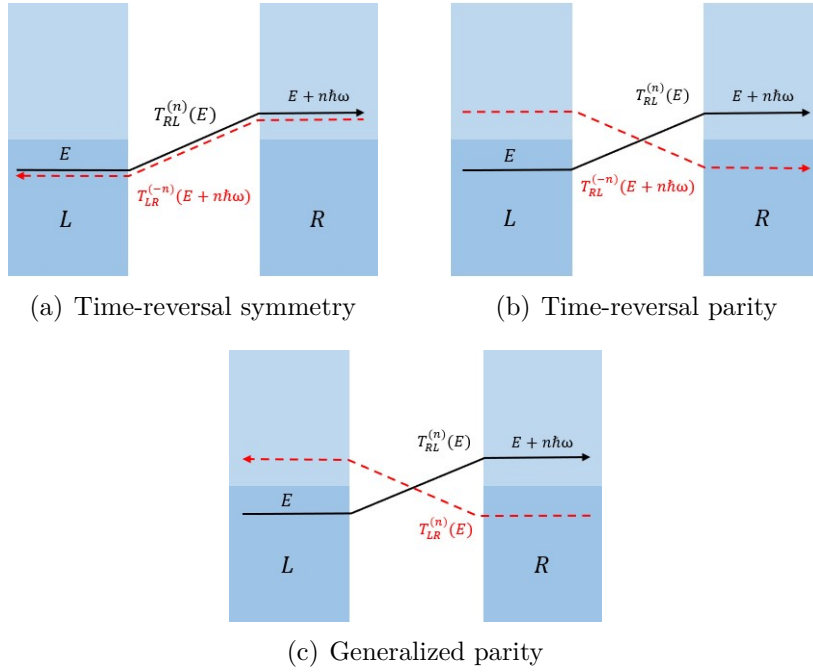


**Figure 1.10:** Scattering processes representing an electron with energy  $E$  transmitted through the junction after absorbing  $n$  energy quanta. In the panels are described also symmetry related processes (red dashed lines) corresponding to (a) time-reversal symmetry, (b) time-reversal parity and (c) generalized parity.

- a. Time-reversal symmetry. The symmetry operator correspond to  $\hat{S}_T$  and the Hamiltonian obeys the relation  $\hat{H}(\vec{x}, t) = \hat{H}(\vec{x}, -t)$ . As a consequence, the transmission coefficients obey the relation  $T_{RL}^{(n)}(E) = T_{LR}^{(-n)}(E + n\hbar\omega)$ , that means scattering processes represented in fig.1.10(a) occurs with the same probability. Going into more detail, time-reversal symmetry allows to state that an electron with initial energy  $E$ , transmitted from left to right absorbing (emitting)  $n$  energy quanta, can return to its initial state if time is rewinded, thus its time reversal counterpart is equivalent to an electron with initial

energy  $E + n\hbar\omega$  transmitted from right to left that emits (absorbs)  $n$  energy quanta to reach a final state at energy  $E$ , that corresponds to the initial one of the considered electron. Time-reversal is typically broken by a magnetic field (not considered in this work) since it is described by an axial vector that under time reversion changes its direction [30]. It is worth notice that a time-independent system in the absence of magnetic fields is a particular case that respects this symmetry since all components of transmission with  $n \neq 0$  are zero and that  $T_{RL}^{(0)}(E) = T_{LR}^{(0)}(E) = T(E)$  [30].

- b. Time-reversal parity. The symmetry operator is defined as  $\hat{S}_{TP} = \hat{S}_T \hat{S}_P$  :  $(\vec{x}, t) \rightarrow (-\vec{x}, -t)$  that is a combination of time-reversal and parity operators. In this case the Hamiltonian obeys also spatial parity which corresponds to systems with identical molecule-electrode charge transfer rate for both sides of the junction. The reasoning about time-reversal symmetry can be repeated but with additional interchanging between left and right, as it is shown in fig. 1.10(b), with transmission probabilities related as  $T_{RL}^{(n)}(E) = T_{RL}^{(-n)}(E + n\hbar\omega)$ . It is important to highlight that this symmetry relates two scattering processes going in the same direction, thus implying possible correlation effects which are intriguing and with possible applications for non-adiabatic electron pumping (see below) [30].
- c. Generalized parity. The corresponding symmetry operator is  $\hat{S}_{GP} = \hat{S}_G \hat{S}_P$  :  $(\vec{x}, t) \rightarrow (-\vec{x}, t + \mathcal{T}/2)$  that combines the parity operator with a time shift by half a driving period of a simple sinusoidal or cosinusoidal monochromatic field [30]. It is possible to demonstrate that, for systems characterized by this symmetry, transmission probabilities obey the relation  $T_{RL}^{(n)}(E) = T_{LR}^{(n)}(E)$ , that means there is no difference between right and left electrodes considering the same scattering process identified by the index  $n$ . Here below the implications to have this symmetry will be given and, for the rest of this work, it will be the symmetry characterizing the simulated molecular junctions.

To recap what just said, time-reversal symmetry is always present, except when are considered the effects of a magnetic field, whereas parity is present when there is no difference between right and left (in the context of molecular junctions when lead-molecule coupling is the same for left and right electrode). An additional symmetry can characterize the system when an incident electric field can be expressed in a simple sinusoidal or cosinusoidal form, thus leading to identical transmission probabilities ( $T_{RL}^{(n)}(E) = T_{LR}^{(n)}(E)$ ). With this in mind is now possible to describe possible application of field driven molecular junctions.

## Applications

Photo-assisted transport is involved in a lot of different applications, some of them of particular interest for researchers because regarding energy harvesting devices, others concerning ‘standard’ optoelectronic devices such as light emitters or detectors. Below most studied applications in the framework of molecular junctions are presented, further justifying the importance of studying their interaction with light.

- *Optical rectification*

A suitably polarized electric field incident to a (un)biased molecular junction can induce an additional AC current with time average different from zero, thus adding a contribution also to DC current through photo-assisted tunneling. This mechanism is equivalent to current rectification, which can be demonstrated starting from conventional circuit theory. Considering adiabatic limit, i.e. a microwave radiation, the incident field can be modeled as an oscillating bias potential. The reason is that the radiation wavelength is larger than the size of the gap, therefore most of the field is incident on the contacts inducing a potential drop. This is equivalent to apply an AC potential to the junction, that is of course a simplification which can be done under certain conditions, described later in Chap. 2. Under this approximation, it is possible to express the potential applied to an electrode as  $V(t) = V_{DC} + V_{AC} \cos(\omega t)$  and considering  $V_{AC} \ll V_{DC}$  the current can be expanded in powers of  $V_{AC}$  in the following way:

$$I(V) = I(V_{DC}) + \left. \frac{\partial I}{\partial V} \right|_{V_{DC}} V_{AC} \cos(\omega t) + \frac{1}{2} \left. \frac{\partial^2 I}{\partial V^2} \right|_{V_{DC}} V_{AC}^2 \cos^2(\omega t) + \dots$$

Truncating at second order and expanding with trigonometric formulas the squared cosine, it is possible to rewrite the above expression as:

$$I(V) = I(V_{DC}) + \left. \frac{\partial^2 I}{\partial V^2} \right|_{V_{DC}} \frac{V_{AC}^2}{4} + \left. \frac{\partial I}{\partial V} \right|_{V_{DC}} V_{AC} \cos(\omega t) + \left. \frac{\partial^2 I}{\partial V^2} \right|_{V_{DC}} \frac{V_{AC}^2}{4} \cos^2(2\omega t)$$

Looking at the final expression it is possible to identify the second term (time-independent) as an additional contribution to DC current, but only if the second derivative of current with respect to the potential is different from zero. This is generally true for a given applied bias, thus a photocurrent is established through an *optical rectification*. Nevertheless, a net current in short-circuit condition is developed only if  $\left. \frac{\partial^2 I}{\partial V^2} \right|_{V_{DC}=0} \neq 0$ . The demonstration given above is useful to understand that the behavior of molecular junctions subjected to small oscillating potentials are not so different from more known rectifiers and that with a simple reasoning is possible to justify the additional photocurrent resulting from the

irradiation of the junction. Nevertheless, molecular systems are much more complex and it is not always possible to consider the case of small oscillating potentials. In particular, in the field of mesoscopic physics, the net short-circuit current described above assumes the name of quantum ratchet, that is another name to identify rectification at zero bias or, better, the conversion of AC forces into directed motion without any net bias [30]. Quantum ratchets are based on quantum mechanical processes (like PAT in molecular junctions) and, depending on the radiation frequency involved, they can be identified by different names such as adiabatic and non-adiabatic electron pump. Adiabatic electron pumps are ratchets based on adiabatic PAT, thus a net short-circuit current can be generated while the system does not abandon its ground state [31]. On the other hand, non-adiabatic electron pumps refer to ratchets based on resonant PAT. However, both types of pump are characterized by breaking of generalized parity, which can be done in two different ways:

- Considering a level structures coupled asymmetrically with the electrodes and under the influence of a harmonic incident radiation by means of dipole-field interaction [30]. This can be achieved in molecular junctions considering different anchoring groups for left and right contacts. In this case the device is called ‘rocking ratchet’.
- Considering a symmetric system where generalized parity is broken dynamically by the incident field that is a mix of higher harmonics [30]. For example this can be achieved by an electric field with the form  $E(t) = E_{0,1} \cos(\omega t) + E_{0,2} \cos(2\omega t)$ . Shifting time by  $\mathcal{T}/2$ , the fundamental harmonic assumes the same value whereas the higher one changes sign, therefore generalized parity is broken.

The need of symmetry breaking can be understood following simple reasoning for both types of electron pump. In adiabatic pump the asymmetry allows to have  $\left. \frac{\partial^2 I}{\partial V^2} \right|_{V_{DC}=0} \neq 0$ , thus developing a net short-circuit current that in open-circuit condition correspond to a photo-voltage. Instead in non-adiabatic pumps the asymmetry can be reflected into different coupling of the levels between left and right. For example, if in a molecular junction the HOMO level is coupled more strongly to one electrode whereas the LUMO level is coupled more strongly to the other, a photo-voltage can establish in unbiased condition. This can intuitively be understood in the following way. A photon impinging on the junction, having an energy equal to the HLG, can excite an electron from the HOMO to the LUMO. Then, in the higher energy orbital, it can be transmitted preferentially to one of the two electrodes and therefore developing a net current.

To the light of what just said, practical applications in the energy-harvesting field exploiting asymmetric single-molecule junctions are possible. A very recent article [22] published in August 2021 by a research group of the University of Cambridge

working at the *NanoPhotonics Centre*, is one of the first experimental works that demonstrates the establishment of a non-zero photocurrent under short-circuit condition for asymmetric molecular junctions. More into detail, they considered a type of geometry called NanoParticle on Mirror (NPoM) where one electrode is a gold substrate while the other is a gold nanoparticle. The gap is filled by a SAM which can be composed of symmetric or asymmetric molecules. For the symmetric case they considered molecules such as alkanedithiols and verified the generation of photocurrent, for finite bias, caused by LSP field enhancement. On the other hand, considering alkanes with different anchoring groups at the two sides (for example thiol and amine group) or considering ferrocene-based alkanethiol, they measured an optical response in the unbiased molecular junctions which is promising for future photovoltaic applications. Moreover, they identified good candidates in conjugated oligophenylene molecules with asymmetric functional groups to maximize the optical responsivity.

For what concerns symmetric junctions, a straightforward application is to use single-molecule junctions as photodetectors. There is a number of experimental papers related to measurement of photocurrent in biased molecular junctions. For example in [32], [20], [33] Y. Selzer and coworkers analyze the possible excitation of surface plasmons in Suspended Wire Molecular Junctions (SWMJ) and in Squeezable Break Junctions (SBJ) while considering symmetric molecules such as alkanedithiols and 2,7-diaminofluorene. In their works they measured current amplification when the junctions were illuminated and justified their results taking in consideration surface plasmons excitation at the considered optical frequency. These works of course imply a possible application in the field of photodetectors, however they did not study the single-molecule junctions with the methodology used for detectors, thus studying quantum efficiency, responsivity, limit of detection, temperature dependence and also noise analysis. Nevertheless, there exists a recent work dated December 2020 [34] by S. Saxena *et al.* who designed a photodetector based on a SAM-junction. The considered SAM were composed by nitroazobenzene oligomers or two-component oligomers (thus a bilayer) such as anthraquinone-bisthienyl benzene (AQ-BTB) or anthraquinone-tetraphenyl porphyrin (AQ-TPP). The length of these molecules are in the range from 14.6 nm to 100 nm, therefore coherent tunneling is not guaranteed in these devices. However, longer molecular layers allow to have a greater area interacting with the field, that is an advantage in photo-detectors. The measured responsivity of the resulting junctions is not competitive with other organic detectors made of thicker molecular films or with conventional solid-state devices. Despite this, molecular junctions composed by short molecules allow to have low dark current, therefore further reducing the limit of detection. As written by S. Saxena *et al.* “The wavelength selectivity, potential response to NIR and UV light outside the range of silicon detectors, low voltage operation, and low dark noise of molecular photodetectors are advantages which

may be tailored to specific applications”.

- *Light emitting single-molecule junctions*

Other important components in optoelectronics are light sources and an obvious question is if it is possible to obtain them using molecular junctions. As already mentioned, photo-assisted tunneling can occur through absorption or emission of energy quanta, therefore theoretically seems possible to develop light emitting single-molecule junctions. However, the emission efficiency is in general low due to strong coupling with metallic electrodes that establishes highly efficient non-radiative channels. Therefore carriers are elastically transmitted and the emission is *quenched*. There are several procedure to decouple the molecule from metallic surfaces to avoid quenching [35] such as:

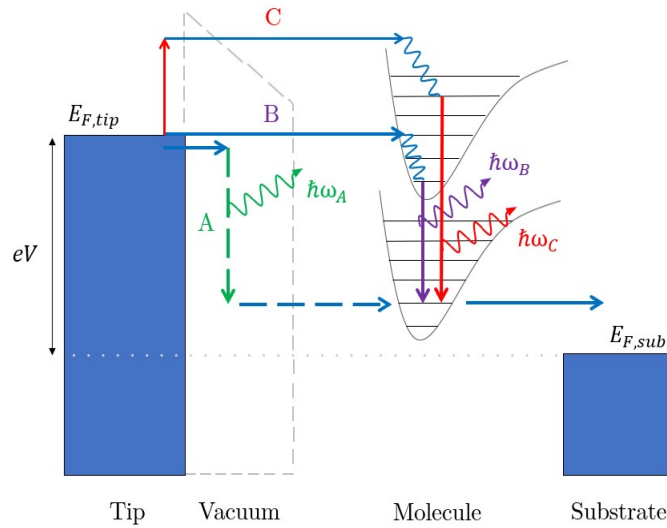


**Figure 1.11:** Emission processes depicted on an energy levels diagram of a molecular junction studied with STM. Process (A) corresponds to direct excitation of localized surface plasmons in the tip. (B) refers to transitions between electronic/vibrational levels inside the bias window that correspond to emitted photons with energy  $\hbar\omega \leq eV$ . The emitted radiation can couple to plasmon modes of the tip that are therefore indirectly excited. (C) Hot carriers tunneling across the junction can also emit photons similarly to process (B) but their energy can be  $\hbar\omega > eV$ .

- Inserting a thin (in)organic insulating layer, as metal oxides, between molecule and electrodes.
- Adding a molecular layer between molecule and electrodes.
- Using ‘molecular’ approaches like synthesize molecules with particular features that aim to reduce charge transfer coupling. For example is possible to produce

a molecule with a tripodal anchor at one side, thus reducing coupling (see reference [10]).

- Lifting a molecular wire laid on a substrate with a STM tip, thus reducing coupling at the tip side. An example in literature is described in [36] where a polythiophene molecular wire is considered.
- Changing metallic electrodes with carbon-based contacts, for example using CNTs that lead to a smaller lead-molecule coupling [10].

Although what said above is relevant in practice, from a theoretical point of view light emission can occur following different transport mechanisms. The latter are now described taking as example a STM experiment that is represented in fig. 1.11. An electron tunneling from the tip to the substrate can follow three different paths (A,B and C) involving light emission:

- A. An electron lying around the Fermi level can couple with a surface plasmon mode of the tip. Before tunneling across the gap, it loses energy in favor of the plasmon mode, that is therefore excited. Then, the electron tunnels through transmission channels located at lower energy, whereas surface plasmon starts

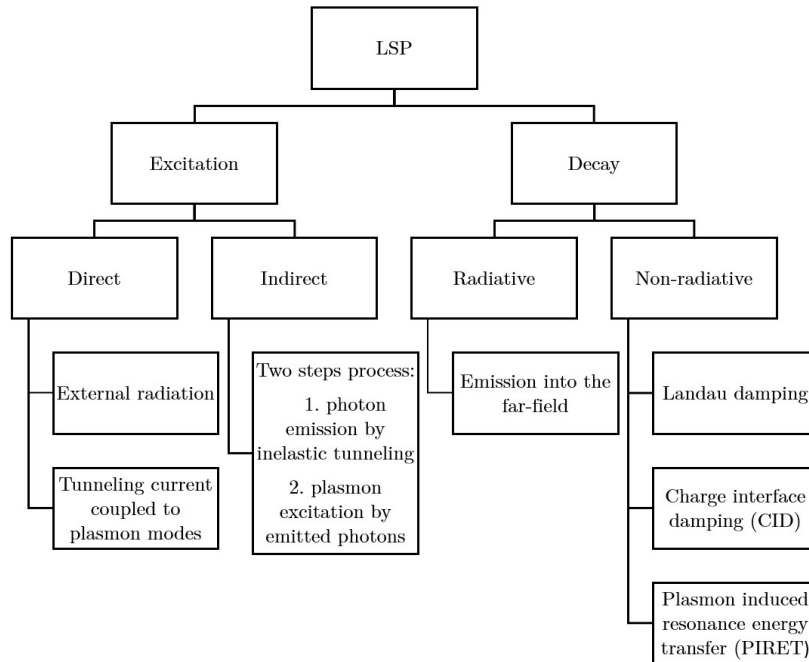


**Figure 1.12:** Diagram summarizing main processes involved in excitation and decay of localized surface plasmons.

to decay. If radiative damping process is efficient, a far-field photon is emitted and has energy equal to the one lost by the electron. This mechanism can be summarized saying that tunneling current is coupled to a plasmon mode, which is 'directly' excited.

- B. If two molecular levels are located in the bias window, i.e. the energy interval between the Fermi levels of the electrodes, they will both be partially occupied and, if optical transitions between them are not forbidden by selection rules, transitions from the higher-energy level to the lower-energy level will occur resulting in photon emission [28]. Moreover, vibrational levels of corresponding electronic states are likely involved during transmission, thus broadening the actual emission spectrum of the single-molecule junction. For this process the photon energy respects the relation  $\hbar\omega \leq eV$  since both levels must belong to the bias window of size  $eV$ . In this case  $V$  is the magnitude of the bias applied between tip and substrate, whereas  $e$  is the elementary charge. It is fundamental to underline that the emitted photons can correspond to an actual light source that is detected in the far-field, but can also couple to a plasmon mode. In this case a plasmon is *indirectly* excited by a two step process: First photons are emitted through inelastic tunneling and then the emitted radiation excites a plasmon mode. If radiative, the effects of plasmon excitation is an enhancement of emitted field but with a reshaped spectrum. In the context of molecular plasmonics, direct excitation is preferred from the indirect one since it does not depend on electronic transitions which occur over a nanosecond scale. This allows to design devices that are faster and not band limited by the energy difference between the levels.
- C. Hot electrons lying at energy greater than the tip Fermi level can first be transmitted to electronic/vibrational states outside the bias window and then, similarly to path B, they can emit photons reaching a lower-energy state. The main difference is the constraint on photon energy. For this process  $\hbar\omega > eV$ , thus it is not limited by the applied bias. Besides hot carriers transport there are also other mechanisms involving emission of photons with  $\hbar\omega > eV$ . For example, this type of emission has been observed in [37] for a single C<sub>60</sub> molecule. The authors attributed the emission above threshold to the possible contribution of 2-electron processes. In general this phenomenon can likely occur when electron-electron interaction is strong and thus charge fluctuations on the molecule give rise to additional noise at optical frequencies, beyond the shot noise of the current that is injected to the tip [37].

The above discussion concludes the description of light emitting single-molecule junctions, which surely have a crucial rule for the design of fully molecular photonic circuits, but also complete the description of mechanisms involved in LSPs

(summarized in fig. 1.12).

- *Other applications*

Over the years a great number of applications exploiting PAT have been investigated from a theoretical point of view, but that do not have a clear experimental evidence. The research group composed by S. Kohler, J. Lehmann and P. Hänggi studied for years molecular wires using a simplified model considering tight-binding approximation. With this model, they predicted phenomena not mentioned above. For example in [38] they described a possible application of PAT as current router. They verified that current flows through different electrodes by varying the incident field polarization. The same phenomenon is described by U. Peskin and M. Galperin in [39] but considering a zero dimensional model (0D) in the framework of NEGF (Non-Equilibrium Green's Function). An other interesting application is described by Kohler and coworkers in [30] where coherent destruction of tunneling (CDT) is predicted when considering an illuminated junctions. This has of course a direct application in molecular transistors since one can imagine to exploit radiation to reduce the off current and thus increasing the  $I_{ON}/I_{OFF}$  ratio. However, both CDT and molecular routers do not have experimental evidence, therefore they are not described here more into detail.

This concludes the introduction to the field of illuminated single-molecule junctions, hoping to have given exhaustive reasons why it is important to study PAT. Next chapter is focused on the description of the main physical models used in literature to study the contribution of PAT in single-molecule junctions. They will be formally introduced after having briefly described charge transport in single-molecule junctions using a simplified zero-dimensional model that can be generalized in the language of NEGF. The description of these models is crucial since their implementation in MATLAB<sup>®</sup> would be the topic of Chap. 3.



## Chapter 2

# Photo-assisted tunneling models

In this chapter I will describe three models, starting from the simplest one and gradually increasing complexity, that are most used in literature to study PAT through single-molecule junctions. Before doing this, an introduction to conduction in 0D-systems (such as molecules) is given in order to have a complete picture of conduction in molecular junctions, but also because in Chap. 3 this simple model, based on *independent levels*, would be the base on which different PAT mechanisms will be implemented. In the following chapters I will use as convention “e” to indicate the elementary charge and “i” for the imaginary unit instead of “j” that is more used in the electronic engineering field. This is justified by the fact that molecular electronics is a “hot” topic also for physicists, especially when light is involved. The majority of papers are signed by them, hence I decided to align with their convention.

### 2.1 Conduction in 0D-systems

In systems like nanocrystals or molecules the electrons are confined along the three dimensions that are in the order of  $\lambda_{DeB}$ , i.e. the characteristic De Broglie wavelength of the electrons. These 0D-systems are generally called quantum dots and are characterized by discrete energy levels whose corresponding electronic wavefunctions are localized in space. Nevertheless conduction is possible when two metallic electrodes, representing big reservoirs of electronic states, are put close to the system that, in our case, is represented by a molecule bridging the electrodes. The electronic wavefunctions corresponding to molecular orbitals would no more be localized on the molecule but they would spread into the contacts. Similarly, the eigenfunctions of the frontier atoms of the metals would ‘spill over’

into the molecular channel. The resulting effect is that the levels inside the molecule ‘gains’ part of the contact states, thus the molecular DOS is no more a sequence of delta functions (corresponding to discrete levels) but would be broadened due to the acquired states. This can be understood also taking in consideration the uncertainty principle. When isolated, the escape time of an electron from the molecule is infinite, thus the spread in energy of the corresponding energy state is infinitesimal. On the other hand, if the molecule is put near two metallic contacts, the same electron can leave the molecule, thus having a finite escape time, that corresponds to a finite spread of the energy level. Right from the uncertainty principle is possible to define a coupling factor, between the molecule and a lead, which is related to the escape rate of electrons and is expressed as  $\gamma = \hbar/\tau$  where at the denominator there is the electron escape time.

This mechanism is in general referred as *hybridization* of molecular orbitals with the ones of the contacts and occurs especially when exists a strong coupling between the molecule and the metals, that means when the molecule is covalently bonded at the two sides. Under this condition is possible to describe transport in single-molecule junctions using a simple model based on independent conduction of different energy levels. The latter must be computed with *ab-initio* simulations, such as Density functional theory (DFT), or semi-empirical simulations, like extended Hückel theory (EHT), since other approximations, such as bounding box, do not allow to retrieve quantitative results in the case of molecular junctions. Here the electronic levels of the molecule are considered as already obtained from an *ab-initio* simulation of the electronic structure and then used to compute charge transport. The independent levels model will now be introduced, first focusing on the conduction of a single level  $E_i$ , including or not spectral broadening, and then generalizing the results. The following discussion is taken from the book “Quantum Transport. Atom to Transistor” by S. Datta [40], that is a simple but effective introduction to quantum transport, and from the notes of course “Nanoelectronic Systems ” taught by professor M. Graziano and G. Piccinini during academic year 2020-2021 at Politecnico di Torino.

### Conduction through a discrete energy level

The situation considered in this paragraph is the one shown in fig. 2.1 where only one energy level enters, for now, in the calculation. The level is strongly coupled to the electrodes that are indicated with the conventional names: source and drain. A bias is applied between them, therefore shifting their Fermi levels and creating the so called bias window (BW), that is the energy range between the Fermi levels of the contacts. Since source and drain are characterized by different Fermi-Dirac distributions, the system is in a non-equilibrium state and each contact tries to bring the molecular channel (i.e. the single level in this case) in equilibrium to itself.

To be more precise, the source keeps pumping electrons into the channel, since it has the higher Fermi level, hoping to establish equilibrium. On the other hand, drain keeps pulling electrons out of the channel in order to bring the system to its own equilibrium. In the end equilibrium is never established and the molecular channel is forced into a non-equilibrium state.

It is possible to quantify the net flux between the contacts and the molecule considering a discrete energy level  $E_i$  inside the BW (broadening is not considered at the moment):

- The source, identified from now on as contact 1 (S=1), would like to see an average number of electrons  $N_i$  inside the i-th level equal to  $2 \cdot f_{FD}(E_i - E_{F,1})$  (factor 2 for spin degeneracy). The net current across the left interface is proportional to  $2 \cdot f_{FD}(E_i - E_{F,1}) - N_i$ :

$$I_1 = \frac{e\gamma_{i,1}}{\hbar}(2 \cdot f_{FD}(E_i - E_{F,1}) - N_i) \quad (2.1)$$

- Similar reasoning applies to drain (from now on D=2), whose net current crossing right interface is:

$$I_2 = \frac{e\gamma_{i,2}}{\hbar}(2 \cdot f_{FD}(E_i - E_{F,2}) - N_i) \quad (2.2)$$

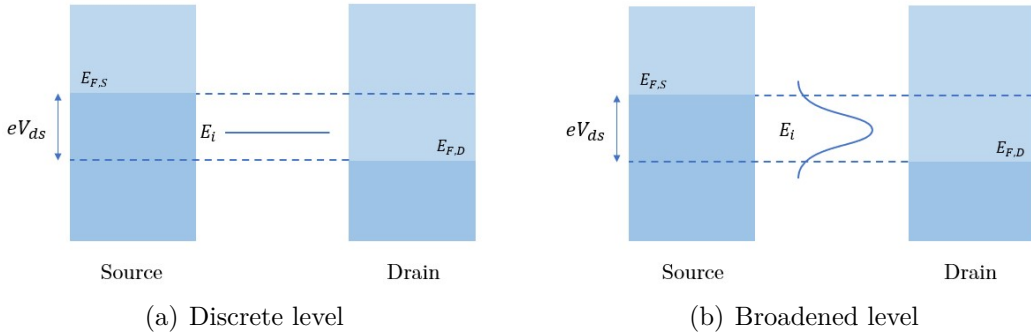


**Figure 2.1:** Band diagram for a single conducting energy level where in (a) is discrete (unphysical situation since the level is strongly coupled with the electrodes) and in (b) broadening is taken in consideration.

Looking at eq. 2.1 and 2.2 is possible to make some observations. First, in steady-state condition the occupation of the level inside the BW would be something intermediate between the distribution of the contacts. Secondly, the ratios  $\gamma_{i,1}/\hbar$  and  $\gamma_{i,2}/\hbar$ , having in mind what mentioned above, are related to the escape time of an electron from the corresponding i-th level. It is known also that  $\gamma_{i,1}$  and  $\gamma_{i,2}$  are

the coupling factors that arises from contacting the molecule with the electrodes. These factors will be important in the following when addressing the broadening problem.

At steady-state the net currents flowing in the left and right electrode are equal in magnitude but have opposite sign  $I_1 = -I_2$ , that implies also  $I_1 + I_2 = 0$ . Inserting in this relation eq. 2.1 and 2.2 we obtain an expression for the average number of electrons in level  $i$ :

$$N_i = 2 \cdot \frac{\gamma_{i,1}f_1(E_i) + \gamma_{i,2}f_2(E_i)}{\gamma_{i,1} + \gamma_{i,2}} \quad (2.3)$$

where  $f_1(E) = f_{FD}(E - E_{F,1})$  and  $f_2(E) = f_{FD}(E - E_{F,2})$  for brevity. This equation confirms what observed above, i.e. the average occupation of the  $i$ -th level corresponding to energy  $E_i$  is a weighted average of what the two contacts would like to impose.

Putting the expression for  $N_i$  in eq. 2.1 it is possible to retrieve a formula for the current  $I = I_1 = -I_2$  under steady-state:

$$I = \frac{2e}{\hbar} \frac{\gamma_{i,1} \cdot \gamma_{i,2}}{\gamma_{i,1} + \gamma_{i,2}} [f_1(E_i) - f_2(E_i)] \quad (2.4)$$

Starting from this equation we can make some considerations:

- If  $f_1(E_i) = f_2(E_i)$  no current is flowing and this is reasonable since the system is at equilibrium.
- If  $E_i \gg E_{F,1}, E_{F,2}$  the level is well above the electrochemical potentials of the electrodes, that implies  $f_1(E_i) \simeq f_2(E_i) \simeq 0$ . Therefore no net current is flowing and the level is empty ( $N_i = 0$ ).
- If  $E_i \ll E_{F,1}, E_{F,2}$  the level is well below the electrochemical potentials of the electrodes, that implies  $f_1(E_i) \simeq f_2(E_i) \simeq 1$ . Again no net current is flowing, but in this case the level is occupied by two electrons ( $N_i = 2$ ).
- $E_i \in \text{BW}$  implies  $f_1(E_i) \neq f_2(E_i)$  that is the only case allowing current to flow.

Summarizing, current flow is the result of a continuous transfer of electrons by means of tunneling across the 0D-system. Electrons in the source develop a net current only reaching the drain through energy levels inside the BW.

To include broadening of the energy levels in this derivation is convenient to recall the concept of Density Of States (DOS), that is the number of states available for a certain energy value. Considering a discrete level in a 0D-system, the DOS just consists of a delta function located at the energy of the level:

$$DOS_i(E) = \delta(E - E_i) \quad (2.5)$$

where the subscript ‘ $i$ ’ is used to remember that in this case the DOS is referred to only one level.

With this expression we can rewrite eq. 2.4 and 2.3 exploiting the properties of delta function. We can include the DOS in these equations by inserting an integral over energy and evaluating the Fermi-Dirac distributions at the integrating variable  $E$ :

$$N_i = \frac{2}{\gamma_{i,1} + \gamma_{i,2}} \int_{-\infty}^{+\infty} DOS_i(E) [\gamma_{i,1} f_1(E) + \gamma_{i,2} f_2(E)] dE \quad (2.6)$$

$$I = \frac{2e}{\hbar} \frac{\gamma_{i,1} \cdot \gamma_{i,2}}{\gamma_{i,1} + \gamma_{i,2}} \int_{-\infty}^{+\infty} DOS_i(E) [f_1(E) - f_2(E)] dE \quad (2.7)$$

Now we are ready to consider the case of level broadening represented in fig. 2.1(b).

### Level broadening

As already said above, broadening occurs when there is a strong coupling between the molecule and the contacts. Moreover, the parameter related to it is  $\gamma_i$  (corresponding to  $i$ -th energy level) that is also proportional to the electron escape time. Increasing the coupling between molecule and electrodes would also increase  $\gamma_i$  which is now exploited to define the level spread in energy. In general broadening is described by an energy-dependent function  $\gamma_i(E)$  which can be computed by more sophisticated techniques such as NEGF. As first approximation,  $\gamma_i$  is considered constant (as done above) and is possible to associate a Lorentzian function to the corresponding DOS of the level. Having in mind that the coupling factor results from the contributions of both electrodes ( $\gamma_i = \gamma_{i,1} + \gamma_{i,2}$ ), the broadened DOS is expressed as follows:

$$DOS_i^B(E) = \frac{\frac{\gamma_i}{2\pi}}{(E - E_i)^2 + (\frac{\gamma_i}{2})^2} \quad (2.8)$$

Equations 2.6 and 2.7 are still valid. The only difference is the use of a Lorentzian DOS that is indicated by the apex ‘B’. An example representing this phenomenon is shown in fig. 2.1(b). In this case the level spreads outside the BW, therefore the overall current would be less with respect to the discrete case since the contributions coming from the tails are not included in the integration. Another important point is that, in case of broadening, a current flow can appear even if the energy level is outside the BW because there would be some tail states of the Lorentzian inside the window.

Before generalizing this result to the case of multi-level 0D-systems, there are two other phenomena to be analyzed that concern the effects on the energy levels when a bias is applied to the electrodes.

## Fermi level of the dot and charging effect

Up to now only a single energy level has been considered. However a quantum dot is characterized by more than one level and has its own Fermi level that determines the occupation of the states. For example in molecules it is known to be between LUMO and HOMO levels since it determines the last (mostly) occupied orbital (i.e. HOMO). Nevertheless, a question arises in non-equilibrium condition: “how the Fermi level of the dot is influenced by an applied bias  $V_{DS}$ ?”. To answer this question is useful to consider a capacity model as the one in fig. 2.2.

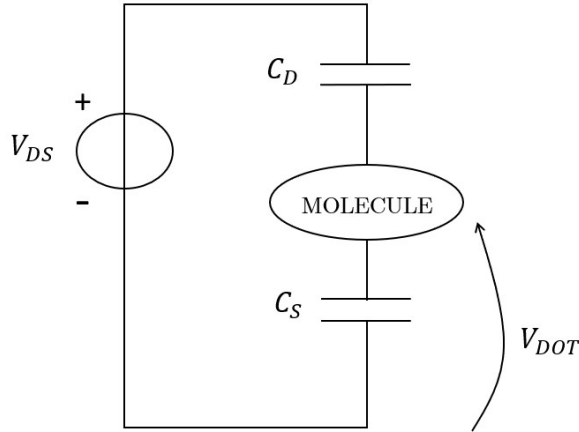


**Figure 2.2:** Capacitive model of a 0D-system.

The two electrodes are modeled with a corresponding capacitance ( $C_S$  and  $C_D$ ) and using simple circuit theory is possible to compute the potential  $V_{DOT}$  dropping on the quantum dot:

$$V_{DOT} = V_{DS} \cdot \frac{C_D}{C_D + C_S} \quad (2.9)$$

Therefore, if we consider source Fermi level as fixed, the drain Fermi level  $E_{F,2}$  will shift in energy by a quantity equal to  $-qV_{DS}$ , while the electrochemical potential of the dot will be shifted down by  $-qV_{DOT}$ . The overall effect is to shift all the energy levels of the dot, thus varying their position in energy which is crucial for conduction. In case of symmetric junctions, where the quality of the two electrodes is the same, the two capacitances are equal  $C_D = C_S$ . Under this condition the potential dropping on the dot is  $V_{DOT} = 1/2 \cdot V_{DS}$ , thus the Fermi level of the dot  $E_{F,DOT}$  takes always the value  $(E_{F,1} - E_{F,2})/2 + E_{F,2}$  that is in the middle of the BW. In this case is possible to see the problem with a different point of view. We can imagine to maintain the levels of the dot at their original equilibrium position and then, when a bias is applied, the source Fermi level is

lift by  $1/2 \cdot V_{DS}$  while the drain Fermi level is lowered by  $-1/2 \cdot V_{DS}$ . The overall result is the same, but the effect of  $V_{DS}$  is taken in consideration when varying the electrochemical potentials of the contacts when a bias is applied. In this special case of symmetric junctions the problem is simplified since it is no more needed to sum an additional potential to the energy levels for considering the effect of bias. In the following this would be the case considered for practical implementation of charge transport.

Another effect, called *charging effect*, is also induced when biasing the junction. Specifically this effect is related to the variation of occupation of the levels when a current flows in the system. At equilibrium each  $i$ -th level hosts  $N_{0,i}$  electrons, while out of equilibrium hosts  $N_i$  electrons evaluated with eq. 2.6. The two values are not equal, thus there is a variation of the total charge inside the dot. Defining as  $N_0$  the total number of electrons in the dot at equilibrium and as  $N$  the number of electrons in non-equilibrium condition, the total charge variation can be simply quantified by the following expression:

$$\Delta Q = -e \sum_{i \in DOT} (N_i - N_{0,i}) = -q(N - N_0) \quad (2.10)$$

The additional charge influences the potential of the dot, therefore is important to study the corresponding contribution. Using again a capacitive model and evaluating the effect of an additional electron w.r.t. equilibrium condition, the potential due to charging effect can be expressed as:

$$U = \frac{e^2}{C_D + C_S} (N - N_0) = U_0 (N - N_0) \quad (2.11)$$

The potential above must be added to the energy levels, which are shifted in energy as consequence. This is important because is at the base of the so-called *Coulomb blockade*. When an energy level enters in the BW, the number of electrons hosted by the level varies. The resulting potential can, for instance, shift up the level delaying its entrance in the BW and so blocking its contribution to conduction. This effect is particularly important in weakly coupled 0D-systems since  $U_0$  is bigger than the thermal ( $k_B T$ ) and broadening ( $\gamma$ ) scale. For strongly coupled systems, such as covalently bonded molecules,  $U_0$  is smaller than the scales just mentioned. However, it is fundamental to consider charging effect in order to have significant results to compare with more sophisticated models. An important problem arises from the evaluation of the total number of electrons. Summing up all the electrons hosted by each level and considering the shift due to charging effect we arrive to this expression:

$$N = \sum_{i \in DOT} \frac{2}{\gamma_{i,1} + \gamma_{i,2}} \int_{-\infty}^{+\infty} DOS_i^B(E - U) [\gamma_{i,1} f_1(E) + \gamma_{i,2} f_2(E)] dE \quad (2.12)$$

The total number of electrons depends on the potential  $U$ , but the latter depends itself on the total number of electrons  $N$ . It is impossible to evaluate analytically an expression for these two quantities and the only possible solution is to find them self-consistently. One can start considering in the first iteration the number of electrons in non-equilibrium condition without considering charging effect and then, in next iterations, evaluate  $U$  and  $N$  using equations 2.11 and 2.12. At each cycle the potential  $U$  can be updated following this procedure:

$$U_{new} = U_{old} + \alpha(U_{calc} - U_{old}) \quad (2.13)$$

$U_{old}$  is the potential used in each iteration to evaluate  $N$  using eq. 2.12 and  $U_{calc}$  is the potential obtained from eq. 2.11 using the updated number of electrons. For the next iteration (for instance  $k + 1$ ) the potential is updated adding a portion of the difference between the potential used in that iteration ( $k$ ) and the potential computed as described above. The parameter  $\alpha$  is in general lower than 1 and can assume values like 0.1-0.5, but in general not smaller than this. The self-consistent procedure is repeated until the potential reaches a value within a certain tolerance. Using the resulting self-consistent potential, renominated  $U_{SCF}$  where SCF stands for Self-Consistent Field, is now possible to evaluate the current. This will be done in the next paragraph summing also all the contributions coming from different levels.

### Independent channels model

As first approximation we can consider the conduction channels identified by the energy levels of the 0D-system as independent. This assumption is of course very coarse but with some necessary changes it can produce good quantitative results. The main consequence of having more levels is that when increasing  $V_{DS}$  the BW becomes larger and can include more than one level (always considering charging effect that delays the entrance in the window). For what concerns equations, the main difference is that now we must sum all the terms relative to different channels. Before obtaining the expression of the current, here below is shown the equation of the total DOS considering the SCF as already computed.

$$\begin{aligned} DOS(E - U_{SCF}) &= \sum_{i \in DOT} DOS_i^B(E - U_{SCF}) \\ &= \sum_{i \in DOT} \frac{\frac{\gamma_i}{2\pi}}{(E - U_{SCF} - E_i)^2 + (\frac{\gamma_i}{2})^2} \end{aligned} \quad (2.14)$$

Using this equation is now possible to rewrite current flow in eq. 2.7 as:

$$I = \frac{2e}{\hbar} \sum_{i \in DOT} \frac{\gamma_{i,1} \cdot \gamma_{i,2}}{\gamma_{i,1} + \gamma_{i,2}} \int_{-\infty}^{+\infty} DOS_i^B(E - U_{SCF}) [f_1(E) - f_2(E)] dE \quad (2.15)$$

Equation 2.15 is the final result to compute the total current flowing through a multilevel quantum dot. Nevertheless this equation is not very familiar for people working in the field of mesoscopic physics. They prefer to introduce the already cited concept of transmission probability of an electron for tunneling from source to drain. In this framework transmission can be introduced by grouping some terms in the above equation:

$$T(E - U_{SCF}) = \sum_{i \in DOT} 2\pi \cdot \frac{\gamma_{i,1} \cdot \gamma_{i,2}}{\gamma_{i,1} + \gamma_{i,2}} DOS_i^B(E - U_{SCF}) \quad (2.16)$$

where  $2\pi$  comes from developing the reduced Planck constant.

Finally with this equation we can write the current in a form that can be seen as an extension of Landauer formula for 0D-systems:

$$I = \frac{2e}{h} \int_{-\infty}^{+\infty} T(E - U_{SCF}) [f_1(E) - f_2(E)] dE \quad (2.17)$$

This is the main result of conduction in 0D-systems adopting the scheme in fig. 2.3 that summarizes what said up to this point. It is worth underline that to compute the  $IV$  characteristic the self-consistent procedure must be repeated for each value of  $V_{ds}$  and then use the SCF in the Landauer formula to obtain the value of current.

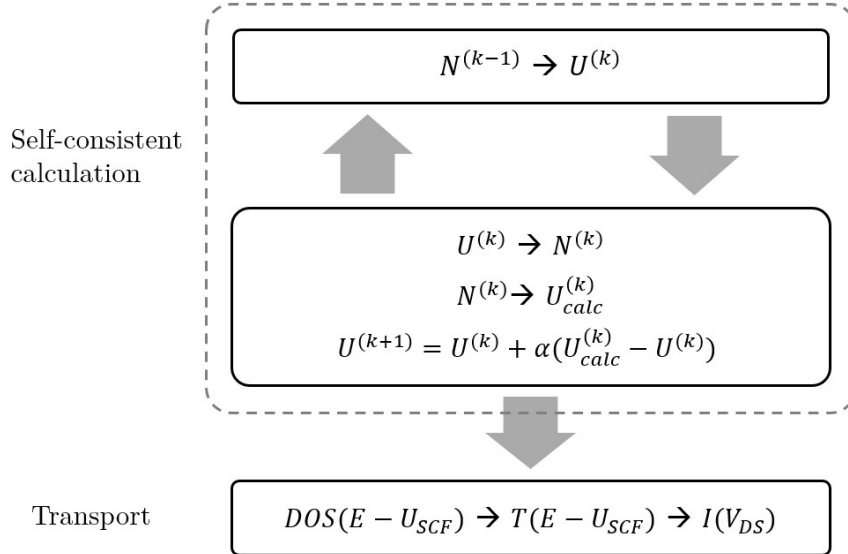


**Figure 2.3:** Scheme summarizing the self-consistent procedure. After convergence is achieved, the SCF is used to compute the DOS, transmission and current.

### Considerations on single-molecule junctions

The independent channels model can be used for a general 0D-system, hence also for single-molecule junctions. The energy levels used in the model are related to the

molecular orbitals and the coupling factors depend on the anchoring groups used to bond the molecule to the electrodes. It is worth notice also that conduction in a real molecular junction is influenced by other factors. The type of molecule is of course important. Conjugated molecules would be more conductive than saturated ones since electrons are bounded to the molecule but with wavefunctions that are spread along the whole system. In turn, conjugation is influenced by torsion angle between adjacent rings with optimal condition when they are in the same plane. Another factor related to the chosen molecule is its length. Longer molecular channels are characterized by lower coupling factors since an electron has a lower probability of being transmitted through the molecule. In addition to this, longer conjugated molecules have smaller HLG and the number of transmission peaks increases.

All these factors, essentially related to the type of considered junction, can be included in the simplified model. However, there are some aspects that go beyond this simplified description. For instance the potential inside the molecule has been described by simply a scalar value but this is of course an approximation. One should solve a Poisson equation in order to obtain a correct potential depending on space variables, that is what *ab-initio* simulators do. Another problem is related to transmission channels. They correspond to different levels but often are superimposed and it is difficult to extrapolate coupling coefficients for all the energy levels. Nevertheless, there is an effect that is crucial and is completely neglected by the described model, which is the polarization of molecular orbitals by an applied bias. When applying a  $V_{DS}$  the molecule feels an electric field that modifies the electronic clouds. They are shifted in space and their shape are deformed. It is almost impossible to understand the effects that a bias would have on transmission since the molecular orbitals can be modified in such a way that the transmission of a certain channel is enhanced whereas the one of another is suppressed. Therefore using the simplified model does not lead to a current comparable to the one computed by other more complex models. But hope is the last to die. Indeed it is possible to modify this simple model to include the effect of polarization. This is done in EE-BESD [41] that is an efficient and effective method for molecular FET modeling developed by A. Zahir *et al.* at Politecnico di Torino. It will be presented in Chap. 3 where I will explain how to modify it to include PAT.

## A bridge towards NEGF

This paragraph has the goal to connect what just described here to a much more complete and rigorous theory that is NEGF. Here I will not give an exhaustive description of the theory, but only essential information needed to make comparisons between the model described in this section and what is the gold standard of quantum transport. NEGF formalism is conceptually different with respect to other

conventional quantum mechanics theory. In general what is usually done is to study the free oscillations of a system under study. In the case of NEGF the perspective is different since this theory aims to study non-equilibrium ‘open’ systems that interact with the environment (an example can be a molecule interacting with the contact reservoirs). The approach of this theory is to study the total response of the system (molecules plus contacts) when an input impulse is considered. The impulse response is represented by the *retarded* Green’s function,  $G^R$ , that is called in this way because there cannot be a response before an impulse is applied. From a mathematical point of view exists also an *advanced* Green’s function,  $G^A$ , which is related to time-reversal symmetry of the system, i.e. when the time variable is rewinded. These functions are defined on two times, one referred to the perturbation ( $t'$ ) and one to the response( $t$ ). However, under steady-state condition, only the time difference  $\tau = t - t'$  is meaningful, therefore is possible to Fourier transforming the Green’s functions in the energy domain, thus simplifying the computation.

$$G^{R,A}(E) = \int_{-\infty}^{+\infty} e^{\frac{i}{\hbar}E\tau} G^{R,A}(\tau) d\tau \quad (2.18)$$

The time dependent functions are then computed with the following equations:

$$G^R(E) = [EI - H - \Sigma^R]^{-1} \quad (2.19)$$

$$G^A(E) = [G^R(E)]^\dagger \quad (2.20)$$

Equation 2.19 is the so called “Dyson’s equation” that is at the basis of the theory. It allows to compute the retarded Green’s function of the total system starting from the Hamiltonian of the active device (a molecule, a nanocrystal, etc.) and including the interaction with the contacts. This is done by defining a retarded contact self-energy  $\Sigma_{1,2}^R$ . Because the two reservoirs are considered at their own equilibrium (established by the external bias) is possible to define a total contact self-energy adding the two contributions:  $\Sigma^R = \Sigma_1^R + \Sigma_2^R$ . Dyson’s equation is an incredible result since allows to treat the interaction of the active system with the reservoirs which could be theoretically of infinite dimensions. The theory models this interaction defining a self-energy that essentially is added to the Hamiltonian. In general it is said that the interaction with the contacts is *folded* inside the Hamiltonian, hence reducing the dimensions of the problem. It is important to underline that Dyson’s equation is not restricted to contact interaction but could be exploited to consider other external influences. For example it is possible to define a ‘phonon’ self-energy that includes in the problem scattering processes between electrons and phonons. On the other hand, when only contact self-energy is considered, the type of transport predicted by the theory is coherent, i.e. elastic with no scattering mechanisms.

Instead, for what concerns the advanced Green’s function, eq. 2.20 relates the two functions showing that  $G^A$  is just the transpose complex conjugate of  $G^R$ .

It is possible to make also other observations on the above equations. The variable  $E$  corresponds to the energy of a ‘test’ electron injected in the device from the contacts, i.e. it corresponds to the input stimulus. In conventional quantum mechanics the energy spectrum of a system is in general the unknown of the problem, instead in NEGF is just a variable characterizing the input stimulus and can be varied as you like. All the above quantities (Hamiltonian, self-energy, Green’s functions) depend on the input energy, thus the solution of Dyson’s equation should be computed for each value of an energy-grid. Inside the equation, the energy variable is multiplied by the identity matrix (in the case of non orthogonal basis set it should be substituted with the overlapping matrix) having dimensions depending on the considered basis set. This means that also all the other quantities between square brackets are matrices, that is not so strange in quantum mechanics. We would have vectors only if the chosen basis set diagonalizes all the quantities, that is almost never the case. In light of this we can say that an inversion of a matrix is involved in the Dyson’s equation. This represents the main drawback of NEGF. The price to pay for an accurate and complete model is to compute a matrix inversion that is computationally very inefficient. To summarize, NEGF simulations are accurate but slow.

In the previous paragraphs a lot of effort was put into explain what is broadening and how it can be considered in the computation of current. But in the framework of NEGF? How does it enter in the theory? As already said contact self energy is the quantity that takes into account what happens at the interface with the reservoirs. For each contact is possible to define a broadening function (matrix) corresponding to the anti-Hermitian part of the contact self-energy:

$$\Gamma_1 = i[\Sigma_1^R - \Sigma_1^A] \quad , \quad \Gamma_2 = i[\Sigma_2^R - \Sigma_2^A] \quad (2.21)$$

$$\Gamma = \Gamma_1 + \Gamma_2 \quad (2.22)$$

where the advanced contact self-energy is defined as  $\Sigma_{1,2}^A = [\Sigma_{1,2}^R]^\dagger$ . Now the problem is to understand why this matrix  $\Gamma_{1,2}$ , depending on energy, is related with broadening. To understand this, a good point is to notice that the eigenvalues of the device are no more related to the only Hamiltonian, but now they can be obtained from  $H + \Sigma^R$ . But this matrix is not Hermitian because  $\Sigma^R$  possesses an anti-Hermitian part, therefore the resulting eigenvalues are complex constituted by a real part  $H + \Re\{\Sigma^R\}$  and an imaginary part  $\Im\{\Sigma^R\}$ . The real part of the energy is renormalized by  $\Re\{\Sigma^R\}$  which is generally small. On the other hand, the imaginary part of energy is the mathematical tool used to describe finite life-time of an eigenstate, that can be seen as the corresponding concept of escape time mentioned above. The finite life-time is directly related to broadening through the uncertainty principle, therefore if there is a link between  $\Gamma$  and  $\Im\{\Sigma^R\}$  we could understand why is called broadening function. Indeed, developing eq. 2.21 we can prove that  $\Gamma = -2\Im\{\Sigma^R\}$ . This confirms its role as direct substitute of

coupling factor  $\gamma$  in NEGF theory, but formally considering the energy dependence of broadening without postulating a Lorentzian shape of the DOS. But why a Lorentzian? We considered a Lorentzian because the DOS assumes that shape when considering a single energy level and neglecting the energy dependence of  $\Sigma^R$ . In this case  $\Gamma = \gamma$  and, extending this assumption for more levels, we obtain the independent channels model described in this section.

In the coherent case, the current computed with NEGF theory assumes an expression identical to Landauer formula of eq. 2.17, without considering the shift due to  $U_{SCF}$  since here all the effects mentioned above are embedded in the theory. What significantly changes is how the transmission probability is computed. Exploiting the above equations, the transmission coefficient is computed in this way:

$$T(E) = \text{Tr}[\Gamma_1 G^R \Gamma_2 G^A] \quad (2.23)$$

The operator ‘Tr’ is the trace operator acting on the matrix inside square brackets. The trace does not change if a different basis set is used and it is also invariant under cyclic permutation of the terms inside the brackets. Equation 2.23 is valid only for coherent transport which is reasonable for molecular junctions considering the nanoscale dimension of molecules.

Generally other two Green’s functions are introduced which are not independent from the ones introduced before. They are called lesser and greater Green’s function and are defined in this way:

$$G^{\lessdot} = G^R \Sigma^{\lessdot} G^A \quad (2.24)$$

$$\Sigma_{1,2}^{\lessdot} = i f_{1,2} \Gamma_{1,2} \quad , \quad \Sigma^{\lessdot} = \Sigma_1^{\lessdot} + \Sigma_2^{\lessdot} \quad (2.25)$$

$$\Sigma_{1,2}^{\gtrdot} = i(f_{1,2} - 1) \Gamma_{1,2} \quad , \quad \Sigma^{\gtrdot} = \Sigma_1^{\gtrdot} + \Sigma_2^{\gtrdot} \quad (2.26)$$

Equation 2.24 is called Keldysh’s equation and allows to compute the lesser ( $G^{\lessdot}$ ) and greater ( $G^{\gtrdot}$ ) Green’s functions starting from the retarded and advanced ones. Moreover the lesser and greater component of contact self-energy are introduced since they enters inside Keldysh’s equation. These components can be computed through the *fluctuations-dissipation theorem* expressed by equations 2.25 and 2.26.

On the contrary to retarded and advanced Green’s functions, which are related to the impulse response of the system, lesser and greater Green’s functions assume different meaning. It is possible to prove that  $-iG^{\lessdot}$  represents the density per unit energy of occupied states, i.e. the electron density per unit energy. This is the reason why  $G^{\lessdot}$  is also called electron correlation function. On the other hand,  $G^{\gtrdot}$  is called hole correlation function and  $iG^{\gtrdot}$  represents the density of empty states per unit energy. Knowing the meaning of these functions is straightforward to compute the spectral function, i.e. the corresponding matrix version of the DOS:

$$A = i(G^{\gtrdot} - G^{\lessdot}) = i(G^R - G^A) \quad (2.27)$$

The spectral function is obtained just by adding the empty states ( $iG^>$ ) with the occupied states ( $-iG^<$ ). Moreover, in steady-state condition only two Green's function are independent and eq. 2.27 expresses also the equivalence between them ( $G^> - G^< = G^R - G^A$ ).

Regarding self-energies, the lesser component  $\Sigma^<$  can be interpreted as the in-scattering of electrons from the contacts to the device. This explains why  $G^<$  is proportional to  $\Sigma^<$  since it has an important role in determining the electron density in the device. Instead,  $\Sigma^>$  is related to the out-scattering of electrons from the device to the contacts and therefore it plays a crucial role in determining the number of empty states represented by  $G^>$ .

Another expression for the current can be obtained using the quantities just introduced. It is a much more general equation that can be used also when scattering mechanisms, for instance phonon or photon scattering, are introduced in the picture.

$$I = \frac{2e}{h} \int_{-\infty}^{+\infty} \text{Tr}[\Sigma_1^<(E)G^>(E) - \Sigma_1^>(E)G^<(E)]dE \quad (2.28)$$

This equation can be interpreted in a simply way.  $\Sigma_1^<G^>$  represents the actual in-scattering from contact 1 to the device: the process is proportional to the number of empty states  $G^>$  and occurs with a rate  $\Sigma_1^<$ . Similarly  $\Sigma_1^>G^<$  is related to the actual out-scattering from the device to contact 1: the process is proportional to the number of occupied states  $G^<$  and occurs with a rate  $\Sigma_1^>$ . The same reasoning can be applied to contact 2 obtaining, in steady-state condition, a current equal in magnitude but with opposite sign.

This concludes the section on conduction of 0D-systems. It is important to have in mind the results commented above because they constitute the base to understand the following models describing PAT, but also because they are the first step towards implementation of photo-assisted transport.

## 2.2 Tien-Gordon model

In 1963 P. K. Tien and J. P. Gordon at the Bell Telephone Laboratories developed a model to explain the experimental results obtained by A. H. Dayem and R. J. Martin studying a superconductor-insulator-superconductor (SIS) junction irradiated by a microwave field. In particular they measured a photocurrent when the junction was irradiated, i.e. there was an additional DC component contributing to the total current. To explain this result, the Tien-Gordon (TG) model is a simple tool, maybe too simple, that already catches the main features of photo-assisted transport. In the last twenty years, it gained a lot of attention from the community of researchers studying illuminated single-molecule junctions since it can give good

qualitative results when it is used in its range of validity. Now the model will be described giving all the information about its assumptions and what they imply. Moreover it will be discussed how it is in general used in the framework of molecular junctions and how it can be compared to other models.

### Assumptions

In TG model the incident electromagnetic field is considered from a classical point of view and the effects of the magnetic field are neglected. The incident radiation is monochromatic and it is simply expressed as  $\vec{E}(\vec{x}, t) = \vec{E}_{AC}(\vec{x}) \cdot \cos(\omega t)$  where  $\vec{E}_{AC}(\vec{x})$  is the amplitude of the incident field having direction determined by the polarization of the field. Considering a laser spot with diameter in the micrometer range, it is much more likely that the electric field interacts with the metallic electrodes than with the molecule. If the incident frequency is below the plasma frequency ( $\omega_p$ ) of the metal and is also lower than the interband transition threshold, the collective screening response of the electrons is effective and most of the light is reflected from the contacts [42], [43]. Nevertheless, if the light polarization is mostly parallel to transport direction, an oscillating potential  $V_{AC}(t)$  will drop between the contacts and the molecule thus inducing a time-dependent current, but also an additional DC component, i.e. the photocurrent, that is modeled by TG. The induced potential is considered *spatially uniform*, i.e. constant, in the electrodes due to the effective screening action below  $\omega_p$ , that is generally in the UV range. On the other hand, the potential inside the junction should be retrieved self-consistently solving Poisson's equation. However this is computationally very intensive and, as it is done in the original article, a vanishing electric field is considered in the gap. Therefore there must be a potential drop at the interface that can follow two conceptual equivalent configurations represented in fig. 2.4: a symmetric one where the total drop  $V_{AC}$  is portioned among the two interfaces and an asymmetric case where the complete drop is just at one interface. Of course this is a dramatic simplification since it is known that in molecular junctions the potential varies depending on how atoms are located in space. On the other hand, if we consider a conjugated molecule, it seems reasonable that the potential drops at the two interfaces due to partial screening of the electric field by the electronic cloud. However the potential along the molecule is likely non-constant, thus this approximation is of course very rough. In addition to this, the symmetric case can be connected to an experimental situation where both contacts are illuminated (that is more likely) whereas in the asymmetric configuration one contact is predominantly illuminated with respect to the other. This point is crucial since is at the core of a non negligible problem of the TG model that will be described in the following.

The exact value of the amplitude  $V_{AC}$  is unknown and depends on various factors such as polarization, radiation frequency, junction geometry, but more importantly

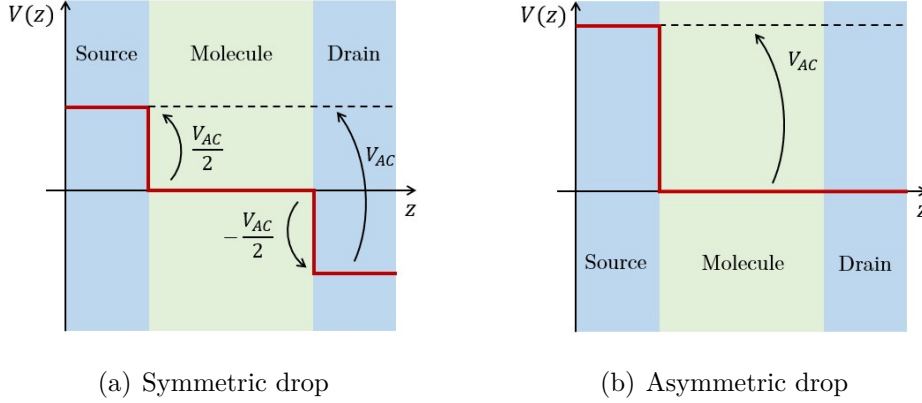


**Figure 2.4:** Representation of the two equivalent configurations of AC voltage drop. In (a) the total drop is partitioned among the two interfaces, therefore is symmetric, while in (b) the drop is just at one interface, thus is asymmetric.

it can be increased by LSP excitation due to related electric field enhancement. For larger values of  $V_{AC}$ , the model loses validity since the precise shape of the induced potential becomes more and more important [44].

The radiation is generally in the microwave range, at most up to frequencies in the visible range below  $\omega_p$ , hence this type of transport is adiabatic (see section 1.3.3) and neglects any intramolecular transitions, even if typically are possible in the optical range. Moreover it also neglects any induced thermal effect, but also any modification in the geometry of the molecule due to the applied field (these last assumptions are valid also for the models in section 2.3 and 2.4).

Here a summary of all the assumptions:

- The electric field is classical:  $\vec{E}(\vec{x}, t) = \vec{E}_{AC}(\vec{x}) \cdot \cos(\omega t)$ .
- When  $\lambda > d_{gap}$ , a spatially uniform oscillating potential  $V_{AC}(t)$  is induced at the contacts and can drop along the junction following a symmetric or asymmetric configuration.
- The radiation frequency must be smaller than the plasma frequency of the metal:  $\omega < \omega_p$  to ensure effective screening. Moreover in this range excitation in the contacts such as phonons or e-h pair generation are neglected.
- The amplitude  $V_{AC}$  is unknown and depend on the specific system under study. It is worth notice that can be generally amplified by LSPs when they are excited, accompanied with a change in the potential shape, which should be computed self-consistently.

- The photo-assisted transport is adiabatic and neglects any intramolecular transitions.
- Light-induced effects are neglected such as thermal effects or modification in the geometry of the molecule.

### Photocurrent

The central idea in TG model is that the induced oscillating potential modulates over time the energy levels of electrons in the contacts while maintaining the same carrier distribution across the levels. This induces a type of transport that is adiabatic since it does not involve resonant transition between molecular energy levels.

It is possible to express the influence on the contacts starting from the Hamiltonian of the system written in second quantization, i.e. the occupation number representation (for a simple but effective introduction see Appendix A in [28]). Without radiation the Hamiltonian can be written as:

$$\hat{H}_0 = \hat{H}_{mol} + \hat{H}_{C1} + \hat{H}_{C2} + \hat{H}_{coupl} \quad (2.29)$$

The first term is the Hamiltonian of the isolated molecule while  $\hat{H}_{C1}$  and  $\hat{H}_{C2}$  correspond to the Hamiltonian of the isolated contact C1 (1 = source) and C2 (2 = drain). Instead the last term represents the charge transfer from the molecule to the electrodes and vice versa, thus it describes the coupling between the molecule and the contacts. Equation 2.29 can be developed using second quantization in this way:

$$\hat{H}_0 = \sum_{i \in mol} E_i \hat{c}_i^\dagger \hat{c}_i + \sum_{k \in C1} E_k \hat{c}_{k,1}^\dagger \hat{c}_{k,1} + \sum_{k \in C2} E_k \hat{c}_{k,2}^\dagger \hat{c}_{k,2} + \sum_{i \in mol} \sum_{k \in \{C1, C2\}} (V_{ki} \hat{c}_k^\dagger \hat{c}_i + H.c.) \quad (2.30)$$

where  $\hat{c}_i$  ( $\hat{c}_i^\dagger$ ) is the fermionic annihilation (creation) operator inside the molecule whereas  $\hat{c}_{k,1}$  ( $\hat{c}_{k,1}^\dagger$ ) is the fermionic annihilation (creation) operator inside contacts C1 and C2.  $E_i$  and  $E_k$  are the energy levels inside the molecule and the contacts while  $V_{ki}$  represents the charge transfer constant coupling a level  $k$  in the electrodes with a level  $i$  inside the molecule. In particular, the expression  $V_{ki} \hat{c}_k^\dagger \hat{c}_i$  means that an electron is created in state  $k$  belonging to one of the two contacts while an electron is annihilated in state  $i$  inside the molecule. Of course also the reverse process could be possible and is represented in the expression by  $H.c.$ , i.e. the Hermitian conjugate of the previous expression.

In the TG model the light irradiating a junction affects only the terms  $\hat{H}_{C1}$  and  $\hat{H}_{C2}$ , therefore the molecular Hamiltonian do not couple with the field and intermolecular transitions cannot be described. An additional oscillating potential appears in the contacts and can be modeled in two ways depending on how the

potential drops at the two interfaces. Dividing the amplitude  $V_{AC}$  in two terms,  $V_{AC,1}$  and  $V_{AC,2}$ , the contact Hamiltonians, that are now time-dependent, can be expressed as:

$$\hat{H}_{C1}(t) = \hat{H}_{C1} + eV_{AC,1} \cdot \cos(\omega t) \quad , \quad \hat{H}_{C2}(t) = \hat{H}_{C2} + eV_{AC,2} \cdot \cos(\omega t) \quad (2.31)$$

For simplicity, for the moment, we restrict the attention only to one (C1) of the two contacts. The additional term in eq. 2.31 does not change the spatial distribution of a wavefunction in contact C1, corresponding to a generic  $k$  state, that can be expressed in the form:

$$\Psi_{k,1}(\vec{x}, t) = f(\vec{x})e^{-i\frac{E_k}{\hbar}t} \quad (2.32)$$

where  $f(\vec{x})$  corresponds to the spatial dependence of the wavefunction. Since the basic assumption in TG is that the external radiation modulates the (quasi-)energy levels of the electrons, one can imagine to substitute  $E_k$  in the above equation with  $E_k + eV_{AC,1} \cdot \cos(\omega t)$ . A general expression of the wavefunction is therefore:

$$\Psi_{k,1}(\vec{x}, t) = f(\vec{x})e^{-\frac{i}{\hbar}\left[E_k t + \int_0^t eV_{AC,1} \cos(\omega t') dt'\right]} \quad (2.33)$$

Expanding the result of the time integral, i.e. a cosine, using Bessel's functions of first kind, we obtain the expression reported in the paper of 1963 by P. K. Tien and J. P. Gordon:

$$\Psi_{k,1}(\vec{x}, t) = f(\vec{x}) \left[ \sum_{n=-\infty}^{n=+\infty} J_n\left(\frac{eV_{AC,1}}{\hbar\omega}\right) e^{-i\frac{E_k + n\hbar\omega}{\hbar}t} \right] \quad (2.34)$$

Generally the argument of the Bessel's functions is defined as  $\alpha_1 = eV_{AC,1}/\hbar\omega$  that is a dimensionless parameter representing the local 'radiation strength' at contact C1. A similar reasoning can be done for contact C2 defining  $\alpha_2$ . In the end what will really count is the difference between the arguments expressed by  $\alpha = \alpha_1 - \alpha_2$ , that is directly related to the total potential drop  $V_{AC}$ . For this reason, considering symmetric drop, we would have  $\alpha_1 = \alpha/2 = eV_{AC}/2\hbar\omega$  and  $\alpha_2 = -\alpha/2 = -eV_{AC}/2\hbar\omega$ , while for the asymmetric case we would have  $\alpha_1 = \alpha = eV_{AC}/\hbar\omega$  and  $\alpha_2 = 0$  or vice versa. This parameter is influenced by the same factors that determine  $V_{AC}$  and in a lot of works is the only parameter defined in the model which can be varied as you like for fitting experimental data.

A question arises looking at eq. 2.34: how do we interpret this wavefunction? J. R. Tucker and M. J. Feldman in 1985 [45] represented graphically (fig. 2.5) the meaning of eq. 2.34. From a point of view of the junction before irradiation, the electrons influenced by an adiabatic driving behave as if having a probability amplitude  $J_n(\alpha)$  to be displaced in energy by  $n\hbar\omega$  i.e. they have a certain probability to exchange  $n$  energy quanta with the oscillating field. Another perspective is to think

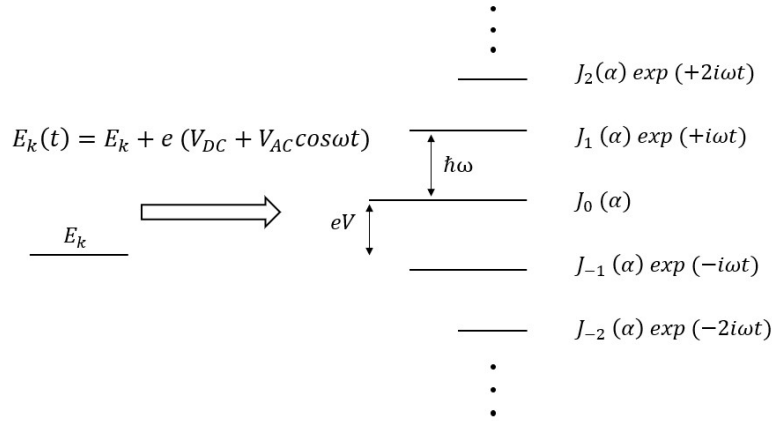


**Figure 2.5:** Graphical interpretation of eq. 2.34 reported in [45] by J. R. Tucker and M. J. Feldman.

that the action of the AC signal is equivalent to the application of voltages  $n\hbar\omega$  with probability  $J_n^2(\alpha)$ .

When index  $n$  is increased, the probability amplitude decreases since related to the order of first kind Bessel’s function. Moreover, increasing the argument  $\alpha$ , Bessel’s functions have an oscillatory decreasing behavior, thus the probability is smaller and smaller as evident from fig. 2.6.

It is also worth underlining that the exchanged energy quanta are not ‘real’ photons from a rigorous point of view since the field is not considered as quantized. Nevertheless in the following I will not make this distinction for simplicity.

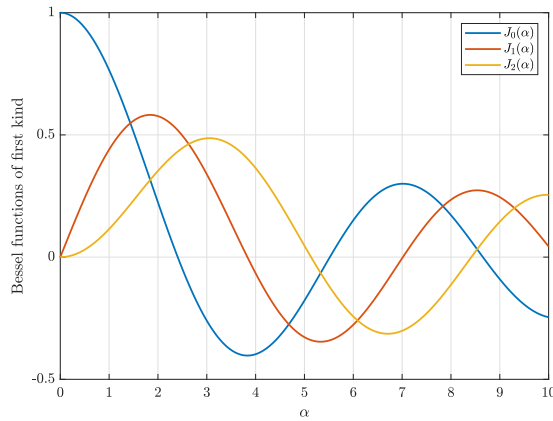


**Figure 2.6:** Bessel’s functions of first kind.

Now we are ready to present the expression of the DC current exploiting the above results. An heuristic derivation will be given, even if a more formal derivation

can be found in [42] where the NEGF formalism is used to obtain a more general expression of DC current when a harmonic perturbation is affecting the system. Assuming that the potential does not spatially vary along the central part of the junction and that the DOS in the contacts is energy independent, the general formula presented in [42] reduces to the result of TG model which will be described here below.

As already said in subsection 1.3.3, when a driving field is acting on a system, transmission probability from left to right and the one from right to left are in general different and should be computed separately. In general the current can be described by a Landauer-like equation:

$$I(V_{DC}; \alpha) = \frac{2e}{\hbar} \sum_{n=-\infty}^{\infty} \int [T_{21}^{(n)}(E)f_1(E) - T_{12}^{(n)}(E)f_2(E)]dE \quad (2.35)$$

To compute the transmission coefficients let us consider the transmission of an electron from left to right electrode. At the left interface an electron can absorb ( $n > 0$ ) or emit ( $n < 0$ ) energy quanta with probability  $J_n(\alpha)^2$ , then they are elastically transmitted through the molecular channel. Similarly, at the other side of the junction they can absorb or emit energy quanta with probability  $J_{l-n}(\alpha)^2$  before crossing the interface and reaching the electrode. At the end the difference between the initial and the final states is of  $l$  quanta. Following this reasoning, the expression for transmission from contact 1 to 2 is:

$$T_{21}^{(l)}(E) = \sum_{n=-\infty}^{\infty} J_{l-n}^2(\alpha_2)T(E + n\hbar\omega)J_n^2(\alpha_1) \quad (2.36)$$

Exploiting the sum rule  $\sum_{l=-\infty}^{\infty} J_l^2(x) = 1$ , we can rewrite the Landauer-like expression as:

$$I(V_{DC}; \alpha) = \frac{2e}{\hbar} \sum_{n=-\infty}^{\infty} \int T(E + n\hbar\omega) [J_n^2(\alpha_1)f_1(E) - J_n^2(\alpha_2)f_2(E)]dE \quad (2.37)$$

This expression is general since considers two different potential drops at the two interfaces. For the symmetric case  $\alpha_{1,2} = \pm\alpha/2$  and eq. 2.37 can be rewritten by factorizing  $J_n^2(\alpha/2)$  since Bessel's functions of first kind are invariant for inversion of sign in the argument:

$$I(V_{DC}; \alpha) = \frac{2e}{\hbar} \sum_{n=-\infty}^{\infty} \int J_n^2\left(\frac{\alpha}{2}\right)T(E + n\hbar\omega) [f_1(E) - f_2(E)]dE \quad (2.38)$$

The above equation can be obtained also for the asymmetric configuration by using  $\alpha$  instead of  $\alpha/2$  inside the squared Bessel's functions (more details below). This equation has a simple interpretation: The molecule supplies the potential landscape

to compute the transmission function and then it is probed at energy  $E + n\hbar\omega$  related to processes involving  $|n|$  photons occurring with probability  $J_n^2(\alpha/2)$ . The current can increase because the absorption or emission of energy quanta can lead electrons to have an energy corresponding to a highly transmissive channel. If their starting energy corresponded to a low transmission coefficient (for example to an off-resonant transport through broadened states), after interacting with photons their transport can change from off-resonant to on-resonant, therefore increasing the overall current. Moreover, is evident that in eq. 2.38 is possible to define a unique transmission spectrum:

$$T_{opt}(E) = \sum_{n=-\infty}^{\infty} J_n^2\left(\frac{\alpha}{2}\right) T(E + n\hbar\omega) \quad (2.39)$$

This spectrum would show additional peaks at energies distant  $n\hbar\omega$  from the main peaks corresponding to the energy levels of the molecule. These new transmission channels are called *sidebands* precisely because they appear at the sides of original transmission peaks.

The main advantage to use this formula for molecular junctions under illumination is that the DC current is fully determined by quantities computed in dark condition, while Bessel's functions weigh different photo-assisted processes, strongly suppressing higher orders of inelastic scattering.

This formula is the main result of TG theory, however it is not generally used in this form since  $V_{AC}$  is unknown. As already said, this voltage can be obtained from experimental data, but only in some specific case. For the sake of clarity I report here the expansion of current around the DC bias truncated at second order:

$$I(V) = I(V_{DC}) + \frac{1}{4} \frac{\partial^2 I}{\partial V^2} \Big|_{V_{DC}} \cdot V_{AC}^2 + \frac{\partial I}{\partial V} \Big|_{V_{DC}} \cdot V_{AC} \cos(\omega t) + \frac{1}{4} \frac{\partial^2 I}{\partial V^2} \Big|_{V_{DC}} \cdot V_{AC}^2 \cos^2(2\omega t) \quad (2.40)$$

This truncation is valid only if  $V_{AC}$  is small and if non-linearities around  $V_{DC}$  are not too large [44]. This last condition is not very typical of molecular junctions due to resonances, i.e. when current increases due to an energy level entering inside the BW. Only for weak bias (small BW) and large HLG this approximation is reasonably good. A type of molecule respecting the constraint on HLG are fully saturated compounds (for example octane).

Within these limits, measuring the characteristic under illumination allows to compute the second derivative of  $I(V)$  at the bias point. From eq. 2.40 is evident that the variation of DC current is expressed by:

$$\Delta I_{DC} = \frac{1}{4} \frac{\partial^2 I}{\partial V^2} \Big|_{V_{DC}} \cdot V_{AC}^2 \quad (2.41)$$

Therefore measuring the variation of current and computing the second derivative allows to obtain  $V_{AC}$ . The obtained value can be used to evaluate a possible

amplification of the field inside the junction by surface plasmons excitation. This procedure is what is done in a number of experimental papers, but not always researchers verify if this approximation is valid or not. Moreover seems almost a contradiction to measure field amplification with a formula obtained by considering a small value of  $V_{AC}$ . Of course you have to be careful before using this approximation.

It is worth notice that developing the TG current in the lowest order of  $V_{AC}$  and, if the conductance varies slowly on a voltage scale of  $\hbar\omega/e$ , we obtain the same variation of DC current expressed in eq. 2.41 (for more details see [20]). This is the reason why eq. 2.41 is frequently reported under the name of ‘TG model’, but, as commented above, is not properly correct in every situation.

### Practical example and critical point of TG model

To understand better what this model implies is crucial to make an example. I will analyze a simple 0D-system depicted in fig. 2.7 that has only two energy levels,  $E_1 = -1$  eV and  $E_2 = 1.5$  eV equivalently coupled to the contacts with  $\gamma = 0.05$  eV. The dark current flowing through the system is computed using the model described in this chapter and corresponds to a value of  $\alpha = 0$ . For simplicity charging effects are not considered, hence is not necessary to compute  $U_{SCF}$ .

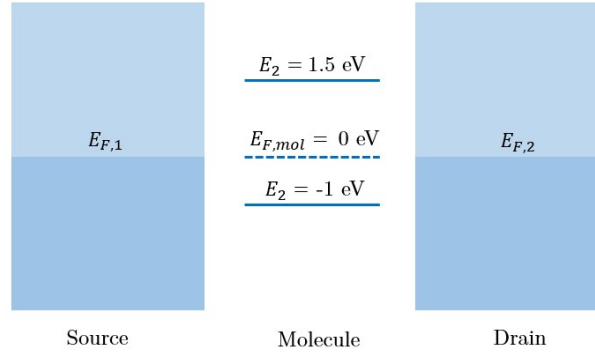


**Figure 2.7:** Example of 0D-system used to show the results of TG model.

If a symmetric drop of  $V_{AC}$  is considered at the two sides of the junction, eq. 2.38 can be directly applied to compute the effects of PAT. It is a ready-to-use expression since it is only required to compute the value of Bessel’s functions and shift the transmission spectrum. The  $IV$  curve under illumination is shown in fig. 2.8(a) where the bias ranges from 0 to 4 V, the considered photon energy is  $\hbar\omega = 0.5$  eV and  $\alpha$  was arbitrary chosen from 0 to 4 since it is just an example.

For value of  $\alpha = 0$ , i.e. no incident radiation, we can observe the dark current. It presents resonances at 2 V and 3 V corresponding to values of bias which allow the entrance of a new level inside the BW. Increasing  $\alpha$ , for low bias the current is

enhanced w.r.t. dark current, while at larger voltages the current is reduced. This behavior is understandable by looking at the transmission spectrum in fig. 2.8(b). The sidebands are visible and the additional peaks correspond to different processes labeled by a certain value of  $n$ . If  $n > 0$  absorption of photons leads electrons inside a main transmission peaks, therefore an additional peak appear at an energy equal to  $E - n\hbar\omega$ . On the other hand, if  $n < 0$  the sidebands correspond to emission of photons that leads electrons inside the main transmission peak. In this figure the integer  $n$  ranges from  $-2$  to  $+2$  because the summations over different orders has been truncated at the second order (positive and negative). It is crucial notice that increasing  $\alpha$ , in the range chosen in this example, the sidebands are enhanced while the ‘dark’ peaks are reduced since the corresponding Bessel’s function,  $J_0$ , decreases with the argument in the range chosen for the example (see fig. 2.6). The overall result is that for low bias additional peaks are inside the BW hence increasing the current with additional resonances, whereas for large bias the current decreases since the height of the main peaks is reduced by the Bessel’s weighting factors.

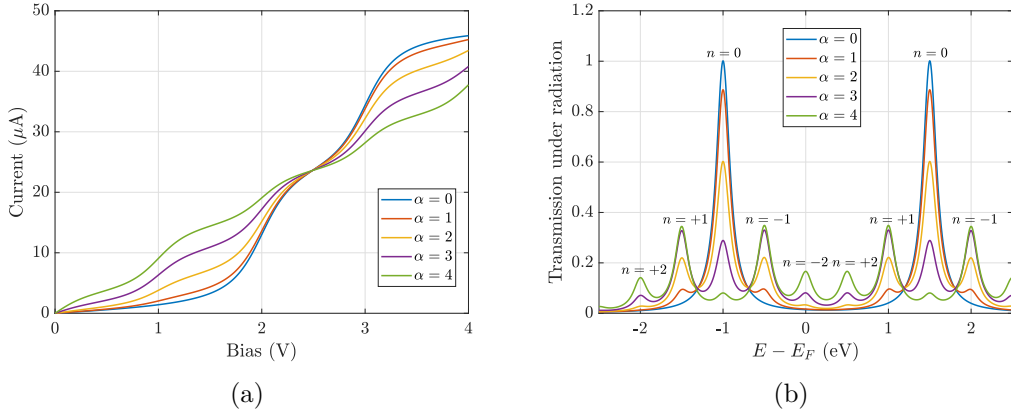


**Figure 2.8:** PAT results using TG model. The left panel (a) shows the  $IV$  curve under illumination of the 0D-system chosen as example, while panel (b) represents how the transmission spectrum is modified by the additional sidebands.

When the power used to illuminate the junction is not so high, it is more likely that occur events involving only the emission or absorption of one photon. In this case  $eV_{AC} \ll \hbar\omega$  and the summation over the Bessel’s orders can be truncated between  $-1$  and  $+1$ . The approximated transmission spectrum is expressed by [21]:

$$T_{opt}(E) \approx T(E) + \frac{1}{4} \frac{\alpha^2}{2} [T(E + \hbar\omega) + T(E - \hbar\omega) - 2T(E)] \quad (2.42)$$

The quality of this approximation can be verified comparing eq. 2.42 with 2.39, whose summation considers orders from  $-5$  to  $+5$ . Using the example above for

$\alpha = 1$ , i.e. a value not so large, the two transmission spectra are computed and shown in fig. 2.9.

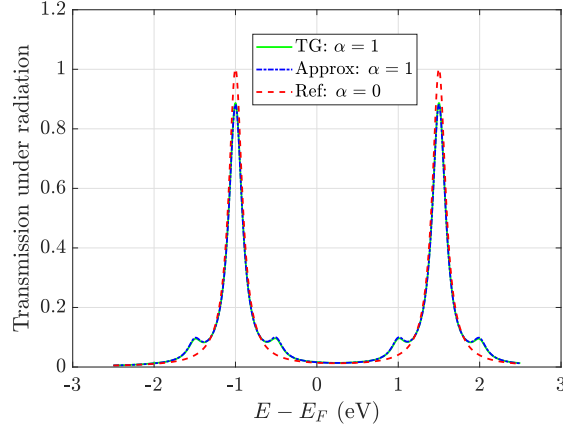


**Figure 2.9:** Comparison between the approximated expression of transmission spectrum under illumination with the one formally obtained in the framework of TG model.

As it can be seen, the spectra are well superimposed and show the same amplitude for the sidebands. Further increasing the value of  $\alpha$  would lead to a completely different result, confirming the validity of the approximated expression only for small oscillating amplitude  $V_{AC}$ .

Another important observation can be done using this simple example. As already mentioned at the end of Chap. 1, in [30] P. Hänggi and coworkers predicted coherent destruction of tunneling (CDT) using a simple tight binding approximation to model a molecular wire in the framework of Floquet theory (see next chapter). Following a similar reasoning is possible to show the same phenomenon with TG model, even if it has not been verified experimentally yet. Thinking about Bessel's weighting factors, a significant reduction of current can occur when the argument  $\alpha/2$  corresponds to a zero of the function  $J_0$ , that is related to transmission peaks in dark conditions. In this case, their contribution to the overall current will vanish, thus reducing its value with respect to the one in dark condition. In fig. 2.10 I compared the  $IV$  curve commented above (represented in panel (a)) with the current computed with  $\alpha = 4.809$  and  $\alpha = 11.040$ , values that if split in half correspond to the first two zeros of  $J_0$ . For the first zero the current is not so different to the one for  $\alpha = 4$ . It is enhanced in the low bias range due to additional sidebands entering inside the BW, while for large bias the current is reduced due to lower contribution coming from main peaks. Nevertheless, for the second zero of  $J_0$  the current is remarkably reduced all over the bias voltages. This is justified by looking at fig. 2.6: Close to the second zero of  $J_0$ , the magnitude of  $J_2$  is also smaller, hence only sidebands of first order contribute to conduction, which is of

course reduced.

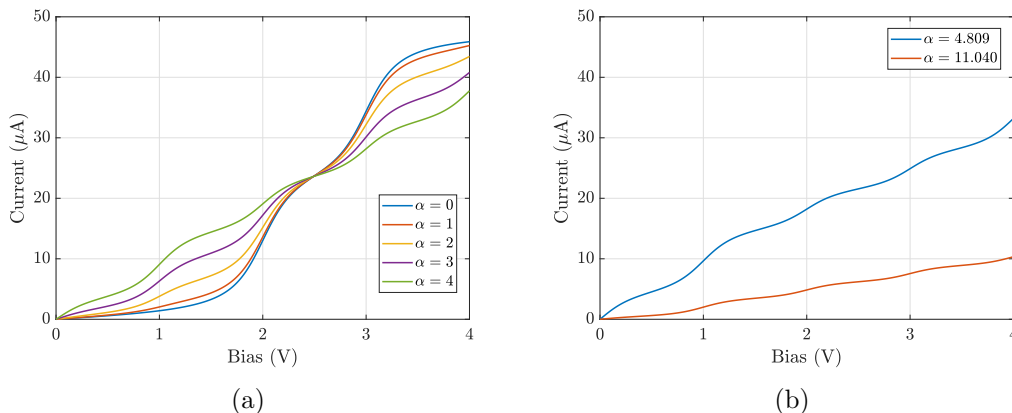


**Figure 2.10:** Theoretical prediction of CDT is shown in panel (b) that depicts the  $IV$  curve for  $\alpha/2$  equal to a zero of Bessel’s function  $J_0$ . In (a) are reported reference  $IV$  characteristics for which  $\alpha/2$  does not correspond to a zero.

Now we are ready to address a critical point of TG model, that will be described exploiting again this example. The plots commented above were computed considering at the two sides of the junction a symmetric drop of the oscillating potential  $V_{AC}$ , as represented in fig. 2.4(a). Nevertheless, shifting by  $V_{AC}/2$  the potential all along the junction, we obtain the asymmetric case depicted in fig. 2.4(b), hence the result should not vary since what changes is just the reference potential. Nevertheless, in this case  $\alpha_1 = eV_{AC}/\hbar\omega$  whereas  $\alpha_2 = 0$ , hence the argument of Bessel’s functions would be  $\alpha$  and no more  $\alpha/2$ . For clarity I reported the expression of current for the asymmetric condition, considering the drop at the left side of the junction:

$$I(V_{DC}; \alpha) = \frac{2e}{\hbar} \sum_{n=-\infty}^{\infty} \int T(E + n\hbar\omega) [J_n^2(\alpha) f_1(E) - f_2(E)] dE \quad (2.43)$$

Computing the  $IV$  characteristics with this equation, for a bias voltage ranging from  $-4\text{ V}$  and  $4\text{ V}$ , we obtain the results shown in fig. 2.11(b). Comparing this case to the symmetric one (reported in fig. 2.11(a)) is obvious that the two configurations predict a different outcome. In particular, the asymmetric configuration shows a photocurrent different from zero even in short-circuit condition when the two Fermi levels of the contacts are identical. This is strange since it means that the electrons, whose energy is adiabatically modulated at one side of the junction, are transmitted through the junction even if no bias is applied. On the other hand, in the symmetric configuration this behavior is not predicted since ideally both sides of the junction are illuminated and opposite fluxes occur leading to a net zero current. This difference between the configurations has been pointed out in 1998

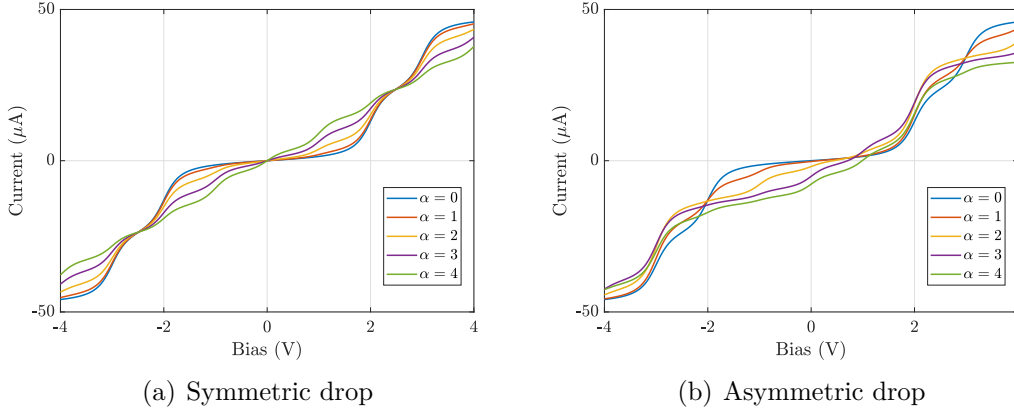


**Figure 2.11:** IV characteristic computed with TG considering a symmetric (a) or asymmetric (b) AC potential drop at the two interfaces. As it is clear, the two results are not equal that means they could correspond to two different physical situations. Nevertheless the system under study is symmetrical and should not develop a net current under short-circuit condition as in (b). For this reason only case (a) will be considered in the following.

by M. H. Pedersen and M. Büttiker [46]. The theory is not *gauge invariant* under an equal shifts of all the potentials, that means the result changes if we change how the AC potential drops along the junction. From a point of view of circuit theory this is of course strange since the result should be the same, while from a ‘mesoscopic’ perspective a different distribution of the potential along the junction could induce a different DC current. However, in the following I will consider as reference the symmetric configuration for this reason: A symmetric system, as the one considered above and the molecular junctions I will consider in Chap. 3, cannot show a net photocurrent in short-circuit condition due to symmetry rules reported in subsection 1.3.3.

M. H. Pedersen and M. Büttiker highlighted also another problem, but related to the symmetric configuration. Because of parity of Bessel’s functions of first kind, if the potential drop is equal at the two sides, both in magnitude and sign, the result does not change. This means that, if  $\alpha_1 = \alpha/2$  and  $\alpha_2 = \alpha/2$ , we obtain again the results shown above. The problem is that if the Fermi levels of the contacts oscillate with the same phase, the difference between them will be always the one imposed by the external DC bias, therefore it should be impossible to develop an additional photocurrent. This issue intrinsically derives from the mathematical formulation of the model and cannot be avoided. In the next sections I will always consider a symmetric drop with opposite phase at the two interfaces.

### Gauge transformation

To conclude this section on TG model and to link it with the next topic, it is worth showing how is possible to modify the problem addressed by TG. As demonstrated in [30] by P. Hänggi and coworkers, the problem of treating oscillating potential applied at the contacts can be gauge transformed in an equivalent problem where the levels of the molecule are oscillating in time. The effect is equivalent to an AC gate voltage uniformly distributed on the channel that varies in time the molecular energy levels. Looking at the Hamiltonian expressed in eq. 2.29, the time dependence was related to additional oscillating potential at the contacts, therefore affecting  $\hat{H}_{C1}$  and  $\hat{H}_{C2}$ . With the gauge transformation the time dependence is transferred to the Hamiltonian of the molecule, but also to the coupling terms that would also depend on time:

$$\hat{H}_{C1}(t), \hat{H}_{C2}(t) \rightarrow \hat{H}_{mol}(t), \hat{H}_{coupl}(t)$$

This transformation is also graphically represented in fig. 2.12 where double-head red arrows are related to the energy oscillation induced by the incident field. Since in the new problem only the molecular Hamiltonian is coupled with the incident radiation, this case can be connected to a different experimental set-up where the field is directed to the molecule by a scanning near-field optical microscope.

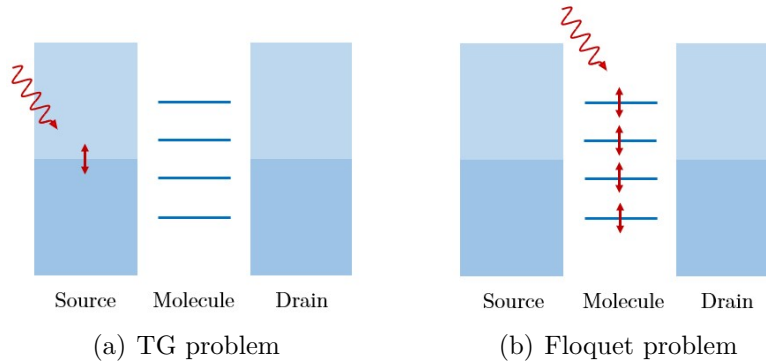


**Figure 2.12:** Graphical representation of gauge transformation from TG case study to typical problem analyzed with Floquet model.

This new point of view is convenient to study direct interaction of light with the molecular system and is at the base of Floquet model. The gauge transformation justifies a possible comparison between TG and Floquet since basically one problem can be transformed to the other. However, this is only true from a mathematical point of view and some doubts are still present concerning what actually happen when light arrives at the junction. It seems more reasonable to think, as said above, that the field interacts predominantly with the contacts when the radiation

frequency is low. Instead, when photon energy is increased up to visible range, the coupling with the molecule could be higher since the energy is comparable to intermolecular transition and LSP can be excited, leading to a strong injection of photons (a.k.a. field amplification) inside the junction.

## 2.3 Floquet model

One of the most studied formalism to analyze PAT in molecular wires is the Floquet model. It is the natural language to deal with periodically driven systems and exploits the Floquet theorem dated back to the original work by Floquet himself in 1883. This theorem was applied later in the context of quantum mechanism when J. Shirley tried to solve the Schrödinger equation for a time-periodic Hamiltonian. Starting from this point, Floquet formalism became an effective tool in physics, used also to understand the behavior of periodic driven many-particle systems like, for example, single-molecule junctions. A first attempt to include Floquet formalism in the study of interaction between light and molecular wires was done by A. Tikhonov [47] in 2002. It was an early work, but already had all the ingredients described later by P. Hänggi and coworkers. Indeed, in 2005 they published an extensive review [30] that describes driven quantum transport, with a particular focus on the analysis of molecular wires exploiting Floquet formalism and NEGF. This section, but especially next chapter, is inspired by this enormous work and also by the high-level work of M. Genske, that in his PhD dissertation analyzed periodically driven many-body quantum systems [48] with a rigorous mathematical approach. It is worth to highlight that Floquet model is the most studied from a theoretical point of view, but it is not applied as much as Tien-Gordon to explain experimental results. The goal of this thesis is also to prove that it can be used in those contexts and can provide information more accurate than Tien-Gordon.

The fundamental assumption needed to apply Floquet formalism is that the Hamiltonian of the system under study is time-periodic. In the context of this thesis, the periodicity is enforced by the incident electromagnetic field that “drives” over time the Hamiltonian of the molecule. Therefore the interaction is just between the electronic structure of the molecule and the radiation field, as depicted in fig. 2.12(b). Recovering the expression of  $\hat{H}_{mol}$  from eq. 2.29, in the driven case it will be time dependent with an additional potential term varying with the same frequency  $\omega$  of the incident field.

$$\hat{H}_{mol}(t) = \hat{H}_{mol,0} + U_{AC}(t) = \sum_{i \in mol} E_i \hat{c}_i^\dagger \hat{c}_i + U_{AC} \cdot \cos(\omega t) \quad (2.44)$$

The second term can be interpreted also in another way. If we introduce the molecular dipole  $\vec{\mu}_{mol}$ , i.e. the dipole moment associated to the molecule, it is

possible to interpret  $U_{AC}(t)$  as the interaction between the dipole and the field. In this dipole approximation we would have:

$$U_{AC}(t) = -\vec{\mu}_{mol}(\vec{x}) \cdot \vec{E}(\vec{x}, t) \quad (2.45)$$

where the maximum values are reached when the polarization of the field is parallel to the molecular dipole. In order to be more general, in this section I will consider  $U_{AC}(t) = U_{AC} \cdot \cos(\omega t)$  instead of this more physical interpretation, that would be commented more in detail in Chap. 3.

Looking at eq.2.44 and defining the period of the field as  $\mathcal{T} = 2\pi/\omega$ , we can state that  $\hat{H}_{mol}(t + \mathcal{T}) = \hat{H}_{mol}(t)$ . It is possible to demonstrate that this dependence is inherited also by the Green's function of the system. An intuitive way to understand this statement is to think about eq.2.19. The equation could be solved at each time instant where only the Hamiltonian of the molecule is varying (for simplicity the time dependence of the coupling term is neglected). Fixing a time  $t_0$ , the solution for  $G_R$  would be the same at the instants proportional to a multiple of the period, that are  $t_0 + n\mathcal{T}$  where  $n$  is an integer. This is true because the Hamiltonian would be the same for these time values, hence the matrix inversion would give the same result. This is crucial when exploiting Floquet in the framework of NEGF since allows to decompose the Green's functions in many modes corresponding to different transport mechanisms. Before showing how it can be done, it is crucial to underline that, when a general time dependence is considered, the Green's functions can no more be Fourier transformed directly from the time domain to the energy domain. However, it is still possible when the Green's functions are time-periodic, but an additional step is needed. This is the main advantage of Floquet theorem, otherwise we would be forced to deal with a time variable that requires more complex computational schemes. Even with a general time dependence, a Fourier transform can be done with respect to one of the time variables that define the Green's function. Considering  $G^R$ , the *one-sided* Fourier transform is [49]:

$$G^R(t, E) = \int_{-\infty}^{+\infty} e^{\frac{i}{\hbar}E(t-t')} G^R(t, t') dt' \quad (2.46)$$

It is evident that the time dependence is still inside the Green's function. However, as said above,  $G^R(t, E)$  has the same periodicity of  $\hat{H}_{mol}(t)$ , hence it can be expanded using a Fourier series in order to rule out the time dependence from  $G^R$ . The Fourier components of the retarded Green's function, also called Floquet modes, will be formally expressed as [30]:

$$G^{R(n)}(E) = \frac{1}{\mathcal{T}} \int_0^{\mathcal{T}} e^{-in\omega t} G^R(t, E) dt \quad (2.47)$$

The energy is the only variable that defines  $G^{R(n)}$ , hence the time dependent problem could be solved adopting a time-independent procedure confirming again

the advantage of using Floquet. In many papers these two steps are generally implicit and the two-times Green's functions are defined directly using the Fourier components expressed in eq. 2.47. For example  $G^R(t, t')$  can be written in this way [50]:

$$G^R(t, t') = \sum_{n=-\infty}^{\infty} \int \frac{dE}{2\pi} G^{R(n)}(E) e^{-\frac{i}{\hbar}E(t-t') + in\omega t} \quad (2.48)$$

The total current can be evaluated starting from the Floquet modes, but the problem is how to compute them. There are two approaches that will be described here below. The first one is based on the practical application of the Floquet theorem. Instead the second is based on the solution of a Floquet-Dyson equation obtained exploiting the time periodicity of the Hamiltonian.

### Floquet theorem

When considering open systems, the effects of the contacts can be folded inside an effective Hamiltonian by means of a contact self-energy  $\Sigma$ . In order to make things simple, to present the Floquet theorem I will consider the Wide Band Limit (WBL) that implies contact self-energies that are independent from energy. Moreover, also the renormalization due to the real part of  $\Sigma$  is neglected, therefore it can be expressed by  $\Sigma_{\alpha}^{R,A} = \mp i\Gamma_{\alpha}/2$  where  $\Gamma_{\alpha}$  is referred to C1 or C2 and does not depend on time and energy. Under this approximation, the term  $\hat{H}_{mol}(t) - i\Gamma/2$  would be time-periodic because folding the effects of the reservoirs inside an effective Hamiltonian means just adding a constant term. As a consequence we can exploit time periodicity to solve the single-particle Schrödinger-like equation that governs the dynamics of the driven system.

$$i\hbar \frac{\partial}{\partial t} |\psi(t)\rangle = \left( \hat{H}_{mol}(t) - i\frac{\Gamma}{2} \right) |\psi(t)\rangle = \hat{H}_{eff}(t) |\psi(t)\rangle \quad (2.49)$$

Note that in this section I will use Dirac's formalism to indicate a particle state. For this reason, the formalism is briefly reviewed in Appendix A. As just mentioned, in the Schrödinger-like equation I have defined an effective Hamiltonian  $\hat{H}_{eff}(t)$  that includes the contribution of the contacts. It is known that the formal solution of the Schrödinger equation is:

$$|\psi(t)\rangle = e^{-\frac{i}{\hbar} \int_{t_0}^t \hat{H}(t') dt'} |\psi(t_0)\rangle = S(t, t_0) |\psi(t_0)\rangle \quad (2.50)$$

The evolution operator  $S(t, t_0)$  expresses the evolution from state  $|\psi(t_0)\rangle$  to state  $|\psi(t)\rangle$ . When the Hamiltonian is Hermitian, the evolution operator is unitary that means inner products are preserved in Hilbert space. However, the effective Hamiltonian in eq. 2.49 is not Hermitian due to the inclusion of contacts self-energy. As a consequence, the evolution operator  $S(t, t_0)$  would be no more unitary.

Moreover, the time dependence rules out the standard variables separation ansatz for which the evolution is expressed by  $S(t, t_0) = \exp[iE(t - t_0)/\hbar]$  (valid in steady-state condition). Nevertheless, eq. 2.49 can be solved by invoking Floquet theorem which states that for a time-periodic Hamiltonian  $\hat{H}(t) = \hat{H}(t + \mathcal{T})$  there exists a complete set  $\{|\psi_\alpha(t)\rangle\}$  of solutions which is of the form [30]:

$$|\psi_\alpha(t)\rangle = e^{-\left(\frac{i}{\hbar}E_\alpha + \gamma_\alpha\right)t} |u_\alpha(t)\rangle \quad (2.51)$$

$$|u_\alpha(t)\rangle = |u_\alpha(t + \mathcal{T})\rangle \quad (2.52)$$

The solution to the Schrödinger-like equation with a time-periodic Hamiltonian can be written as a product of a plane wave, characterized by a complex quasienergy  $E_\alpha - i\hbar\gamma_\alpha$ , and a time-periodic function that is called “Floquet state”. Curiously, this solution is very much similar to the one for spatially periodic systems when Bloch’s theorem is used. Substituting this functional form of the solution inside eq. 2.49 we obtain an eigenvalue equation of this type:

$$\underbrace{\left(\hat{H}_{mol}(t) - i\frac{\Gamma}{2} - i\hbar\frac{\partial}{\partial t}\right)}_{\hat{H}^F(t)} |u_\alpha(t)\rangle = (E_\alpha - i\hbar\gamma_\alpha) |u_\alpha(t)\rangle \quad (2.53)$$

This equation is called “Floquet equation” whereas  $\hat{H}^F$  is the Floquet Hamiltonian. The advantage to have an equation like this is that, despite of having a time dependent Hamiltonian, it is enough to solve an eigenvalue problem, typical of a time-independent Hamiltonian, in order to acquire all the information about the system [48]. The problem is that Floquet states depend on time, hence the eigenvalue problem should be solved for times in the first period ( $t \in [0, \mathcal{T})$ ). Looking better at the problem, we can realize that there is a certain redundancy inside Floquet states. Indeed, given a state  $|u_\alpha(t)\rangle$  with corresponding eigenvalue  $E_\alpha - i\hbar\gamma_\alpha$ , it is possible to find another Floquet state which produces the same physical eigenstate  $|\psi_\alpha(t)\rangle$ :

$$|u_{\alpha'}(t)\rangle = e^{i\omega t} |u_\alpha(t)\rangle \quad (2.54)$$

The corresponding eigenvalue of this equivalent state would have a real part equal to  $E_{\alpha'} = E_\alpha + n\hbar\omega = E_{\alpha,n}$  with  $n \in \mathbb{Z}$ . Thus, to each eigenstate labeled by  $\alpha$ , there is a class of solutions that are just replicas of the same Floquet state. A consequence of this is that the quasienergy spectrum is periodic with a periodicity  $\hbar\omega$ . Thanks to this redundancy, we can reformulate the eigenvalue problem considering that the quasienergies  $E_\alpha$  are restricted in an interval called first Floquet zone (1FZ) defined as:

$$-\frac{\hbar\omega}{2} \leq E_\alpha < \frac{\hbar\omega}{2} \quad (2.55)$$

Knowing the quasienergies inside the 1FZ allows to know all the others quasienergies outside this interval thanks to the replicas shifted by  $n\hbar\omega$ . This of course simplifies the problem since it reduces the dimensions of the set of solutions. It remains the problem of time dependence inside the Floquet equation which can be addressed by exploiting again time periodicity of Floquet states. Indeed they can be expanded through a Fourier series:

$$|u_\alpha(t)\rangle = \sum_n e^{-in\omega t} |u_\alpha^n\rangle \quad (2.56)$$

The Fourier modes of a Floquet state are indicated by  $|u_\alpha^n\rangle$  whereas  $e^{-in\omega t}$  are the Fourier basis functions identified by the set  $\{|n\rangle\}$ . It is worth making a digression about the mathematical structure which Floquet states belong to. Fourier functions form a complete orthonormal set in the vector space  $\mathbb{T}$  of  $\mathcal{T}$ -periodic functions. Knowing this, we can observe that Floquet states  $|u_\alpha(t)\rangle$  are defined on a composite vector space  $\mathbb{F} = \mathbb{H} \otimes \mathbb{T}$  where  $\mathbb{H}$  is the Hilbert space spanned by some basis  $\{|\beta\rangle\}$ , while  $\mathbb{T}$  is the space defined above. The composite vector space is referred in literature as extended Hilbert space, Sambe space or Floquet space. Having this in mind, it is possible to express a Floquet state as:

$$|u_\alpha\rangle\rangle = (\dots, |u_\alpha^{-1}\rangle, |u_\alpha^0\rangle, |u_\alpha^1\rangle, \dots)^T \quad (2.57)$$

The ‘double ket’ notation is used instead of specifying the time dependence, that has been directly absorbed in the structure of Floquet space. It is clear how the Floquet mode can be represented as a vector of Fourier modes, each of them defined on  $\mathbb{H}$ . Instead, if explicit time dependence is required, is sufficient to evaluate eq. 2.56 in order to obtain  $|u_\alpha(t)\rangle$ .

The double ket notation is also convenient to express the scalar product between two vectors in  $\mathbb{F}$ :

$$\langle\langle\psi|\phi\rangle\rangle = \frac{1}{\mathcal{T}} \int_0^{\mathcal{T}} \langle\psi(t)|\phi(t)\rangle dt \quad (2.58)$$

The inner couple of bra-ket represents the scalar product in  $\mathbb{H}$  whereas the external couple corresponds to a time averaging over a single driving period, i.e. the scalar product in  $\mathbb{T}$ .

Another important observation is that  $|u_\alpha(t)\rangle$  cannot be taken as basis vectors of space  $\mathbb{T}$  since they are not mutually orthogonal due to the non-Hermiticity of the Floquet Hamiltonian. Therefore in this case is much more convenient working with the Fourier basis set.

Finally, Fourier decomposition can be exploited to convert Floquet equation in a matrix version that is more manageable from a computational point of view. The first step is to rewrite Floquet states using eq. 2.56:

$$\hat{H}_F(t) \sum_n e^{-in\omega t} |u_\alpha^n\rangle = (E_\alpha - i\hbar\gamma_\alpha) \sum_n e^{-in\omega t} |u_\alpha^n\rangle \quad (2.59)$$

Then, we can left-multiply by  $\langle m| = e^{im\omega t}$  and time averaging over the first period:

$$\sum_n \frac{1}{T} \int_0^T \underbrace{e^{im\omega t} \hat{H}^F(t) e^{-in\omega t} dt}_{H_{mn}^F} |u_\alpha^n\rangle = (E_\alpha - i\hbar\gamma_\alpha) \sum_n \frac{1}{T} \int_0^T \underbrace{e^{im\omega t} e^{-in\omega t} dt}_{\delta_{m,n}} |u_\alpha^n\rangle \quad (2.60)$$

$$\sum_n H_{mn}^F |u_\alpha^n\rangle = (E_\alpha - i\hbar\gamma_\alpha) |u_\alpha^m\rangle \quad (2.61)$$

The first underbrace in eq. 2.60 defines the matrix elements of Floquet Hamiltonian computed with Fourier basis functions, while the second underbrace simply shows that the inner product between two different Fourier exponential is equal to a Kronecker delta function. The action of the delta is to remove the summation over  $n$  and change the index of the Fourier mode from  $n$  to  $m$ . Equation 2.61 simply shows the previous equation rewritten with the matrix formalism. This expression can be generalized considering a vector of Fourier modes, i.e. a vector  $|u_\alpha\rangle \in \mathbb{F}$  that is multiplied by the matrix  $\tilde{H}^F$  that contains all the elements  $H_{mn}^F$ .

$$\tilde{H}^F |u_\alpha\rangle = (E_\alpha - i\hbar\gamma_\alpha) |u_\alpha\rangle \quad (2.62)$$

It is clear that this eigenvalue equation can be treated as a time-independent problem since the time dependence is intrinsically present on the definition of state vectors  $|u_\alpha\rangle$ . The main problem is therefore the diagonalization of matrix  $\tilde{H}^F$ . The goal of all this derivation is to obtain the eigenstates in order to compute the Floquet modes of the Green's function, in turn used to compute the total current. This is done exploiting the spectral decomposition of Green's functions. However, it is feasible only if the eigenstates form a complete and orthonormal basis. As mentioned above, this is not the case for  $|u_\alpha(t)\rangle$  because the Floquet Hamiltonian is not Hermitian. Nevertheless, solving also the adjoint equation

$$[\tilde{H}^F]^\dagger |u_\alpha^\dagger\rangle = (E_\alpha + i\hbar\gamma_\alpha) |u_\alpha^\dagger\rangle \quad (2.63)$$

is possible to define at equal times a bi-orthogonal basis that respects the orthonormal and completeness condition:

$$\langle u_\alpha^\dagger(t) | u_\beta(t) \rangle = \delta_{\alpha,\beta} \quad (2.64)$$

$$\sum_\alpha |u_\alpha(t)\rangle \langle u_\alpha^\dagger(t)| = 1 \quad (2.65)$$

Eventually, the Floquet modes of the retarded Green's function is obtained from a spectral decomposition that is done exploiting this basis [30]:

$$G^{R(n)}(E) = \sum_{\alpha,n'} \frac{|u_\alpha^{n'+n}\rangle \langle u_\alpha^{n'\dagger}|}{E - (E_\alpha + n'\hbar\omega - i\hbar\gamma_\alpha)} \quad (2.66)$$

Summarizing, the first step of the procedure is to solve the (adjoint) Floquet equation in order to find the (adjoint) Floquet modes that are later used to compute the Floquet modes of the retarded Green's function.

Even if this procedure is well established, since there are several papers where it is described into detail and implemented ([51], [52], [53]), less information is available on the computational schemes needed to diagonalized the Floquet Hamiltonian. Moreover I have found much more practical the other approach to compute  $G^{R(n)}$ , that is not simpler to understand or implement, but it is well described in literature [54], [55].

### Floquet-Dyson equation

The second method that can be adopted to compute the Floquet modes of the Green's functions is based on the direct inclusion of time periodicity inside the NEGF framework. The following discussion is taken from a paper [55] signed by G. Stefanucci who is an italian professor working at the University of Rome Tor Vergata.

First of all, the time-periodic perturbation  $U_{AC}(t)$  can be decomposed into a Fourier series where only two terms corresponding to orders  $m = \pm 1$  are different from zero when considering a monochromatic incident radiation (that is the case analyzed in this thesis).

$$U_{AC}(t) = \sum_m U_m e^{im\omega t} = U_+ e^{i\omega t} + U_- e^{-i\omega t} \quad (2.67)$$

When considering a cosinusoidal perturbation the Fourier amplitudes are  $U_+ = U_{AC}/2$  and  $U_- = U_{AC}/2$ , whereas for the sinusoidal case  $U_+ = U_{AC}/2i$  and  $U_- = -U_{AC}/2i$ . For these cases the time-averaged current computed with the Green's function is the same because the difference between sine and cosine is just a phase shift. From now on I will generally consider the amplitudes  $U_{\pm}$ .

The Green's function of the molecular channel in the absence of radiation is defined by  $g(t, t')$ . In this condition the retarded Green's function depends only on time difference  $\tau = t - t'$ . Nevertheless, is always possible to apply eq. 2.48 to expand  $g^R(t, t')$ :

$$g^R(t, t') = \sum_{n=-\infty}^{\infty} \int \frac{dE}{2\pi} g^{R(n)}(E) e^{-\frac{i}{\hbar}E(t-t') + in\omega t} \quad (2.68)$$

In the absence of external perturbation, the Floquet modes  $g^{R(n)}$  are equal to zero except for  $g^{R(0)}$  that is computed with the Dyson's equation for steady-state condition:

$$g^{R(0)}(E) = [EI - H_{mol,0} - \Sigma^R]^{-1} = \frac{I}{EI - H_{mol,0} - \Sigma^R} \quad (2.69)$$

In eq. 2.69 a fractional notation is used to express the matrix inversion, reminding that  $I$  corresponds to the identity matrix and  $\Sigma^R$  is referred to the total contact self-energy.

When the perturbation is switched on, it is possible to write a Dyson's equation in order to include inside the Green's functions the effects of the interaction with the field (for more information about NEGF see section 2.4). Therefore to obtain the interacting Green's function we need to solve the following “Floquet-Dyson equation” where the perturbation induced by an incident monochromatic field is time-periodic.

$$G^R(t, t') = g^R(t, t') + \int g^R(t, \bar{t}) U_{AC}(\bar{t}) G^R(\bar{t}, t') d\bar{t} \quad (2.70)$$

It is more convenient to rewrite this equation in terms of Floquet modes. Substituting eq. 2.67 and 2.68 inside the Floquet-Dyson equation we obtain the following expression, that is easier to address with a computational scheme:

$$G_n(E) = \delta_{n,0} g_n(E) + g_n(E) \sum_m U_m G_{n-m}(E) \quad (2.71)$$

I must underline that  $g_n$  is not a Floquet mode of  $g$  since the latter refers to the non-interacting system. Indeed,  $g_n$  is just a short-hand notation corresponding to  $g_n(E) = g^{R(0)}(E - n\hbar\omega)$ . Also  $G_n$  is a notation used to indicate the  $n$ -th Floquet mode sampled at energy  $E - n\hbar\omega$ , i.e.  $G_n(E) = G^{R(n)}(E - n\hbar\omega)$ . Instead  $\delta_{n,0}$  is the Kronecker delta that adds the term  $g_n(E)$  to the equation only when  $n = 0$ . Equation 2.71 is valid for any time-periodic perturbation. Restricting the focus on the monochromatic case, the summation runs only on two terms corresponding to  $m = \pm 1$ , i.e. the Fourier amplitudes  $U_{\pm}$ . Therefore, the Floquet-Dyson equation becomes:

$$G_n(E) = g_n(E) \left[ \delta_{n,0} + U_+ G_{n-1}(E) + U_- G_{n+1}(E) \right] \quad (2.72)$$

It is clear that this equation relates different Floquet modes whose index difference is equal to one. It is useful to rewrite the expression above in a slightly different way:

$$-g_n U_+ G_{n-1} + G_n - g_n U_- G_{n+1} = g_n \delta_{n,0} \quad (2.73)$$

From this expression it is clear that the Floquet-Dyson equation corresponds to a tridiagonal matrix whose entries are the terms in the left hand side, whereas the known vector is the right hand side term. The unknown of the system is the vector of Floquet modes  $G_n$ . To clarify this concept, I have reported here below the expression of the matrix storing the coefficients coming from the left hand side.



are defined. First of all the matrix block  $[0]$  corresponds to a matrix where all the entries are zeros. Instead  $M_+$  and  $M_-$  correspond to the bottom-right and top-left block respectively. These block matrices stores all the terms that multiplies the Floquet modes. In particular, terms belonging to  $M_+$  multiply the Floquet modes with index  $n > 0$ , whereas terms in  $M_-$  multiply only Floquet modes with index  $n < 0$ . Considering for the moment only the Floquet modes with  $n > 0$ , we can write down a matrix sub-system where  $M_+$  multiplies the vector  $G_+$  that contains the considered Floquet modes.

$$\begin{bmatrix} I & -g_1U_- & 0 & 0 & \cdots \\ -g_2U_+ & I & -g_2U_- & 0 & \cdots \\ 0 & -g_3U_+ & I & -g_3U_- & \ddots \\ 0 & 0 & \ddots & \ddots & \ddots \end{bmatrix} \begin{bmatrix} G_1 \\ G_2 \\ G_3 \\ \vdots \end{bmatrix} = \begin{bmatrix} g_1U_+G_0 \\ 0 \\ 0 \\ \vdots \end{bmatrix} \quad (2.76)$$

The known vector in the above matrix sub-system is obtained by considering that the only term outside  $M_+$  used to determine  $G_+$  is  $-g_1U_+$ , that is inside the central column highlighted in eq. 2.75. This term multiplies  $G_0$  and is added to the others in order to obtain a zero, in the known vector, corresponding to index  $n = 1$ . In eq. 2.76 we consider only the terms inside  $M_+$ , therefore the entries of the known vector, indicated by  $b$ , would be all zeros expect for the first term corresponding to  $n = 1$ . This entry would be equal to  $g_1U_+G_0$ , i.e. the opposite of the missing term that is taken into account by the total matrix system. Inverting the matrix above, we can express the vector of positive Floquet modes by a simple matrix multiplication between the inverted matrix, indicated by  $C_+$ , and the known vector.

$$M_+G_+ = b \quad \Rightarrow \quad G_+ = [M_+]^{-1}b = C_+b \quad (2.77)$$

Writing down explicitly the component of  $C_+$  is possible to obtain a formal expression for  $G_+$ .

$$\begin{bmatrix} C_{+,11} & C_{+,12} & C_{+,13} & C_{+,14} & \cdots \\ C_{+,21} & C_{+,22} & C_{+,23} & C_{+,24} & \cdots \\ C_{+,31} & C_{+,32} & C_{+,33} & C_{+,34} & \cdots \\ \vdots & \vdots & \vdots & \vdots & \ddots \end{bmatrix} \begin{bmatrix} g_1U_+G_0 \\ 0 \\ 0 \\ \vdots \end{bmatrix} = \begin{bmatrix} C_{+,11}g_1U_+G_0 \\ C_{+,21}g_1U_+G_0 \\ C_{+,31}g_1U_+G_0 \\ \vdots \end{bmatrix} \quad (2.78)$$

The main problem of the expression above is that computing an inversion of a matrix is never a good idea in terms of computational effort. However, the recursive scheme developed by Martinez allows to obtain all the Floquet modes starting from one of the coefficient inside  $C_+$ . Similarly to what is done in [55], I will indicate the top-left entry of  $C_+$  as  $M_+^{-1} = C_{+,11}$ . The reasoning followed up to now can be generalized for negative Floquet modes, therefore I will indicate with  $M_-^{-1}$  the

bottom-right entry of  $[M_-]^{-1}$ . With this notation and looking at eq. 2.78 we can express the Floquet modes corresponding to  $n = \pm 1$  as:

$$G_{\pm 1} = M_{\pm}^{-1} g_{\pm 1} U_{\pm} G_0 \quad (2.79)$$

Since positive and negative modes can be computed in a similar way, starting from this point I will indicate with the index  $n$  the absolute value of the mode, i.e.  $n \leftarrow |n|$ . The above result can be inserted inside eq. 2.72, considering  $n = 0$ , in order to obtain an expression for  $G_0$ :

$$G_0 = g_0 + g_0 \sum_{\pm} U_{\mp} M_{\pm}^{-1} g_{\pm 1} U_{\pm} G_0 \quad (2.80)$$

This equation is a key result for the recursive procedure since from the zero-th order it can be possible to obtain all the other Floquet modes. Before describing how we can do this, it can be demonstrated that, starting from  $M_{\pm}$ , the terms  $M_{\pm}^{-1}$  can be expressed as a matrix continued fraction:

$$M_{\pm}^{-1} = \frac{I}{I - g_{\pm 1} U_{\mp} \frac{I}{I - g_{\pm 2} U_{\mp} \frac{I}{I - g_{\pm 3} U_{\mp} \dots}} g_{\pm 2} U_{\pm}} \quad (2.81)$$

$$= \frac{I}{g_{\pm 1}^{-1} - U_{\mp} \frac{I}{g_{\pm 2}^{-1} - U_{\mp} \frac{I}{\dots}} U_{\pm}} g_{\pm 1}^{-1} \quad (2.82)$$

Looking at the above equation, we can say that  $M_{\pm}^{-1}$  is obtained by the multiplication between a continued matrix fraction and  $g_{\pm 1}^{-1}$ . The continued fraction in eq. 2.82 can be rewritten with a recursive relation, therefore  $M_{\pm}^{-1}$  can be rewritten as:

$$M_{\pm}^{-1}(E) = H_{\pm 1}^{-1}(E) g_{\pm 1}^{-1}(E) \quad (2.83)$$

where  $H_{\pm 1}^{-1}$  corresponds to the ‘external’ fraction written in 2.82. This term is obtained with a recursive scheme, starting from the maximum order  $n = n_{max}$  and backwards computing all the others until  $n = 1$ . Consecutive  $H_{\pm n}^{-1}$  are linked by the following recursive relation:

$$H_{\pm n}^{-1}(E) = \frac{I}{g_{\pm n}(E) - U_{\mp} H_{\pm(n+1)}^{-1}(E) U_{\pm}} \quad (2.84)$$

$$= \frac{I}{(E \mp n \hbar \omega) I - H_{mol,0} - \Sigma^R(E \mp n \hbar \omega) - U_{\mp} H_{\pm(n+1)}^{-1}(E) U_{\pm}} \quad (2.85)$$

It is evident that matrix inversions are involved to compute  $H_{\pm n}^{-1}$ , but the dimensions of the involved matrices are of course smaller than the ones of  $C_{\pm}$ .

Now is possible to substitute eq. 2.83 inside 2.80 and define an AC self-energy that takes into account the effects of the perturbation:

$$\Sigma_{AC}^R(E) = \sum_{\pm} U_{\mp} H_{\pm 1}^{-1} U_{\pm} \quad (2.86)$$

The definition of a self-energy allows to elegantly rewrite the Floquet-Dyson equation for the zero-th mode:

$$G_0(E) = g_0(E) + g_0(E) \Sigma_{AC}^R(E) G_0(E) \quad (2.87)$$

Even if not immediately obvious, we can reformulate the expression above in such a way to make it resembles eq. 2.19. This can be done by left-multiplying the equation by  $g_0^{-1}$  and right-multiplying by  $G_0^{-1}$ . The resulting expression will have terms proportional to  $g_0^{-1} g_0$  and  $G_0 G_0^{-1}$  that are equal to the identity matrix. In the end we would have an equation like 2.89.

$$g_0^{-1}(E) G_0(E) G_0^{-1}(E) = g_0^{-1}(E) g_0(E) G_0^{-1}(E) + g_0^{-1}(E) g_0(E) \Sigma_{AC}^R(E) G_0(E) G_0^{-1}(E) \quad (2.88)$$

$$G_0^{-1}(E) = g_0^{-1}(E) - \Sigma_{AC}^R(E) \quad (2.89)$$

Writing explicitly the expression for  $g_0^{-1}$  using eq. 2.69, we obtain an equation for  $G_0$  that is identical to the Dyson's equation in steady-state condition, but in this case we have an additional self-energy coming from the perturbation .

$$G_0(E) = [EI - H_{mol,0} - \Sigma^R(E) - \Sigma_{AC}^R(E)]^{-1} \quad (2.90)$$

The final step is to compute all the other Floquet modes starting from  $G_0$  and exploiting the following equation which is a generalization of eq. 2.79:

$$G_{\pm n}(E) = H_{\pm n}^{-1}(E) U_{\pm} G_{\pm(n-1)}(E), \quad n > 0 \quad (2.91)$$

This step allows then to compute the DC current using the Floquet modes. For the sake of clarity, the main steps of the overall recursive scheme are summarized here below.

- Choice of a maximum order  $n_{max} > 0$  such that the cutoff energy  $E_{max} = n_{max} \hbar \omega$  is much larger than any other energy scale in the problem.
- Computation of  $H_{\pm n_{max}}^{-1}$ , arbitrary taken as :

$$H_{\pm n_{max}}^{-1}(E) = g_{\pm n_{max}}(E) = g_0^R(E \mp n_{max} \hbar \omega) \quad (2.92)$$

- Recursive evaluation of eq. 2.84, starting from  $H_{\pm n_{max}}^{-1}$ , until  $H_{\pm 1}^{-1}$  is obtained.
- Computation of  $\Sigma_{AC}^R$  using  $H_{\pm 1}^{-1}$ .
- Evaluation of  $G_0$  using Floquet-Dyson equation for the zeroth-order.
- Recursive computation of all  $G_n$ .

The next step is to evaluate current using the  $G_n$ , procedure that is described in the following paragraph.

### Current evaluation

The current equation used to compute the DC current is the same adopted for TG model where the only difference is in the way transmission coefficients are computed. For clarity I report here below eq. 2.35.

$$I_{DC} = \frac{2e}{\hbar} \sum_{n=-\infty}^{\infty} \int [T_{21}^{(n)}(E)f_1(E) - T_{12}^{(n)}(E)f_2(E)]dE$$

The transmission coefficients from one contact to another, corresponding to interaction events with  $n$  photons, are obtained with these following equations that have been demonstrated by Stefanucci in [55] and by Hänggi and coworkers in [30]:

$$T_{21}^{(n)}(E) = \text{Tr} [\Gamma_1(E)G_n^\dagger(E)\Gamma_2(E - n\hbar\omega)G_n(E)] \quad (2.93)$$

$$T_{12}^{(n)}(E) = \text{Tr} [\Gamma_2(E)G_n^\dagger(E)\Gamma_1(E - n\hbar\omega)G_n(E)] \quad (2.94)$$

Some considerations done with the TG model based on junction symmetry can be repeated also in this context. In particular, if the junction is symmetric, i.e.  $\Gamma_1(E) = \Gamma_2(E)$ , the two transmission coefficients are equal, hence in short-circuit condition is impossible to develop a net current different from zero. The advantage in this case is the possibility to define, as in TG, a total transmission spectrum:

$$T_{opt} = \sum_n T_{21}^{(n)} = \sum_n T_{12}^{(n)} \quad (2.95)$$

With respect to TG model, Floquet should take into account the intermolecular transitions between the energy levels. On the other hand, Floquet algorithm is computationally heavier due to matrix inversion involved in the recursive computation of  $H_{\pm n}^{-1}$  and for the computation of  $G_0$ . In addition, the matrix inversions should be repeated for each value of the chosen energy grid, but also for each bias point considered in the evaluation of the characteristics. The total number of inversions that should be computed depends also on the maximum order  $n_{max} > 0$ , that represents the cutoff of Floquet modes. In the end we would have:

$$N_{inv} = (2n_{max} + 1) \cdot N_{energy} \cdot N_{bias} \quad (2.96)$$

The dimension of the energy grid is indicated by  $N_{energy}$  whereas  $N_{bias}$  corresponds to the number of bias voltages used to evaluate the  $IV$  curve. Of course this algorithm is computationally demanding when considering a large number of basis functions since it increases the dimensions of the matrices that must be inverted. Nevertheless, when a simple model is considered, like the 0D-transport model described in this chapter, the dimensions of the matrices involved in the algorithm depends on the number of energy levels considered for the molecule, i.e. the 0D-system, placed between the contacts. For example if  $N_{levels}$  energy levels are considered, the quantities involved would have  $N_{levels} \times N_{levels}$  dimensions that can be limited considering, for instance,  $N_{levels} = 4$ . This would be the case considered for Floquet model implementation in MATLAB<sup>®</sup> and will be described more in detail in the next chapter.

Last considerations can be done on the limits of Floquet model. In this section I have considered only the monochromatic case, however it can be generalized for more harmonics, but the algorithm would be too computationally demanding. Another drawback is that the model cannot be applied to non time-periodic perturbation since a full-time dependent approach is required. Examples of such schemes are presented by M. Galperin in [49], [56]. An additional study on these schemes could be a good starting point for future thesis works based on this topic.

## 2.4 SCBA for electron-photon interaction

The third and last model described in this chapter is based on NEGF, in particular on how is possible to include electron-photon scattering processes. This model is the one implemented in the software *QuantumATK* developed by SYNOPSIS<sup>®</sup>. The references indicated by the manual [57], that were consulted for model implementation, are [58], [59], [60], [61], [62]. In this section I will present the model especially following reference [58], which describes electron-photon interaction for a resonant tunneling diode, but also the notes taken from the doctoral course “Analisi di dispositivi optoelettronici mediante la teoria delle funzioni di Green fuori equilibrio” taught by professor F. Bertazzi in 2021 at Politecnico di Torino. Another useful reference containing a formal description of NEGF is the PhD dissertation of U. Aeberhard [63] that is focused more on photovoltaic applications.

For the sake of simplicity, the description that will be given of the model does not contain all the theoretical details needed to have a thorough knowledge of NEGF since the complexity is very high and lies outside the goal of this thesis. The main idea is to describe the general reasoning behind the model, without demonstrating everything, and give to the reader a simple guide to compute the photocurrent using *QuantumATK*.

A good starting point to include the interaction between electrons and photons

is to rewrite the Dyson's equation in a different way. As already said in section 2.1, the non-equilibrium Green's function can be seen as the impulse response of a system. However, there is another interpretation that is deeply connected to its formal definition. Indeed the non-equilibrium Green's function can be interpreted as the propagator of a particle state over space and time. In particular, the function  $G(\vec{r}_2, t_2, \vec{r}_1, t_1)$  expresses a correlation between two times  $t_1$  and  $t_2$  and two positions  $\vec{r}_1$  and  $\vec{r}_2$ . For  $t_2$  later than  $t_1$  the Green's function encodes the reaction of a system to the creation of a particle in state  $(\vec{r}_1, t_1)$ , with consequent propagation of the perturbation to state  $(\vec{r}_2, t_2)$  where is annihilated.

From a mathematical point of view,  $G$  is computed as a non-equilibrium statistical average over an ensemble of particles (for example electrons) and the variable  $G_0$  (not to be confused with the zero-th Floquet mode of the previous section) indicates the *free* propagator, i.e. the propagator of a particle which is non-interacting, therefore corresponding to a system that is at equilibrium. To include an external influence that moves the systems out of equilibrium, a perturbation expansion is needed to compute the propagator  $G$ , which is the interacting Green's function or, in other words, the propagator that considers the influence of an interaction acting on a particle. The interaction can be of different type such as the influence of state reservoirs on a system or the interaction between electrons and phonons or photons. As already introduced, the general way to include an interaction is to define a corresponding self-energy which is used to compute the non-equilibrium Green's function of the system. Each self-energy is constituted by more terms coming from a perturbation expansions of the Green's function. The most known are Hartree and Fock terms, at first order, and direct and exchange term at second order. Generally the expansion is truncated at first order and the resulting self-energy is used inside the Dyson's equation. This approximation is called first-order Born approximation. However this procedure is not fully consistent because self-energies and Green's functions generally depend on each other. To understand better this concept I will make an example. An electromagnetic field incident on an electronic system will influence the behavior of electrons, but in turn the response will modify in some way the incident field, hence a self-consistent solution is needed. In NEGF the procedure used to find self-energies and Green's functions is called self-consistent Born approximation (SCBA) and consists of an *inner* loop linking the Dyson's equation with the equations used to compute the self-energies. For what concerns the perturbative expansion, achieving self-consistency means that higher order terms are included in *dressed* first order terms used in the computation. The advantage is that a sum over infinite orders is now represented by two effective terms. Only in this way conservation laws for carrier densities and currents are satisfied.

Curiously, for only one case self-consistent loop is not needed and is when considering contacts self-energies with no scattering mechanisms involved during

transport. In this case  $\Sigma$  can be computed exactly without needing any loop with Dyson's equation.

In light of just said, Dyson's equation resulting from perturbative expansion has the following equivalent matrix forms:

$$G = G_0 + G_0 \Sigma G \quad (2.97)$$

$$G = G_0 + G \Sigma G_0 \quad (2.98)$$

These equations are not so similar to Dyson's equation expressed in eq. 2.19, however it is possible to prove that, dividing  $G$  in different terms over a time contour integral, under steady-state condition the two expressions are equivalent (see [63]).

Now the problem is to understand how to obtain an expression for the self-energy  $\Sigma_{ph}$  corresponding to the interaction between electrons and photons. The first thing to do is to write down the Hamiltonian and identify the term corresponding to the perturbation of the system. The single electron Hamiltonian including the effects of a monochromatic electromagnetic field has the following general expression:

$$\hat{H} = \frac{[\hat{p} + e\hat{A}(\vec{r}, t)]^2}{2m} + U_{eff} \quad (2.99)$$

The first terms in this equation take in consideration the variation of momentum operator  $\hat{p}$  (that is a vector) by the vector potential  $\hat{A}(\vec{r}, t)$  of the incident radiation, that has a direction parallel to field polarization. At the denominator,  $m$  is the (effective) mass of the electron, whereas  $U_{eff}$  includes the terms corresponding to the electron-electron interaction, that are the Hartree and the exchange potential, but also a possible external applied potential (a bias). Developing the terms in brackets, the Hamiltonian becomes:

$$\hat{H} = \frac{\hat{p}^2}{2m} + \frac{e}{m} \hat{p} \cdot \hat{A}(\vec{r}, t) + \frac{e^2}{2m} \hat{A}^2(\vec{r}, t) \quad (2.100)$$

The term proportional to the squared vector potential is negligible when considering the electromagnetic potential as a weak interaction, hence it is relevant only at higher intensities for taking into account non-linear effects. This is the so called dipole approximation where the perturbation is identified by the second term:

$$\hat{H}_{e-ph} = \frac{e}{m} \hat{p} \cdot \hat{A}(\vec{r}, t) \quad (2.101)$$

This is the coupling term expressing the interaction between an electron and an electromagnetic field, that will be the input for computing the electron-photon (e-ph) self-energy. In order to do this it is necessary to express the coupling Hamiltonian in second quantization, starting from the vector potential. A monochromatic

single-mode plane wave corresponds to a vector potential expressed in the following quantized form, using bosonic annihilation ( $\hat{b}$ ) and creation ( $\hat{b}^\dagger$ ) operators:

$$\hat{A}(\vec{r}, t) = \hat{A}_0(\vec{r}) (\hat{b}e^{-i\omega t} + \hat{b}^\dagger e^{i\omega t}) \quad (2.102)$$

$\hat{A}_0(\vec{r})$  is the amplitude of the potential having direction parallel to the polarization of the incident field, whereas  $\omega$  is the frequency of the field. Bosonic operator  $\hat{b}$  represents the annihilation of a photon with energy  $\hbar\omega$  while  $\hat{b}^\dagger$  corresponds to the creation of a new photon with energy  $\hbar\omega$ . In order to find the amplitude of the potential, it is possible to choose a vector potential satisfying the Lorenz gauge:

$$\nabla \cdot \hat{A}(\vec{r}, t) + \epsilon\mu \frac{\partial \phi(\vec{r}, t)}{\partial t} = 0 \quad (2.103)$$

where  $\phi(\vec{r}, t)$  is the electrostatic scalar potential,  $\mu$  is the magnetic permeability and  $\epsilon$  is the dielectric permittivity, both referred to the material under study. Under this condition, the amplitude  $\hat{A}_0$  is found by the Helmholtz equation:

$$\nabla^2 \hat{A}_0(\vec{r}) + \frac{\omega^2}{c^2} \hat{A}_0(\vec{r}) = 0 \quad (2.104)$$

A general solution of the above equation is expressed as  $\hat{A}_0(\vec{r}) = e^{ik \cdot r}$ , where  $k$  is the wave vector related to frequency and material properties by:

$$k = \frac{\omega}{c} \sqrt{\epsilon_r \mu_r} \quad (2.105)$$

In this expression  $\epsilon_r$  is the relative dielectric constant and  $\mu_r$  the relative magnetic permeability. When the system under study is isotropic with homogeneous permeability and dielectric constant, averaging over time to eliminate the oscillating components allows to express the final expression of the vector potential as:

$$\hat{A}(\vec{r}, t) = \left( \frac{\hbar \sqrt{\epsilon_r \mu_r}}{2N\omega\epsilon c} F_{ph} \right)^{1/2} (\vec{a} \hat{b} e^{-i\omega t} + (\vec{a})^* \hat{b}^\dagger e^{i\omega t}) \quad (2.106)$$

Relevant quantities in the above equations are:

- $\vec{a}$  is the polarization unit vector of the incident field. It is generally complex in order to consider each possible polarization such as circular ones.
- $N$  is the total number of photons populating the single monochromatic mode.
- $F_{ph}$  is the photon flux incident on the system and is expressed as  $F_{ph} = Nv/V = Nc/\sqrt{\epsilon_r \mu_r}$  where  $v = c/\sqrt{\epsilon_r \mu_r}$  is the electron velocity inside the system and  $V$  is the overall volume of the considered system. The photon flux will be the photon-field strength parameter.

Now is possible to express the coupling Hamiltonian using fermionic operators. In particular, it is important to know that in second quantization the expression for a one electron operator  $\mathcal{O}$  is:

$$\mathcal{O} = \sum_{ij} o_{ij} c_i^\dagger c_j \quad (2.107)$$

where  $o_{ij} = \langle i|o|j\rangle$  are the matrix elements of the operator computed using basis functions with index  $i$  and  $j$ . *QuantumATK* is based on Linear Combination of Atomic Orbitals (LCAO), therefore in this case the indices refer to atomic orbitals. Using  $\hat{H}_{e-ph}$  in place of  $\mathcal{O}$ , we are finally able to express the perturbation term:

$$\hat{H}_{e-ph} = \sum_{ij} \langle i|\hat{H}_{coupl}|j\rangle c_i^\dagger c_j \quad (2.108)$$

$$\hat{H}_{e-ph} = \sum_{ij} M_{ij} (\hat{b} e^{-i\omega t} + \hat{b}^\dagger e^{i\omega t}) c_i^\dagger c_j \quad (2.109)$$

The matrix elements  $M_{ij}$  of the coupling matrix  $M$  are defined substituting eq. 2.101 and 2.106 inside eq. 2.108:

$$M_{ij} = \frac{e}{m} \left( \frac{\hbar \sqrt{\epsilon_r \mu_r}}{2N\omega\epsilon c} F_{ph} \right)^{1/2} \langle i|\hat{p} \cdot \vec{a}|j\rangle \quad (2.110)$$

It is worth notice that the coupling elements are proportional to the product between the momentum operator and the polarization unit vector. Depending on the symmetry of atomic orbitals used to compute the matrix elements, some transitions would be forbidden while others would be possible.

Finally, under steady-state condition and assuming that the photon population remains at equilibrium, the first order self-consistent Born approximation leads to the following expression for the lesser and greater component of e-ph self-energy:

$$\Sigma_{ph}^<(E) = \left[ N M G^<(E - \hbar\omega) M^\dagger + (N + 1) M^\dagger G^<(E + \hbar\omega) M \right] \quad (2.111)$$

$$\Sigma_{ph}^>(E) = \left[ N M^\dagger G^>(E + \hbar\omega) M + (N + 1) M G^>(E - \hbar\omega) M^\dagger \right] \quad (2.112)$$

These self-energies are written in the self-consistent picture because the input arguments are the lesser and greater interacting Green's function. Moreover they couple different points in space through the coupling matrix  $M$ , but also different energy states are coupled because the input Green's functions are evaluated at  $E \pm \hbar\omega$  and not at  $E$ . Since these self-energies correspond to in- or out-scattering rates via optical excitations, the first term of  $\Sigma_{ph}^<$  can be interpreted as the excitation of an electron in state  $E - \hbar\omega$  to state  $E$  after absorbing a photon energy  $\hbar\omega$ . This process is proportional to the total number of electrons  $N$  which is coherent to what known in semiconductor physics. Similarly, the second term corresponds to the emission of a photon energy  $\hbar\omega$  by an electron moving from state  $E + \hbar\omega$  to

state  $E$ . This emission can be “spontaneous” or “stimulated” by the external field and indeed is proportional to  $(N+1)$  where the 1 is referred to the spontaneous contribution. A similar interpretation can be associated to  $\Sigma_{ph}^>$  but considering holes instead of electrons. In this case the in-scattering rate for holes corresponds to an out-scattering rate for electrons from state  $E$  to state  $E \pm \hbar\omega$ .

Starting from the lesser and greater component is also possible to find the corresponding retarded self-energy:

$$\Sigma_{ph}^R(E) = \frac{1}{2} [\Sigma_{ph}^>(E) - \Sigma_{ph}^<(E)] - i\mathcal{P} \left\{ \int \frac{dE'}{2\pi} \frac{\Sigma_{ph}^<(E) - \Sigma_{ph}^>(E)}{E - E'} \right\} \quad (2.113)$$

The retarded self-energy is anti-Hermitian and hence responsible for dephasing of charge transport. Instead the principal value integral term is Hermitian and it is usually neglected since it has a very small imaginary part that do not affects carriers lifetime. Moreover, its real part leads to an energy renormalization of around 1% of the total real part of the energy, hence the total principal value integral can be safely ignored.

Exploiting the above self-energy, it is now possible to compute all retarded Green’s functions, but also its lesser and greater component that would be the new input of the self-consistent procedure.

$$G^R = [EI - H_0 - \Sigma^R]^{-1} \quad , \quad \Sigma^R = \Sigma_{C1}^R + \Sigma_{C2}^R + \Sigma_{ph}^R \quad (2.114)$$

$$G^< = G^R \Sigma^< G^A \quad , \quad \Sigma^< = \Sigma_{C1}^< + \Sigma_{C2}^< + \Sigma_{ph}^< \quad (2.115)$$

In eq. 2.114  $H_0$  is the Hamiltonian in the absence of radiation, while  $\Sigma^R$  is the retarded self-energy obtained summing the contact self-energy to the e-ph self-energy. It is worthwhile to underline that in eq. 2.115 the input Green’s function are referred to the interacting picture, hence the equation refers to a generic iteration during the self-consistent loop. For the first iteration,  $\Sigma_{ph}^<$  and  $\Sigma_{ph}^R$  will be computed using the non-interacting Green’s function  $G_0^{R/A}$  and  $G_0^<$  that, in this case, include only the influence of the contacts and are computed using equations 2.19, 2.20 and 2.24. The resulting self-energies are then used inside equations 2.114 and 2.115 along with  $G_0^{R/A}$  and  $G_0^<$  to obtain the interacting Green’s functions of the first iteration. The procedure is repeated until self-energies and Green’s function do not change anymore within a certain tolerance. With the converged results is possible to compute all the relevant quantities such as the total current density and carriers density. Normally, in a semiconductor device, in order to guarantee the inclusion of space-charge effects, an additional self-consistent loop is considered between the SCBA procedure and the Poisson’s equation. In particular, the converged carriers density of SCBA will be the input of the Poisson’s equation whose solution updates the Hartree potential included in  $H_0$ . This procedure is called “outer loop” in order to distinguish it from the SCBA loop. The direct iteration between NEGF

equations and Poisson's equation is not stable and different strategies are used to stabilize and speed up the algorithm. The figure below summarizes the complete algorithm that must be followed to guarantee self-consistency. In light-blue is shown the inner loop related to SCBA while in green is represented the outer loop related to NEGF-Poisson iteration. After convergence is achieved, is possible to compute

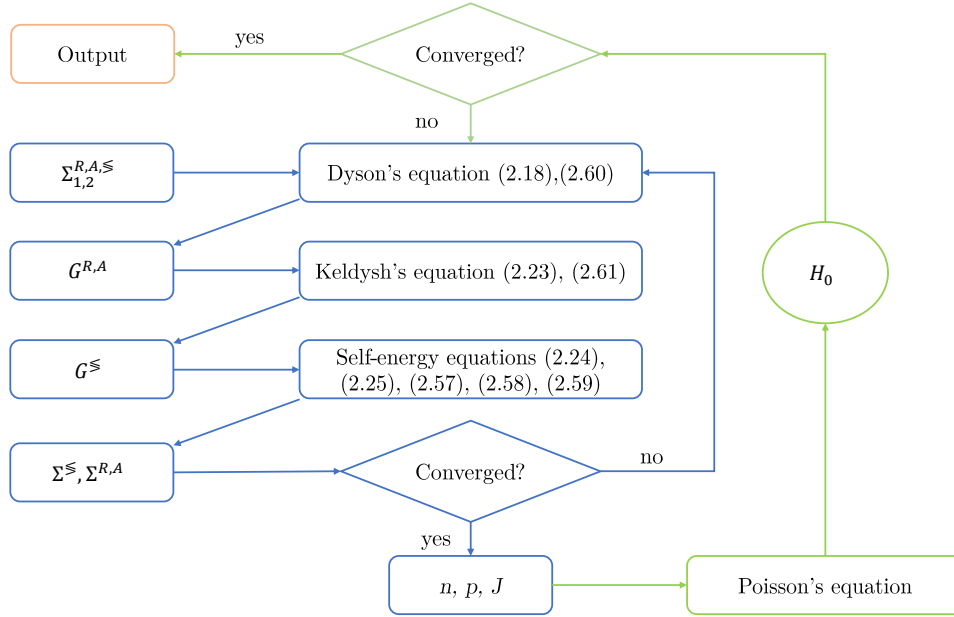


**Figure 2.13:** Diagram that summarizes the SCBA procedure (inner loop) considering also direct iteration between NEGF and Poisson's equation (outer loop). Near the name of the equations there are the corresponding numeric labels referred to those reported in the text.

the output current that includes the effects of photo-assisted transport. This self-consistent algorithm represents the state of the art of quantum transport, but at the same time is really computationally expensive. Moreover, in *QuantumATK* things are a bit simplified and I will described them here below.

### Computation of photocurrent with QuantumATK

As reported in the manual [57], *QuantumATK* adopts the first order perturbative expansion of the self-energy in order to include the interaction between electrons and photons, but do not achieve self-consistency with an inner loop. As mentioned above, this case is called first-order Born approximation and of course is a simplification since carrier densities and current conservation is not guaranteed. More in detail, the equations commented above are now evaluated using the non-interacting Green's function  $G_0^{\lessdot}$  (obtained with eq. 2.24) in order to compute  $\Sigma_{ph}$  and then evaluate

the interacting Green's function  $G^{\lessgtr}$ . This is equivalent to the first iteration of the inner loop that is coherent with what commented previously. For completeness I report here below the equations used by *QuantumATK*.

$$\Sigma_{ph}^<(E) = \left[ NMG_0^<(E - \hbar\omega)M^\dagger + (N + 1)M^\dagger G_0^<(E + \hbar\omega)M \right] \quad (2.116)$$

$$\Sigma_{ph}^>(E) = \left[ NM^\dagger G_0^>(E + \hbar\omega)M + (N + 1)MG_0^>(E - \hbar\omega)M^\dagger \right] \quad (2.117)$$

$$G^{\lessgtr} = G_0^R(\Sigma_{C1}^{\lessgtr} + \Sigma_{C2}^{\lessgtr} + \Sigma_{ph}^{\lessgtr})G_0^A \quad (2.118)$$

With the lesser and greater Green's functions and self-energies is possible to define an effective transmission coefficient needed to compute the total current flowing in steady state condition in one of the two contacts. Taking inspiration from eq. 2.28 is easy to see that the current flowing through contact  $\alpha \in \{C1, C2\}$ , leaving the device volume, can be computed defining an effective transmission spectrum as:

$$T_\alpha^{(e-ph)}(E) = \text{Tr} \left[ \Sigma_\alpha^<(E)G^>(E) - \Sigma_\alpha^>(E)G^<(E) \right] \quad (2.119)$$

where  $G^{\lessgtr}$  are the interacting Green's functions, whereas the self-energies are only the one of the contacts. Developing the contact self-energies is possible to rewrite the effective transmission in a slightly different way, that is the one reported in the manual:

$$T_\alpha^{(e-ph)}(E) = \text{Tr} \left\{ i\Gamma_\alpha(E) \left[ (1 - f_\alpha(E))G^<(E) + f_\alpha(E)G^>(E) \right] \right\} \quad (2.120)$$

The Fermi-Dirac distribution in contact  $\alpha$  is expressed by  $f_\alpha$  and it comes out from the fluctuation-dissipation theorem. I would like to underline that this expression is wrongly reported in the manual since square brackets are missing, while in the reference article [60] they are clearly present.

Then the total current can be computed with a Landauer-like equation where spin degeneracy is considered:

$$I_\alpha = \frac{2e}{\hbar} \int_{-\infty}^{+\infty} T_\alpha^{(e-ph)}(E) dE \quad (2.121)$$

The total current corresponds to the sum between dark current and photocurrent, hence if you want to compute the latter is enough to do  $I_{\alpha,ph} = I_\alpha - I_{\alpha,dark}$ . In *QuantumATK*,  $I_{\alpha,ph}$  can be computed with the device analysis object "Photocurrent" that allows to evaluate  $I_{\alpha,ph}$  at a specific bias for different photon energies. The result of the simulation is the photocurrent expressed as a function of the incident photon flux, the temperature of the environment and the properties of the medium (the relative dielectric constant and relative magnetic permeability). These variables can be chosen by the user and are just scalar numbers. This is of course another approximation since the considered system can be anisotropic and inhomogeneous.

Moreover, dielectric constant and magnetic permeability refer to the device region that can correspond to a molecule in case of single-molecule junctions. Of course the dielectric properties of the central region would highly inhomogeneous and is even problematic to define a dielectric constant. Instead, less problematic is the photon flux incident on the device region. It is expressed in  $\text{\AA}^{-2}\text{s}^{-1}$  and represents just a scalar factor that directly multiply the photocurrent. For example if the flux is increased by a factor of 2, also the photocurrent will follow the same increase.

The “Photocurrent” object works only with an electronic structure computed with DFT, that is strange since the Born approximation could be computed, in theory, also with a semi-empirical model. However, it is not so clear if using another model would decrease the computational time needed for photocurrent evaluation. The procedure is not self-consistent therefore it should not involved a direct loop with the model used to compute the electronic structure. The manual again is not clear enough to understand these details. What is sure is that the photocurrent simulations are slow and require a lot of times ranging from days to weeks depending on the number of photon energies considered in the simulation. For example, the computation of photocurrent for a single-molecule junction, considering a 3TT between two gold contacts, required  $\approx 5$  days of simulation for a single bias point, 49  $k$ -points and 45 values of the photon energy using a Double Zeta Polarized (DZP) basis set.

Another ambiguous behavior of “Photocurrent” object is the convention used for source and drain with respect to the one used to compute the dark current. To compute the latter, *QuantumATK* uses NEGF considering as drain the left electrode and as source the right electrode (the convention is switched compared to the one used in section 2.1). On the other hand, the photocurrent is evaluated considering as source the left contact and as drain the right contact (same convention of section 2.1). Therefore, if a positive bias is applied to the left electrode, the dark current will be positive flowing from left to right while the photocurrent will be negative, hence the photocurrent will flow in opposite direction to the applied external field. Of course this should not be excluded *a priori*, but in this case it is just the effect of the opposite convention adopted by the two tools inside the software. Therefore, to obtain a positive photocurrent, the bias applied to the right electrode must be positive. The resulting dark current will be negative, but the computed photocurrent will be positive. Table 2.1 summarizes the conventions just commented that are adopted by *QuantumATK*.

Arrived at this point, it is crucial to understand what are the limits of this model since self-consistency is not achieved in the simulation. An assumption made above is that the interaction between the electromagnetic field and the system is weak, that means the field is considered as a perturbation that is plausible only when considering a small intensity regime. The incident photon flux cannot be increased as you want because at some point you will exit from the validation region of the

Convention	Dark current	Photocurrent
Source	Right contact	Left contact
Drain	Left contact	Right contact
Current direction	$I_{dark} > 0$ from left to right	$I_{ph} > 0$ from right to left

**Table 2.1:** Convention adopted by *QuantumATK* for dark current and photocurrent computation.

model. Within the low intensity limit, it is possible to evaluate quantities that are linear with the photon flux  $F_{ph}$  like the linear component of the photocurrent. Therefore the truncated sequence of the SCBA can allow to describe the linear response for weakly interacting field. On the other hand, all other nonlinear optical effects can be described only when self-consistency is achieved between Green's functions and self-energies.

There is a simple reasoning to understand the reason why the photocurrent is linear with the photon flux. If absorption terms dominate over emission, the terms in the e-ph self-energies proportional to  $N + 1$  can be neglected. In this case the photon number  $N$ , multiplying absorption terms, cancels out with the  $N$  at the denominator coming from matrices  $M$  and  $M^\dagger$ . Therefore the self-energies are proportional to  $F_{ph}$  which comes out from the matrix multiplication. This proportionality does not immediately imply that the current is linear with photon flux since self-consistency should be achieved. However, if the procedure is truncated, the interacting Green's functions will also be proportional to  $F_{ph}$  because they are directly proportional to the e-ph self-energy. As a consequence, also the total current will be proportional to  $F_{ph}$  that means is linear with photon flux.

The assumption of weak interaction between the electromagnetic field and the system under analysis implies two important physical consequences [58]:

- i. The underlying single-electron state structure is not appreciably disturb by the electromagnetic radiation. In other words, the non-interacting  $G_0^R$ , which represents the single-electron dynamics of the system, may be used to describe the single-electron dynamics of the interacting electron-photon system.
- ii. Electrons that are excited by a photon cannot subsequently be excited by another photon, that is unlikely if the photon field is weak. Then, only single-photon interaction events are considered in the low intensity limit.

These considerations are crucial to understand which physics can be described by the model implemented in *QuantumATK*.

Lastly, it is interesting to rewrite eq. 2.121 for the evaluation of current in order to have an other phenomenological interpretation of the transmission coefficient. This alternative expression for current, found in [61] and [62], considers only

absorption of photons, hence only the terms in self-energies proportional to  $N$ . In this case a Fermi’s golden rule like expression is obtained and the current induced by absorption of photons is:

$$I_{\alpha,ph} = \frac{2e}{\hbar} \int_{-\infty}^{+\infty} \sum_{\beta \in \{C1, C2\}} [1 - f_{\alpha}(E)] f_{\beta}(E - \hbar\omega) T_{\alpha,\beta}^{-}(E) - f_{\alpha}(E) [1 - f_{\beta}(E + \hbar\omega)] T_{\alpha,\beta}^{+}(E) dE \quad (2.122)$$

$$T_{\alpha,\beta}^{-}(E) = N \text{Tr} [M A_{\beta}(E - \hbar\omega) M^{\dagger} \tilde{A}_{\alpha}(E)] \quad (2.123)$$

$$T_{\alpha,\beta}^{+}(E) = N \text{Tr} [M^{\dagger} A_{\beta}(E + \hbar\omega) M \tilde{A}_{\alpha}(E)] \quad (2.124)$$

$$A_{\alpha}(E) = G_0^R(E) \Gamma_{\alpha}(E) G^A(E) \quad (2.125)$$

$$\tilde{A}_{\alpha}(E) = G_0^A(E) \Gamma_{\alpha}(E) G^R(E) \quad (2.126)$$

$A_{\alpha}$  is the spectral function of lead  $\alpha$  computed with the non-interacting Green’s functions, whereas  $\tilde{A}_{\alpha}$  is the time reversed spectral function. Instead,  $T_{\alpha,\beta}^{-}(E)$  represents the transmission coefficient for an electron, with initial state in contact  $\beta$  at energy  $E - \hbar\omega$ , that undergoes a single-photon absorption event while moving across the device to reach contact  $\alpha$  at energy  $E$ . Similarly,  $T_{\alpha,\beta}^{+}(E)$  corresponds to the transmission coefficient for a hole, with initial state in contact  $\beta$  at energy  $E + \hbar\omega$ , that undergoes a single-photon absorption event while crossing the device to reach contact  $\alpha$  at energy  $E$ . Equation 2.122 takes in consideration these fluxes of electrons and holes to compute the total current into contact  $\alpha$ . In particular there are the so called “Pauli blocking factors” that are coefficients derived from Fermi-Dirac distribution. More in detail, for electrons they weigh the number of occupied states in contact  $\beta$  (proportional to  $f_{\beta}$ ) and the number of available states in contact  $\alpha$  (proportional to  $1 - f_{\alpha}$ ). A similar reasoning can be done for the transmission of holes.

This expression of current is directly related to absorption events, i.e. represent just the photocurrent, and has an easy interpretation. In Appendix B I have shown how to derive eq. 2.122 starting from 2.120 and 2.122. The alternative formulation of current, in terms of transmission coefficient from one contact to another, it is also important because it seems that *QuantumATK* uses this formalism even if not explicitly reported in the manual. Indeed the default option to compute the photocurrent is to neglect emission events that is analogous to what done in the above formulation. The output of photocurrent simulation is stored in a HDF5 data structure where are also saved all the transmission coefficients  $T_{\alpha\beta}^{\pm}$ . Nevertheless, it is difficult to interpret these spectra and it is not clear how to obtain the photocurrent starting from them. Moreover, they are probably expressed in atomic units and the conversion is not so straightforward. There is also another command that can be used to compute the photon-mediated transmission. After the simulation has finished, is possible to use the method `photonMediatedTransmission` that gives

as output the photon-mediated transmission for electrons or for holes depending on which carrier has been specified. In this case the spectra are not expressed in atomic units and are just probability amplitudes.

What just written should be enough to understand the model implemented in *QuantumATK*, whose simulations are reported in the next chapter, in order to compare them with the results obtained from the implementation of TG and Floquet model.

## Chapter 3

# Photo-assisted tunneling simulator

In this chapter I will show how I have implemented Tien-Gordon and Floquet model in MATLAB<sup>®</sup> starting from EE-BESD, that is an efficient implementation of 0D-transport for molecular junctions. Then, I will describe a comparison between the models for a single-molecule junction, based on terthiophene (3TT), going in detail on the dependence of photocurrent from the simulation parameters such as the photon flux, the photon energy and the amplitude of the oscillating energy potential term. Lastly, the models will be compared with the more sophisticated *QuantumATK* simulations and with the experimental measurement of photocurrent for a molecular junction based on octane (C8) done by R. Arielly and coworkers [20].

### 3.1 EE-BESD

The Tien-Gordon and Floquet model described in Chap. 2 have been implemented starting from an efficient modeling of 0D-transport for single-molecule junction that takes into account the effects of polarization on molecular orbitals. The model was developed by the PhD candidate A. Zahir at Politecnico di Torino in 2015 [41] and its name, EE-BESD, stands for: Efficient and Effective model based on Broadening level, Evaluation of peaks, SCF and Discrete levels. The implementation follows the scheme represented in fig. 2.3 where the current is computed for each value of the applied bias  $V_{DS}$ . The main difference is that in EE-BESD the transmission spectrum can change shape depending on the applied voltage. Indeed, thanks to *ab-initio* simulations, it is known that transmission peaks can vary their width and height depending on  $V_{DS}$ . It is difficult to know *a priori* if a transmission channel will be enhanced or suppressed, therefore EE-BESD takes into account these effects

thanks to a fitting procedure on simulations done with *ab-initio* methods such as DFT-NEGF or EHT-NEGF. The main idea is to compute the transmission spectrum of the single-molecule junction for some points of the  $IV$  characteristics. The next step is to isolate a certain number of transmission peaks contributing to conduction, generally two peaks below  $E_F$  and two above it, and analyze how their height and width change when the bias is varied. In particular, from the average of the widths of a certain peak we obtain the total coupling  $\gamma_i$  of the discrete level  $i$ , centered in the middle of the corresponding peak at equilibrium. Since only symmetric junctions are considered in EE-BESD, the total coupling can be equally divided in two terms corresponding to  $\gamma_{i,1} = \gamma_i/2$  and  $\gamma_{i,2} = \gamma_i/2$ , that determine the contribution to broadening coming from the two contacts. Instead, for what regards the variation of the peak height, a polynomial interpolation is done in order to obtain a function  $h_i(V_{DS})$  that allows to approximately compute the value of the height, corresponding to level  $i$ , as a function of  $V_{DS}$ :

$$h_i(V_{DS}) = c_{i,1}|V_{DS}|^2 + c_{i,2}|V_{DS}| + c_{i,3} \quad (3.1)$$

The coefficients  $c_{i,1}$ ,  $c_{i,2}$ ,  $c_{i,3}$  come from interpolation that is generally done with a second-order polynomial. The applied voltage is considered in modulus since only symmetric junctions are analyzed in EE-BESD, hence the  $IV$  characteristic is symmetric with respect to the origin and the variation of the transmission spectrum is the same when the sign of the bias is reversed.

The total transmission spectrum of the 0D model is obtained from the sum of transmission coefficients related to different levels (see eq. 2.16):

$$T(E) = \sum_i T_i(E - U_{SCF}) \quad (3.2)$$

where  $T_i(E - U_{SCF})$  refers to level  $i$  after the computation of the self-consistent potential. Instead in EE-BESD the total transmission, influenced by the applied bias, is computed by multiplying each transmission  $T_i$  by the corresponding height fitting function  $h_i$ :

$$T(E, V_{DS}) = \sum_i h_i(V_{DS})T_i(E - U_{SCF}) \quad (3.3)$$

What it is important to highlight is that there is one fitting function for each transmission peak. In the MATLAB<sup>®</sup> implementation used in this thesis, the multiplication between  $h_i$  and  $T_i$  is done by the function `applyVds` which has as inputs the voltage  $V_{DS}$  and the transmission spectra  $T_i$ , and as output the transmission spectra modified by orbital polarization. A schematic summary of the EE-BESD algorithm is shown in fig. 3.1.

The crucial point in EE-BESD is the fitting procedure because it is the step that allows to reproduce the *ab-initio* results with a simpler 0D-model. Once the fitting

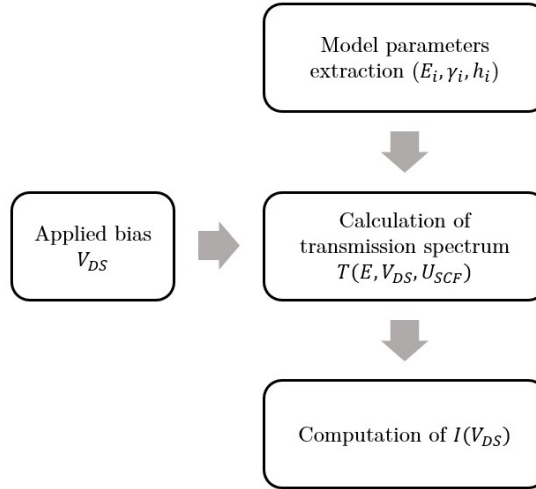


**Figure 3.1:** Schematic summary of the algorithm implemented in EE-BESD.

is done, you can compute the characteristics any time you want for any value of bias inside the range adopted in the *ab-initio* simulation of the molecular junction. Most of the effort is therefore directed to the fitting of the transmission spectrum. The procedure adopted by A. Zahir is not described in detail, hence I have developed the methodology represented in fig. 3.2. After having chosen the bias range, the *IV* curve is computed in *QuantumATK* for 11 values of  $V_{DS}$ . Only positive voltages are considered due to the symmetry of the analyzed junctions, hence the characteristics should be the same from positive and negative bias points, except for a minus sign. Then, the peaks involved in conduction are identified, which are the two below  $E_F$  and the two above  $E_F$ . These peaks are fitted with Lorentzian functions whose parameters (location, width, height) are used to obtain EE-BESD parameters ( $E_i$ ,  $\gamma_i$ ,  $h_i$ ). It is not obvious that there are four well distinguished peaks and, some times, it is necessary to define an effective peak that approximately encloses the same area of the *QuantumATK* transmission spectrum, in the energy range where the peak is defined. The Lorentzian fit of the transmission spectrum must be done for each value of bias. The locations of the peaks, corresponding to  $E_i$  in EE-BESD, are obtained from the transmission spectrum at equilibrium. Then the peaks are shifted in energy thanks to  $U_{SCF}$  when a bias is applied.. On the other hand, the coupling with the contacts  $\gamma_i$  is obtained by the average over the bias points of the fitted width of the  $i$ -th peak. Instead,  $h_i$  is computed as described above where the variation of the height of a peak is analyzed through the Lorentzian fit. Next step is to insert the fitted parameters in EE-BESD, stored in an array of energy levels  $E_0 = [E_1, E_2, E_3, E_4]$  and of coupling constants  $\gamma = [\gamma_1, \gamma_2, \gamma_3, \gamma_4]$ , and verify that the calculated current is similar to the one obtained with *QuantumATK*.

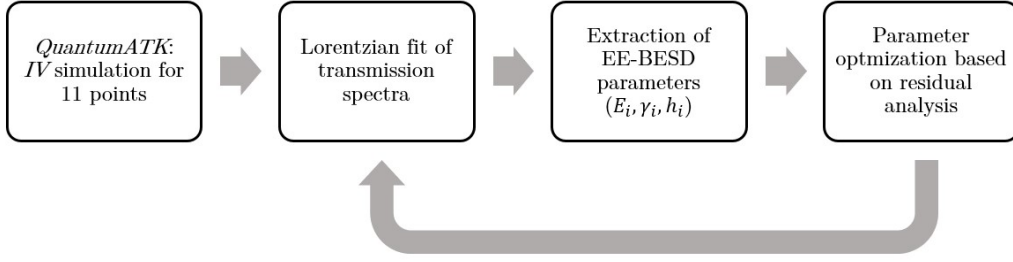


**Figure 3.2:** Flow chart of the fitting procedure adopted in this thesis.

The comparison can be done with a residual analysis, for example verifying that the maximum relative difference between the characteristics is less than a certain percentage for each bias point. If the result is not satisfying, the Lorentzian fit should be repeated until the area integrated under the transmission spectra is the most similar between EE-BESD and *QuantumATK*, hence optimizing the current computed with EE-BESD.

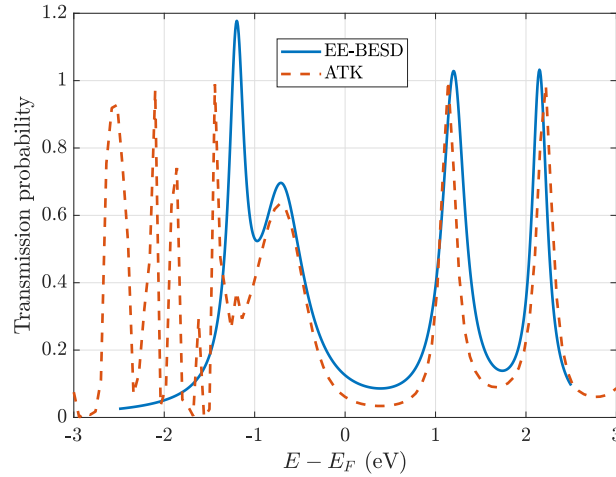


**Figure 3.3:** Comparison between the transmission spectra computed with EE-BESD and *QuantumATK* at equilibrium.

To make things clearer, an example taken from A. Zahir’s work is described here below. The molecular junction under study is based on 3TT, a molecule composed by three rings of thiophene, that is anchored to two gold contacts with a thiol group at both sides. Figure 3.3 shows the comparison between the transmission spectrum obtained with EE-BESD at equilibrium and the one computed by *QuantumATK*. The two spectra are well superposed, especially for the peaks above  $E - E_F > -1$  V. Instead, the first peak at  $E - E_F = -1.2$  eV seems to be completely uncorrelated

with the *ab-initio* spectrum. However, this is an effective peak that can reproduce a ‘correct’ fitting when a bias is applied, inducing a change in *QuantumATK* spectrum.

The effects of  $V_{DS}$  on the EE-BESD transmission spectrum are shown in fig. 3.4. It is evident that the peak associated to the HOMO level generally decreases in intensity when  $V_{DS}$  increases, even if there is a small increase when passing from  $V_{DS} = 2$  V to  $V_{DS} = 3$  V. Instead, the other peaks are not affected by the bias and would mostly contribute for larger  $V_{DS}$ . As already mentioned above, the same variation with bias would occur when  $V_{DS} < 0$  because the junction under study is symmetric.

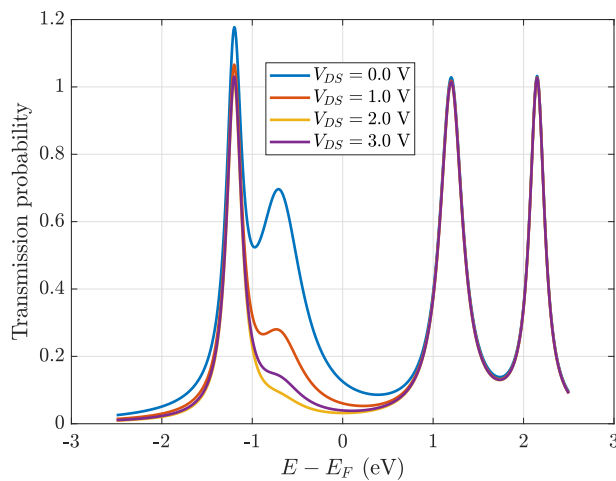


**Figure 3.4:** Variation of EE-BESD transmission spectrum by an applied  $V_{DS}$ .

The EE-BESD  $IV$  curve computed with the transmission spectra shown above is represented in fig. 3.5, where is compared to the *QuantumATK* result. It is astonishing how EE-BESD is able to reproduce very well the *ab-initio* result with a computational time that is infinitesimal with respect to *QuantumATK*. Comparing the areas under the  $IV$  curves, the percentage difference is only about 2.9%. Moreover, EE-BESD computes the current in less than a second considering hundreds of bias points. On the other hand, *QuantumATK* implements NEGF, coupled with an *ad-initio* electronic structure model (such as DFT or EHT), that is time consuming. For example, considering the case of 11 values of bias needed for the fitting procedure, a DFT-NEGF simulation needs about 2 days to finish considering a DZP basis set, a PBE-GGA exchange correlation functional and a  $7 \times 7$  grid of  $k$ -points. Furthermore, for the number of bias points used to plot fig. 3.5, thus 151, the simulation would take much more time to finish. This underlines the importance of EE-BESD as an efficient and effective tool for MolFET modeling.

One can think to implement PAT with EE-BESD in order to have an efficient

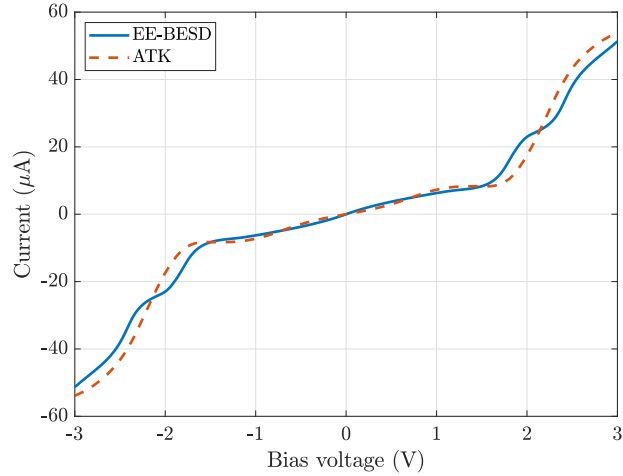


**Figure 3.5:** Comparison between the  $IV$  curves obtained with EE-BESD and *QuantumATK*.

tool to compute photocurrent. Indeed, Tien-Gordon is easy to implement since are involved only shifts of the transmission spectrum by  $n\hbar\omega$  and evaluations of Bessel's functions of first kind. This is straightforward to do in MATLAB<sup>®</sup> where the summation over  $n$  must be truncated up to a maximum order. For  $n_{max} = 5 - 6$  the summation already converges, but in any case the simulation is fast and taking at maximum dozens of seconds.

Things are more complex for Floquet model implementation since it involves the formalism of non-equilibrium Green's functions. In order to exploit the simplicity of 0D transport model, one should rewrite EE-BESD in the framework of NEGF theory. This means that the EE-BESD results should be obtained evaluating Green's functions and using them to compute the transmission spectrum. In the following section I will describe how this step can be done before implementing the Floquet algorithm presented by Stefanucci [55].

## 3.2 EE-BESD-NEGF

The first step to rewrite EE-BESD with the NEGF formalism, named EE-BESD-NEGF, is to convert vectors in matrices, as usually used in quantum mechanics. The array  $E_0$  storing the position of the peaks can be thought as the eigenvalues of an effective Hamiltonian that in the diagonalized form is expressed by

$$E_0 \Rightarrow H_{mol,0} = \begin{bmatrix} E_1 & 0 & 0 & 0 \\ 0 & E_2 & 0 & 0 \\ 0 & 0 & E_3 & 0 \\ 0 & 0 & 0 & E_4 \end{bmatrix} \quad (3.4)$$

Similarly, the array of coupling constants  $\gamma$  can be expressed with a diagonalized matrix where each entry of the diagonal corresponds to the coupling of a certain energy level:

$$\gamma \Rightarrow \Gamma = \begin{bmatrix} \gamma_1 & 0 & 0 & 0 \\ 0 & \gamma_2 & 0 & 0 \\ 0 & 0 & \gamma_3 & 0 \\ 0 & 0 & 0 & \gamma_4 \end{bmatrix} \quad (3.5)$$

The matrix  $\Gamma$  is the broadening matrix that is independent from energy. This means that each level  $E_i$  is coupled to any level of the contacts with constant  $\gamma_i$ . Considering energy independence and neglecting the renormalization of eigenvalues predicted by NEGF, the retarded contact self-energy can be expressed in the WBL as (see section 2.3)

$$\Sigma^R = -i\frac{\Gamma}{2} \quad (3.6)$$

The knowledge of the retarded contact self-energy allows to calculate the retarded Green's function evaluating the Dyson's equation:

$$G^R(E) = [EI - H_{mol,0} - \Sigma^R]^{-1} \quad (3.7)$$

It is important to understand that the energy dependence of  $G^R$  is obtained by solving the Dyson's equation for each value of  $E$  defined over an energy grid around  $E_F = 0$ . In EE-BESD the array of energy, called `Energy_span`, is defined with the MATLAB<sup>®</sup> built-in function `linspace` that defines a vector of points equally distant. The range that I have considered is between  $E_{min} = -2.5$  eV and  $E_{max} = 2.5$  eV with a total number of points equal to 5001. In EE-BESD we can consider a larger number of points in order to have a better energy resolution, that means a more precise evaluation of the energy integral of the transmission spectrum. On the other hand, if the algorithm is converted in the NEGF formalism, an inversion of a matrix with dimensions  $N_{levels} \times N_{levels}$  is involved for each value of energy and bias point, therefore is better to reduce the number of energy values to 5001, that is anyway sufficient to have a good resolution. Moreover, the energy value inside the Dyson's equation is multiplied by the identity matrix in order to obtain a diagonal matrix, having the same dimensions of  $H_{mol,0}$  and  $\Sigma^R$ , whose entries are all equal to the value  $E$  considered inside the energy loop.

After having computed  $G^R(E)$ , we can calculate the transmission spectrum using eq. 2.23:

$$T(E) = \text{Tr}[\Gamma_1 G^R(E) \Gamma_2 G^A(E)]$$

where  $\Gamma_{1,2} = \Gamma/2$  and  $G^A(E) = [G^R(E)]^\dagger$ . Knowing the transmission coefficient it is straightforward to compute steady-state current using Landauer formula.

In fig. 3.6 the EE-BESD-NEGF algorithm is graphically summarized. The outer light gray block represents the loop over bias voltages  $V_{DS}$  where the index `iv` goes

from 1 to nV, that is the total number of considered voltages. The applied  $V_{DS}$  varies at each iteration corresponding to the  $iv$ -th value of an array of voltages, in this figure called `Vds_array`. The bias determines the BW, but also the self-consistent potential  $U_{SCF}$  that is used to compute the shift of the energy levels due to charging effects. Then the updated levels are used to calculate  $H_{mol,0}$  and  $\Gamma$  which define the matrix that must be inverted to obtain  $G^R(E)$ . This is represented by the inner dark gray block where the transmission coefficient  $T(E)$  is computed by repeating the matrix inversion for each value of the grid `Energy_span` having dimension nE. Eventually, the current corresponding to the applied  $V_{DS}$  is evaluated using Landauer formula. The whole process is then repeated for each value of bias.

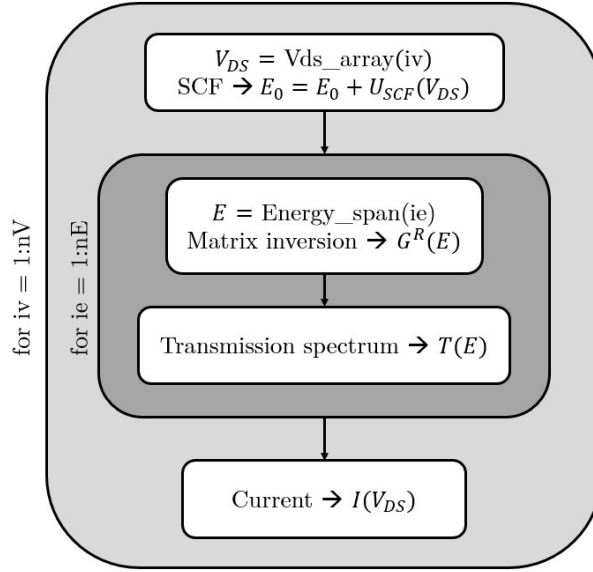


**Figure 3.6:** EE-BESD-NEGF flow chart. The outer light gray block corresponds to the  $V_{DS}$  loop necessary to evaluate the current for each value of bias. Instead, the inner dark gray block represents the energy loop used to evaluate the transmission probability for each value of the defined energy grid.

The results obtained with this procedure are shown in fig. 3.7 and 3.8. We can immediately observe that the transmission spectrum at  $V_{DS} = 1$  V obtained with EE-BESD-NEGF is different with respect to the one computed by EE-BESD. The peak corresponding to HOMO is much greater in EE-BESD-NEGF meaning that there is a problem with the fitting procedure. Indeed, the EE-BESD-NEGF spectrum is identical to the one obtained with the 0D transport model described in section 2.1. The reason is that the algorithm described above does not consider the fitting procedure needed to ‘map’ the *ab-initio* results into the ones of a simpler model. Therefore it is like considering an independent channels model, i.e. EE-BESD without the fitting procedure, where the coupling of each level correspond

to a Lorentzian in the transmission spectrum having amplitude equal to one. In fig. 3.7 the height of the peaks are greater than one because the Lorentzians are superposed and the tails of one channel add up to the peaks of the other channels.

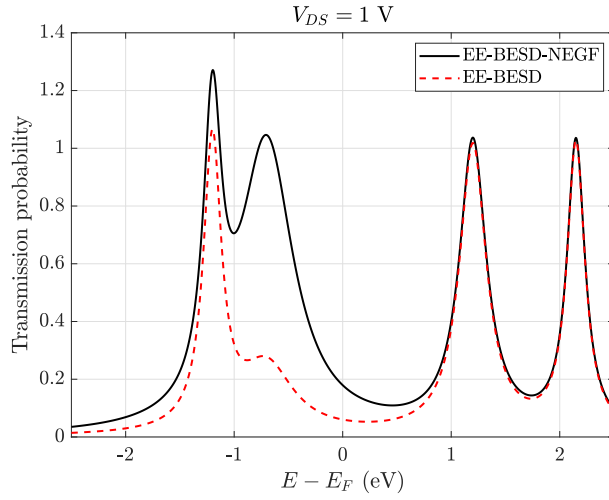


**Figure 3.7:** Comparison between transmission spectra computed with EE-BESD and with EE-BESD-NEGF which do not consider the fitting procedure.

As a consequence of the difference in the transmission probabilities, also the resulting  $IV$  curve would be different. In particular, the presence of a HOMO level that is highly transmissive increases remarkably the current for basically any value of  $V_{DS}$  as shown in fig. 3.8.

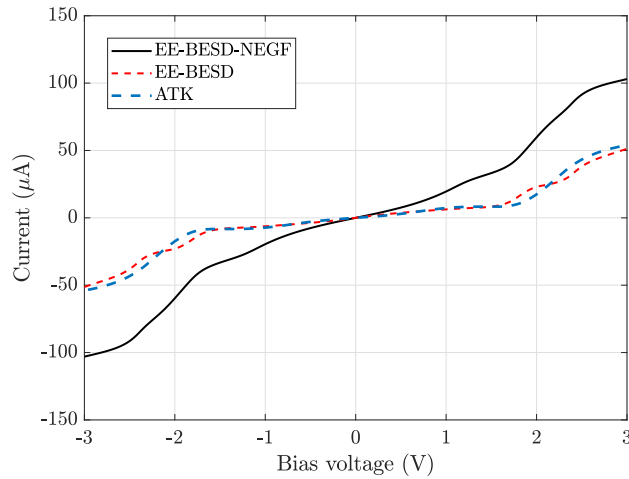


**Figure 3.8:**  $IV$  characteristics comparison between *QuantumATK*, EE-BESD and EE-BESD-NEGF.

We would like to retrieve the EE-BESD results, therefore now the question is: “How is it possible to include the fitting procedure in EE-BESD-NEGF?”. The problem is that we need Green’s functions that, when inserted in the formula for the evaluation of transmission, allow to obtain the same transmission of EE-BESD. Therefore we need a  $G^R(E)$  that includes the effects of the fitting. Nevertheless, in EE-BESD the function `applyVds` acts on the single Lorentzian peaks  $T_i$  of the transmission spectrum before they are added up. Instead, in EE-BESD-NEGF we compute the total transmission spectrum and `applyVds` cannot be directly applied. It is necessary a sort of transformation to obtain the EE-BESD spectrum starting from the one of EE-BESD-NEGF. This can be done with an energy dependent coefficient that is found with the following reasoning. First we define with  $T_{0D}$  the spectrum that does not consider the effects of polarization, thus the one implemented by the 0D model or by EE-BESD-NEGF algorithm described above. Considering four energy levels,  $T_{0D}$  is constituted by four terms

$$T_{0D}(E) = T_1(E) + T_2(E) + T_3(E) + T_4(E) \quad (3.8)$$

Starting from this equation, we can compute the EE-BESD spectrum applying the `applyVds` function obtaining

$$T_{pol}(E, V_{DS}) = h_1(V_{DS})T_1(E) + h_2(V_{DS})T_2(E) + h_3(V_{DS})T_3(E) + h_4(V_{DS})T_4(E) \quad (3.9)$$

where the subscript ‘pol’ stands for polarization and indicates that the effect is included in the transmission. Focusing on  $T_{0D}$ , we can transform it in  $T_{pol}$  imagining to multiplied the former by an energy and bias dependent coefficient  $h_{NEGF}(E, V_{DS})$ . Therefore we can compare the two expressions of  $T_{pol}$  to find  $h_{NEGF}(E, V_{DS})$ :

$$h_{NEGF}(E, V_{DS})T_{0D}(E) = T_{pol}(E, V_{DS}) \quad (3.10)$$

$$\Rightarrow h_{NEGF}(E, V_{DS}) = \frac{T_{pol}(E, V_{DS})}{T_{0D}(E)} \quad (3.11)$$

This coefficient can be efficiently computed using the EE-BESD algorithm since  $T_{0D}$  is the spectrum before using `applyVds`, whereas  $T_{pol}$  is its output. The computation is instant, hence can be included inside EE-BESD-NEGF. Knowing  $h_{NEGF}(E, V_{DS})$ , we can rewrite the transmission in the NEGF formalism as:

$$T(E) = h_{NEGF}(E, V_{DS}) \cdot \text{Tr}[\Gamma_1 G^R(E) \Gamma_2 G^A(E)] \quad (3.12)$$

The coefficient  $h_{NEGF}$  can be moved inside the trace without changing the result. Moreover it can be divided in two terms, identically equal to its square root, that respectively multiply  $G^R$  and  $G^A$ . This can be safely done because the coefficient

is real. The operation is reported in the equation below.

$$\Rightarrow T(E) = \text{Tr} \left[ \Gamma_1 \left( \sqrt{h_{NEGF}(E, V_{DS})} G^R(E) \right) \Gamma_2 \left( \sqrt{h_{NEGF}(E, V_{DS})} G^A(E) \right) \right] \quad (3.13)$$

It is clear that we can identify two new Green's functions that include the fitting procedure through  $h_{NEGF}$  and allow to obtain the EE-BESD transmission spectrum.

$$G^R(E, V_{DS}) = \sqrt{h_{NEGF}(E, V_{DS})} G^R(E) \quad (3.14)$$

$$G^A(E, V_{DS}) = \sqrt{h_{NEGF}(E, V_{DS})} G^A(E) \quad (3.15)$$

The transmission probability at  $V_{DS} = 1$  V computed with eq. 3.13 is shown in fig. 3.9. Now the peaks are identical to those predicted by EE-BESD, which means the mapping from one model to the other has been successful.

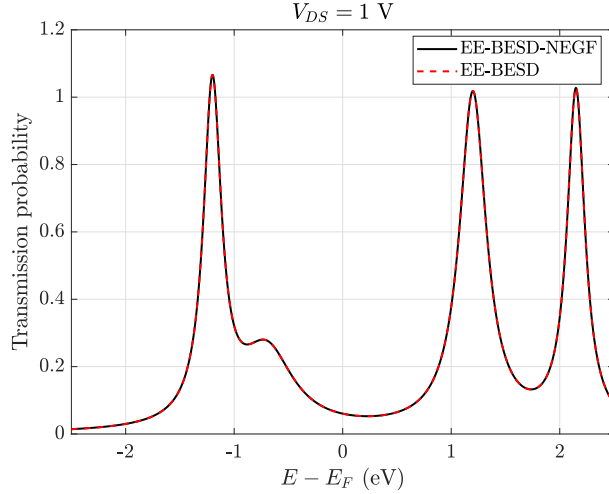


**Figure 3.9:** Comparison between EE-BESD and EE-BESD-NEGF transmission spectra when fitting procedure is included in both models.

Because of the perfect superposition between the transmission spectra, also the  $IV$  curves would be identical as shown in fig. 3.10. What significantly changes is the computational time that now is about 10 minutes for 601 bias points compared to EE-BESD simulations which take less than a second. Nevertheless, this computational time is not so bad compared to *ab-initio* simulations. I focused on EE-BESD-NEGF to implement Floquet model also because it is needed the knowledge of non-equilibrium Green's functions for the molecular system. The modified version of EE-BESD that implements TG and Floquet model is called EE-BESD-PAT and is described in the following section.

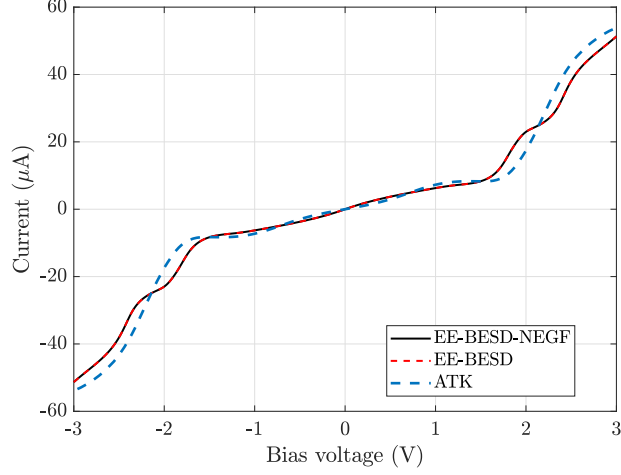


**Figure 3.10:**  $IV$  characteristics comparison between *QuantumATK*, EE-BESD and EE-BESD-NEGF when the fitting procedure is exploited to compute the Green's functions.

### 3.3 EE-BESD-PAT

Starting from EE-BESD and EE-BESD-NEGF I have implemented Tien-Gordon and Floquet model respectively. As already commented above, TG is easier to implement since it is just necessary to shift the transmission spectrum and truncate the summation up to a maximum order. For what concerns Floquet, the implemented algorithm is the one described by Stefanucci [55], presented in section 2.3, considering WBL for contact self-energy evaluation. The main difference in the algorithm is about the definition of zero-th Floquet mode

$$G_0(E, V_{DS}) = [g_0(E, V_{DS})^{-1} - \Sigma_{AC}^R(E)]^{-1} \quad (3.16)$$

where the non-interacting Green's function  $g_0(E) = g^{R(0)}(E)$  defined by Stefanucci is here evaluated as in EE-BESD-NEGF

$$g^{R(0)}(E, V_{DS}) = (EI - H_{mol,0} - \Sigma^R) \cdot \sqrt{h_{NEGF}(E, V_{DS})} \quad (3.17)$$

The 'mapping' coefficient  $h_{NEGF}$  is only used in this equation since the other Floquet modes are obtained through the recursive relation expressed in eq. 2.91. Also the continued matrix fraction is computed evaluating the matrices  $H_{\pm n}^{-1}(E)$  without employing  $h_{NEGF}$ . In this way all the information coming from the fitting procedure is encoded in  $g^{R(0)}(E, V_{DS})$  and then transmitted to the Floquet modes.

What remains is to understand how to define the amplitude  $V_{AC}$  of the oscillating potential used in TG and the amplitude  $U_{AC}$  of the time-dependent energy potential. The problem is that it is difficult to know *a priori* their values, as

extensively commented in section 2.2. However, it is possible to make some coarse approximation in order to have an idea of the photocurrent developed by the incident field. This will be discussed in the next paragraph together with the description of simulation parameters.

### 3.3.1 Simulation parameters

The parameters defined in EE-BESD-PAT can be divided in two classes. To the first class belong the electrical parameters, in particular those already used in EE-BESD such as an array of bias voltages  $V_{DS}$  and an array defining the energy grid. Instead, to the second class belong the optical parameters used to define the characteristics of the incident electromagnetic radiation. Similarly to what is done by *QuantumATK*, in EE-BESD-PAT is possible to choose the energy  $\hbar\omega$  and the flux  $F_{ph}$  of the incident photons. Starting from these variables we can compute the power per unit area simply multiplying the flux for the photon energy:  $P/A = F_{ph} \cdot \hbar\omega$ , where the notation  $P/A$  is used to indicate the surface power density. From classic electromagnetism it is known that the active power density considering plane waves is:

$$P/A = \frac{1}{2} \Re\left\{\frac{1}{Z}\right\} E_{AC}^2 = \frac{1}{2} \Re\{Y\} E_{AC}^2 \quad (3.18)$$

The quantity  $Y = 1/Z$  is the characteristic admittance of the medium through which the radiation propagates. In EE-BESD-PAT I have considered only the case of vacuum or air, therefore  $Y = \sqrt{\epsilon_0/\mu_0} = \epsilon_0 c$ , where  $c$  is the speed of light in vacuum. Knowing  $P/A$  we can compute the electric field amplitude of the incident field inverting eq. 3.18:

$$E_{AC} = \sqrt{\frac{2P/A}{\epsilon_0 c}} \quad (3.19)$$

With the electric field amplitude we can roughly estimate the potential drop along the gap. If the field is considered as uniform and the gap has a dimension equal to  $d_{mol}$ , that is the length of the molecule, for TG model the potential is estimated as:

$$V_{AC} = E_{AC} \cdot d_{mol} \quad (3.20)$$

This is of course a drastic approximation since the electric field is likely influenced by the electrostatic potential of the molecule and vice versa. Moreover, for the estimation we have considered a uniform electric field that does not agree with the potential profile of a symmetric single-molecule junction depicted in fig. 2.4. Nevertheless, J. K. Viljas and coworkers verified in [64] that, if we consider a linear ramp in the gap instead of a flat zero potential, the result of TG does not change significantly. Furthermore, in 2021 D. Kos *et al.* published an article [22] where

they estimated in the same way the 'optical' potential drop considering a NPoM geometry. This confirms the approach adopted for TG in the following. On the other hand, for Floquet the potential energy  $U_{AC}$  can be estimated with eq. 2.45 considering only the spatial dependence:

$$U_{AC} = -\vec{\mu}_{mol}(\vec{x}) \cdot \vec{E}_{AC}(\vec{x}) \quad (3.21)$$

Considering maximum coupling, i.e. the electric field having linear polarization aligned with the molecular electric dipole, the potential becomes:

$$U_{AC} = (-) \frac{\mu_{mol} \cdot E_{AC}}{e} \quad (3.22)$$

where the minus sign does not change the result of Floquet simulation and the elementary charge  $e$  is added to obtain  $U_{AC}$  in eV, that is the unit used to express  $H_{mol,0}$ . The *ab-initio* software *ORCA* can be used to optimize the geometry of the molecule but also to compute the molecular electric dipole of the isolated molecule. The dipole depends on the applied electric field, i.e. by the applied bias  $V_{DS}$ , and is influenced by the contacts. However, the latter dependence is neglected here in order to take things simpler. The components of the dipole computed by *ORCA* for a certain applied electric field is expressed in atomic units, while the magnitude is expressed in Debye. In the table below I reported the conversion between atomic units, Debye and SI.

atomic units (a.u.)	Debye (D)	SI (C·m)
1	2.541,765	$8.478,36 \times 10^{-30}$
0.393,427	1	$3.335,62 \times 10^{-30}$
$1.179,47 \times 10^{29}$	$2.997,94 \times 10^{29}$	1

**Table 3.1:** Units used to express the molecular electric dipole.

In the table above the values belonging to the same row are equivalent and can be used to pass from one unit to another. It is relevant to observe that isolated molecules have an electric dipole that is generally lower than 10 D. For example, considering an input electric field for *ORCA* simulation of  $1 \times 10^{-3}$  a.u. =  $5.142,206 \times 10^8$  Vm<sup>-1</sup>, that is basically equivalent to applying a  $V_{DS} = 1$  V on a 2 nm gap, a conjugated molecule like 3TT develops an electric dipole with magnitude equal to 1.995,043,745,7 D whereas a saturated molecule like C8 develops a dipole with magnitude equal to 0.005,705,724,4 D. Of course the magnitude of the dipole is greater for conjugated molecule thanks to the electronic cloud delocalized along the molecule. Nevertheless, considering this order of magnitude ( $\approx 1$  D), to obtain a reasonable value of  $U_{AC} \approx 0.1 - 10$  eV we would need an electric field  $E_{AC} \approx 10^9 - 10^{11}$  V/m that is much larger than the critical field  $E_c = 10^6$  V/m

that produces the electrical breakdown of the medium. To understand better the problem, I will show an example taking as reference the 3TT molecule. Starting from the value of  $U_{AC}$  and  $eV_{AC}$  ( $V_{AC}$  is multiplied by  $e$  in order to express it in eV, but the value remains the same) we can compute the value of the corresponding incident field, power and photon flux. I have chosen as photon energy  $\hbar\omega = 1$  and I have initially neglected the possible field enhancement due to LSP resonance (enhancement factor equal to one). Under these assumptions, the incident field required to obtain  $U_{AC}$  and  $eV_{AC}$  in the range  $[0,10]$  eV is computed inverting eq. 3.20 and 3.22. The results are shown in fig. 3.11 where a semi-logarithmic scale is adopted. It is immediately clear that the field required to obtain  $U_{AC}$  is much greater than the one necessary to obtain the same value of  $eV_{AC}$ .  $E_{AC}(U_{AC})$  is about one order and a half greater than  $E_{AC}(eV_{AC})$ . However, both curves are above the critical field ( $E_c$ ) therefore, imagining a laser irradiating the system, the field would ionize air before reaching the junction, which is a problem for practical applications. Moreover, the corresponding power density and photon flux, shown in fig. 3.12, are too high for typical lasers which have often power densities in the range  $10^6 - 10^9$  W/m<sup>2</sup>.

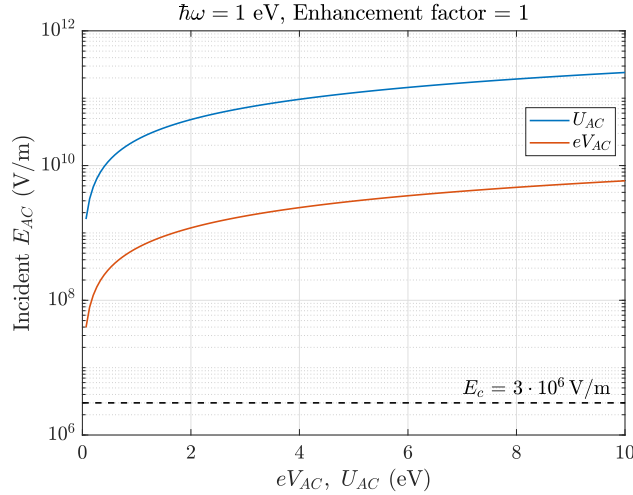


**Figure 3.11:** Incident electric fields required to have a fixed value of  $U_{AC}$  and  $eV_{AC}$ .

The situation changes when the plasmonic response is considered in the computation of the field. In this case the parameters of the models are computed in the following way:

$$V_{AC} = E_{AC} \cdot k_{enh} \cdot d_{mol} \quad (3.23)$$

$$U_{AC} = (-) \frac{\mu_{mol} \cdot E_{AC}}{e} \cdot k_{enh} \quad (3.24)$$

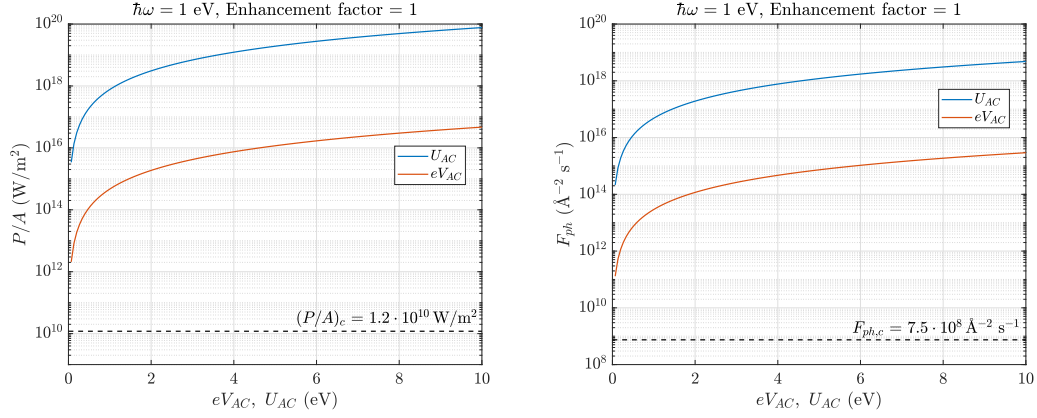


**Figure 3.12:** Power density and photon flux required to have a fixed value of  $U_{AC}$  and  $eV_{AC}$ .

The coefficient  $k_{enh}$  corresponds to the electric field enhancement and depends on the frequency of the incident radiation. In this thesis I have considered the enhancement simply as a scalar value, although it has a vectorial character and should be computed in each point of space. The product  $E_{AC} \cdot k_{enh}$  corresponds to a rough approximation of the ‘local’ electric field, that is the one that determines  $U_{AC}$  and  $eV_{AC}$ . Considering an enhancement equal to  $k_{enh} = 500$  at the chosen photon energy, the required ‘local’ electric field to have a certain value of  $U_{AC}$  and  $eV_{AC}$  would be the same of fig. 3.11, but the incident one would be lower thanks to enhancement. The results are shown in fig. 3.13. The difference between

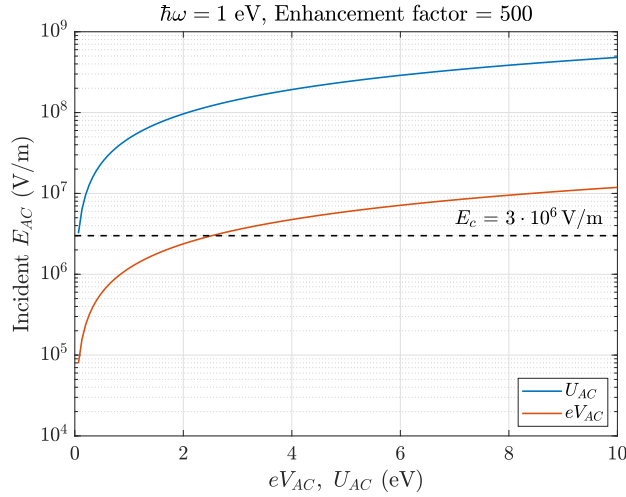


**Figure 3.13:** Incident electric fields required to have a fixed value of  $U_{AC}$  and  $eV_{AC}$  when field enhancement is considered.

the two curves remains the same, but in this case there are some values of  $eV_{AC}$  that allow to have  $E_{AC} < E_c$  and avoid electrical breakdown. On the other hand, considering the more physical model of coupling between molecule and field, i.e. the expression for  $U_{AC}$ , it does not allow to have values of the field smaller than the critical one. For this reason in EE-BESD-PAT simulations I have posed  $U_{AC} = eV_{AC} = E_{AC} \cdot k_{enh} \cdot d_{mol}$ , that means I have considered the same parameter for TG and Floquet simulation.

In light of this, the enhancement factor would be another optical input parameter of the simulation chosen by the user. Future works could be focused on the computation of  $k_{enh}$  starting from the junction geometry in order to have a more realistic guess of field enhancement. Figure 3.14 graphically summarizes the optical parameters and how they are related to each other to obtain  $U_{AC}$  and  $eV_{AC}$ .

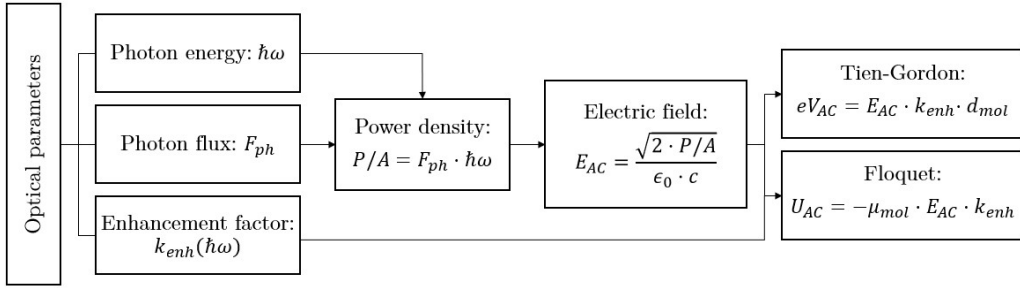


**Figure 3.14:** Summary of the optical parameters and of their relations needed to compute  $U_{AC}$  and  $eV_{AC}$ .

Before presenting an example of EE-BESD-PAT simulation, it is important to make an observation concerning possible ionization of the molecule inside the gap. Indeed the photon energy can be large enough to extract an electron from the highest occupied molecular orbital, i.e. from the HOMO, producing the ionization of the molecule. The energy difference between the vacuum level and the HOMO level is equal to the binding energy  $E_b$  of an electron in the HOMO. Considering the 3TT junction as an example, the binding energy can be read from the molecular energy spectrum computed with *QuantumATK*, that is the projection of the Hamiltonian over the device region. The levels of the molecule can be computed with respect to vacuum level. In this case the energy corresponding to HOMO is equal to the binding energy. For 3TT we have  $E_b = -3.303,403$  eV, that means an absorption of a photon with energy  $\hbar\omega \approx 3.31$  eV from an electron in HOMO would produce the ionization of the molecule. Therefore photons with energy larger than this value would significantly change the conduction properties of the molecule. In addition to this process, if the power density is sufficiently high, the energy transferred to the molecule could also modify the junction geometry. In the case of 3TT, the thiophene rings could be broken, hence destroying the junction. A rough estimation

of the energy necessary to divide 3TT in two parts, a 1TT (single thiophene ring) and a 2TT (two thiophene rings), can be done computing the total energy of the molecules. In particular, the total energy of 3TT is lower than the sum of the total energy of 1TT and 2TT (otherwise the molecule would not exist). The binding energy is then estimated as:

$$E_b = E_{tot}(1TT) + E_{tot}(2TT) - E_{tot}(3TT) \quad (3.25)$$

Using *ORCA* it is possible to compute the total energy of the optimize geometry. Considering the DFT functional CAM-B3LYP, I have obtained the following total energies:

Molecule	Total energy	
1TT	-552.936 H	-15,046.144 eV
2TT	-1,104.826 H	-30,063.838 eV
3TT	-1,656.646 H	-45,079.638 eV

**Table 3.2:** Total energy of 1TT, 2TT and 3TT expressed in Hartree (H) and in eV

Inserting these values in eq. 3.25 we obtain  $E_b = -30.343$  eV. As done above, we can approximately consider the potential energy transferred to the junction as  $U_{AC} = E_{AC} \cdot k_{enh} \cdot d_{mol}$ . If  $U_{AC} = |E_b|$  we can imagine that the incident radiation can likely generate the breaking of the molecule. The corresponding ‘local’ field is  $\approx 1.8 \times 10^{10}$  V/m. This can be considered as an ‘ionization’ threshold on the enhanced electric field that should not be overcome. Generally, if the enhancement factor is not too high, incident fields smaller than  $E_c$  are not so much amplified to become greater than the ionization threshold. Nevertheless, it becomes possible for high field amplification and this effect should be taken into account.

In the next section I will present an example of EE-BESD-PAT simulations for a 3TT junction. The parameters described above can be combined in order to do different simulations. In particular three simulations can be chosen in the MATLAB<sup>®</sup> ‘main’ file and are indicated with the following strings:

- **Vds\_cycle.** This simulation allows to compute the *IV* curve under illumination, therefore it is defined an array of  $V_{DS}$  and some values for the photon energy  $\hbar\omega$  and the photon flux  $F_{ph}$ .
- **hw\_cycle.** The total current is computed considering an array of photon energies and some values of the photon flux and of the applied bias. The corresponding figure of merit is the current plotted with respect to  $\hbar\omega$ .
- **Uac\_cycle.** In this simulation an array of photon fluxes is defined to compute the corresponding current considering some values of photon energy and of

bias. The figure of merit corresponds to the current plotted with respect to flux variation.

### 3.3.2 Example: illuminated 3TT junction

In this section I will show and comment the results of the simulations taking as example a symmetric single-molecule junction based on 3TT bonded to two gold contacts through thiol groups. The length of the molecule used to estimate  $U_{AC}$  and  $eV_{AC}$  is  $d_{mol} = 1.683,9$  nm, that is measured from the builder tool of *QuantumATK*. This molecule has been chosen because is familiar and was already implemented in EE-BESD. The transmission peaks at equilibrium are located at energies values identified by the array  $E_0 = [-0.7, -1.2, 1.2, 2.15]$  eV that is extracted by the fitting procedure. In TG and Floquet there is the summation over index  $n$  that has been truncated at  $n_{max} = 16$ , for both models, to obtain the results shown below. Hence the summation goes from  $-n_{max}$  to  $n_{max}$ , thus it considers 33 terms. This considerably large number of terms is especially necessary for Floquet model to reach convergence when  $U_{AC}$  increases, that is the case of `Uac_cycle` simulation. In order to make a fair comparison between the execution times, I have considered the same maximum number of terms included in the summation for all types of simulation.

First of all I have computed the  $IV$  curve under illumination. The parameters used in the simulation are the following:

- $E$ : energy grid equal to an array of 5001 values between  $-2.5$  eV and  $2.5$  eV (equal for all the simulations).
- $V_{DS}$ : array of 76 values in the range from 0 to  $1.5$  V. Only positive voltages are considered since the junction is symmetric under inversion of bias.
- $\hbar\omega$ : array of two values corresponding to  $0.5$  eV and  $1$  eV.
- $F_{ph}$ : array of three values equal to  $0$ ,  $1 \times 10^8 \text{ \AA}^{-2}\text{s}^{-1}$  and  $1 \times 10^9 \text{ \AA}^{-2}\text{s}^{-1}$ .
- $k_{enh}$ : fixed to 500.

Note that the enhancement factor has been chosen arbitrary and fixed equal to both values of photon energy. This is not properly correct since the localized plasmon response should vary with the wavelength of the incident radiation. Nevertheless, this is just an example that has the goal to show how the results of the simulator should be analyzed, hence I will not take in consideration this difference. I considered  $k_{enh} = 500$  to have reasonable values of the incident field that do not produce electrical breakdown. However the results would be the same with  $k_{enh} = 1$  and considering higher fluxes. On the other hand, when comparing the results

of the simulator with real experimental measurements, we must pay attention to choose correctly the parameters, as it will be done below for the validation of the simulator.

The execution time of TG is 7 s, that means the model is low computational demanding. The TG simulation could be faster because the summation over  $n$  basically converges with  $n_{max} = 5$ . However, the execution time is so short that is possible to increase the number of terms without paying too much attention. The execution time for a single combination  $(V_{DS}, \hbar\omega, F_{ph})$  of the parameters is  $\approx 0.015$  s. This allows to choose more values of the parameters for a single TG simulation, for example increasing the resolution of the  $IV$  characteristics. On the other hand, Floquet simulation is much more time consuming. Nevertheless, the execution time are far shorter than the one of *ab-initio* simulations. For this case the execution time is equal to 1,873.45 s corresponding to 31.22 minutes. If the value of  $U_{AC}$  is not too high, it is possible to reduce the total computational time reducing the number of considered Floquet modes. However, the result with 33 modes  $(2n_{max} + 1)$  is still reasonably fast since the execution time for a combination  $(V_{DS}, \hbar\omega, F_{ph})$  is  $\approx 4.11$  s.

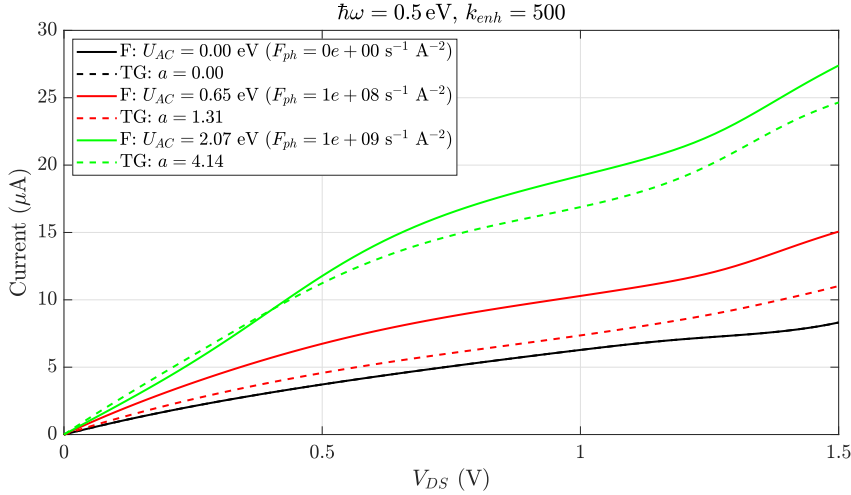


**Figure 3.15:**  $IV$  curves of 3TT junction illuminated by different fluxes of photons having energy  $\hbar\omega = 0.5$  eV.

In fig. 3.15 are shown the  $IV$  curves for different fluxes considering  $\hbar\omega = 0.5$  eV. Curves with the same color corresponds to the same flux, whose corresponding value of  $U_{AC}$  and  $\alpha = eV_{AC}/\hbar\omega$  is shown in the legend (in MATLAB<sup>®</sup> I used the letter  $a \equiv \alpha$  for practical reason). The solid and dashed black curves, corresponding to a null flux, are coincident. This is coherent because no photons are incident on the junction and therefore the result of the two models should be the same and equal to the  $IV$  characteristic predicted by EE-BESD. On the other hand, the red curves

corresponding to a flux equal to  $1 \times 10^8 \text{ \AA}^{-2} \text{ s}^{-1}$  include the photocurrent induced by the incident radiation. In particular, for this photon energy and flux, the total current predicted by Floquet is greater than the one computed with TG for any value of bias. Things are a bit different when the flux is changed to  $1 \times 10^9 \text{ \AA}^{-2} \text{ s}^{-1}$ . Indeed the difference between TG and Floquet currents is smaller. Moreover, for low bias up to  $V_{DS} = 0.4 \text{ V}$ , the TG current is slightly greater than the one of Floquet. This suggests that the difference between the currents computed with the two models is not obvious, but depends on the simulation parameters that determine the value of  $U_{AC}$  and  $\alpha$ , with a greater weight associated to the photon flux. For example, if we change the photon energy to  $\hbar\omega = 1 \text{ eV}$ , the current changes as shown in fig. 3.16. In this case, the TG current in dashed green, corresponding to a flux equal to  $1 \times 10^9 \text{ \AA}^{-2} \text{ s}^{-1}$ , is greater than the solid green curve predicted by Floquet. It is relevant to observe that also the shape of the current changes considerably with respect to the previous case, getting away from the shape of the curve predicted by EE-BESD. This seems to be true especially for large fluxes as in the case of the dashed green curve in this range of  $V_{DS}$ . In order to understand

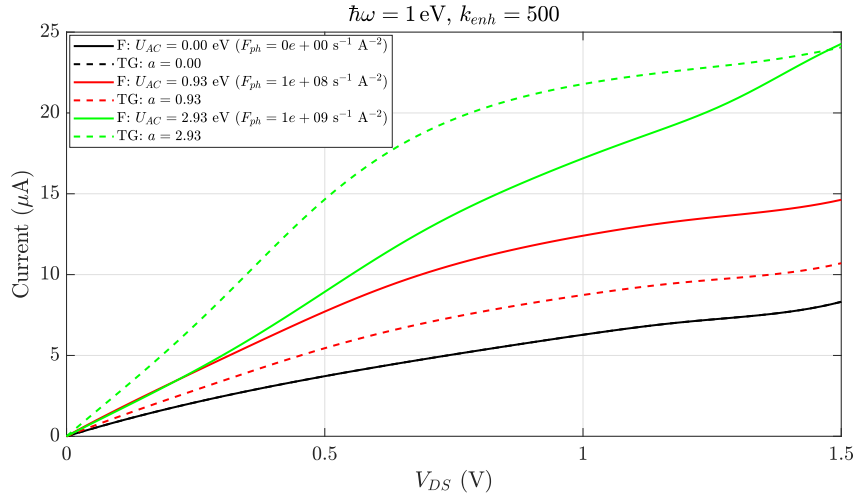


**Figure 3.16:**  $IV$  curves of 3TT junction illuminated by different fluxes of photons having energy  $\hbar\omega = 1 \text{ eV}$ .

better the behavior of the illuminated  $IV$  characteristic, it is important to look at the ‘optical’ transmission spectrum that can be computed for symmetric junction following eq. 2.95. The spectra for  $\hbar\omega = 0.5 \text{ eV}$  and  $\hbar\omega = 1 \text{ eV}$  with  $V_{DS} = 0.4 \text{ V}$  are shown in fig. 3.17 and 3.18. Again the dashed and solid black spectra are superposed since they refer to dark condition and the transmission spectrum is equal to the one computed by EE-BESD. Increasing the photon flux produces additional peaks, the so called sidebands, at a distance  $n\hbar\omega$  from the main peaks due to absorption or emission of  $n$  photons. The light-blue rectangle represents the

BW defined by the source and drain Fermi levels. The integration of the spectrum inside this area is proportional to the total current. It is clear that the ‘optical’ transmission spectrum takes larger value in this energy range, therefore the current increases as commented above. Focusing on the flux  $F_{ph} = 1 \times 10^9 \text{ \AA}^{-2} \text{ s}^{-1}$ , it is not immediate to understand that the integration inside the BW of the dashed and solid green curves for  $\hbar\omega = 0.5 \text{ eV}$  corresponds to basically the same current as shown in fig. 3.15. On the other hand, if we consider the case for  $\hbar\omega = 1 \text{ eV}$ , it is

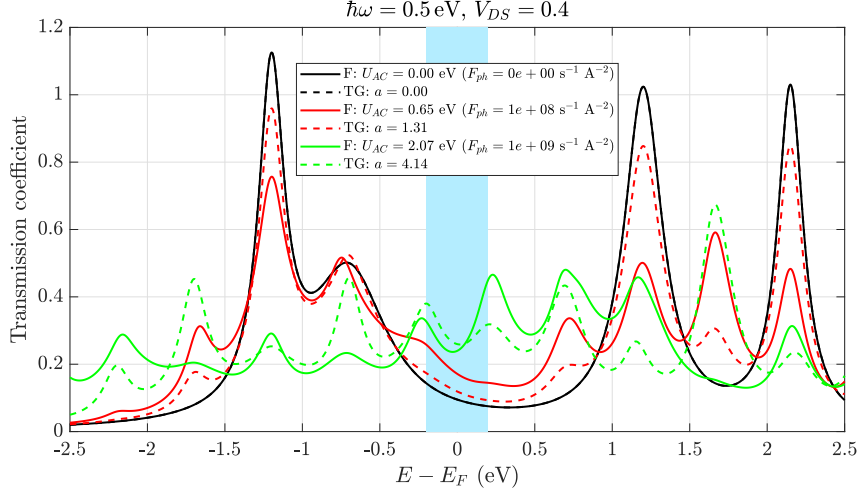


**Figure 3.17:** Transmission spectra of illuminated 3TT junction when the flux is varied considering  $\hbar\omega = 0.5 \text{ eV}$  and  $V_{DS} = 0.4 \text{ V}$ . The light-blue rectangle represents the BW defined by the applied bias.

clear that the area under the green dashed curve is greater than the solid green one. Indeed, in fig. 3.16 is easy to see that the TG current is greater than the one predicted by Floquet for the applied bias  $V_{DS} = 0.4 \text{ V}$ . Although it is not difficult to identify the main peaks and the corresponding sidebands, it is important to know in detail the dependence of the location and intensity of the peaks on the optical parameters. Something has been already said, but we can add information by analyzing the following two simulations: `hw_cycle` and `Uac_cycle`.

As already said, the simulation `hw_cycle` concerns the computation of the current flowing through the illuminated junction depending on the incident photon energy. I have considered the following parameters:

- $V_{DS}$ : array of 5 values in the range from 0 to 1 V equally distant 0.2 V to each other.
- $\hbar\omega$ : array of 84 values in the range from 0 to 2.5 eV.
- $F_{ph}$ : one value of photon flux equal to  $1 \times 10^8 \text{ \AA}^{-2} \text{ s}^{-1}$ .

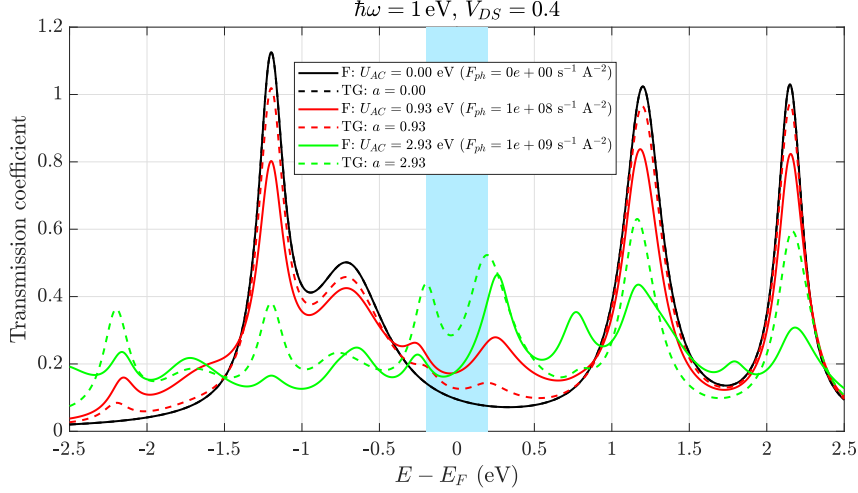


**Figure 3.18:** Transmission spectra of illuminated 3TT junction when the flux is varied considering  $\hbar\omega = 1$  eV and  $V_{DS} = 0.4$  V. The light-blue rectangle represents the BW defined by the applied bias.

- $k_{enh}$ : fixed to 500 for each photon energy.

The TG simulation took 2.54 s to finish while Floquet execution time was 1,214.19 s. The former corresponds to an execution time per combination ( $V_{DS}, \hbar\omega, F_{ph}$ ) that is  $\approx 0.006$  s, while for the latter the time per combination is  $\approx 2.89$  s. These times per combination are slightly shorter than the ones of the previous simulation but still well comparable. In fig. 3.19 is shown the current at different  $V_{DS}$  depending on the photon energy. One should expect that the current for  $\hbar\omega = 0$  eV is equivalent to the EE-BESD result. Indeed it is the case for Floquet current that converges to the dark case. Instead the current predicted by TG for  $\hbar\omega = 0$  eV is equal to zero for all values of bias (this limiting case is highlighted with an orange rectangle in fig. 3.19). This is of course wrong and represents a limitation of TG that originates from the way the model is defined. The argument of the Bessel's functions  $\alpha$  is inversely proportional to the photon energy, hence if  $\hbar\omega \rightarrow 0$  we would have  $\alpha \rightarrow \infty$ . Since Bessel's functions decrease with  $\alpha$ , all the peaks of the transmission spectrum would be weighed with very small values, thus the transmission assumes very low values (see fig. 3.21(a)) corresponding to a negligible current with respect to the dark one. Even if we must be aware of this problem concerning TG, it is not so problematic since is unusual to consider very small values of photon energy close to 0 eV.

Regarding the rest of fig. 3.19, we can see that for this photon flux the current predicted by Floquet is greater than the one computed with TG for all values of photon energy. Moreover, for smaller values of bias, there are three visible peaks at photon energies equal to 0.66 eV, 1.14 eV and 2.16 eV whereas, increasing  $V_{DS}$ , the

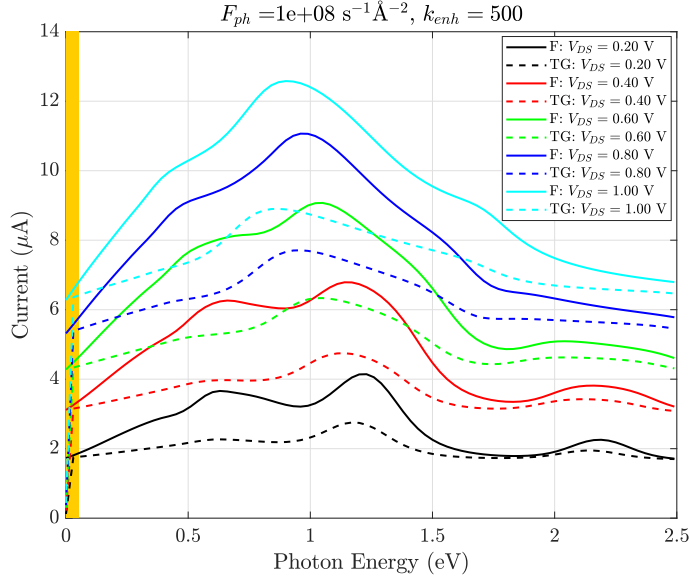


**Figure 3.19:** Current computed with TG and Floquet varying the photon energy for different values of bias. The rectangle in orange highlights the region close to  $\hbar\omega = 0$  eV where the TG model shows a limitation.

spectrum of the current becomes more broadened. To understand if these peaks are related to the electronic structure of the molecule it is necessary to analyze how the transmission spectrum changes with  $\hbar\omega$ . Fig. 3.20 shows four transmission spectra computed at  $V_{DS} = 0.4$  V for different consecutive values of photon energy. Panel (a) is basically the transmission spectrum plotted in red in fig. 3.17. We can observe that for this photon flux only side peaks referred to  $n = \pm 1$  are visible and are located at the same positions both for TG and Floquet. It is interesting to observe that the sideband at  $\approx 1.7$  eV is greater than the others because corresponding to the superposition of two additional peaks coming from the absorption of a photon by electrons at  $E = 1.2$  eV and from the emission of a photon by electrons at  $E = 2.15$  eV. Increasing  $\hbar\omega$ , that means moving from panel (a) to (d), the position of the additional peaks moves along the energy axis. A clear example is the peak at the left hand side of HOMO-1 peak that shifts towards lower photon energies until is no more visible (see panel (d)). For certain values of  $\hbar\omega$ , side peaks can be inside the BW (superposed or not), as in panel (b), producing an increment in the current that can correspond to a peak in the  $I(\hbar\omega)$  plot. In fig. 3.21 I reported the transmission spectra for  $V_{DS} = 0.4$  V corresponding to the photon energies for which there is a peak in the current (except for panel (a) that corresponds to a value of  $\hbar\omega$  close to zero). In these cases the area under the spectrum inside the BW reaches a local maximum, which corresponds to the inclusion of a side peak.

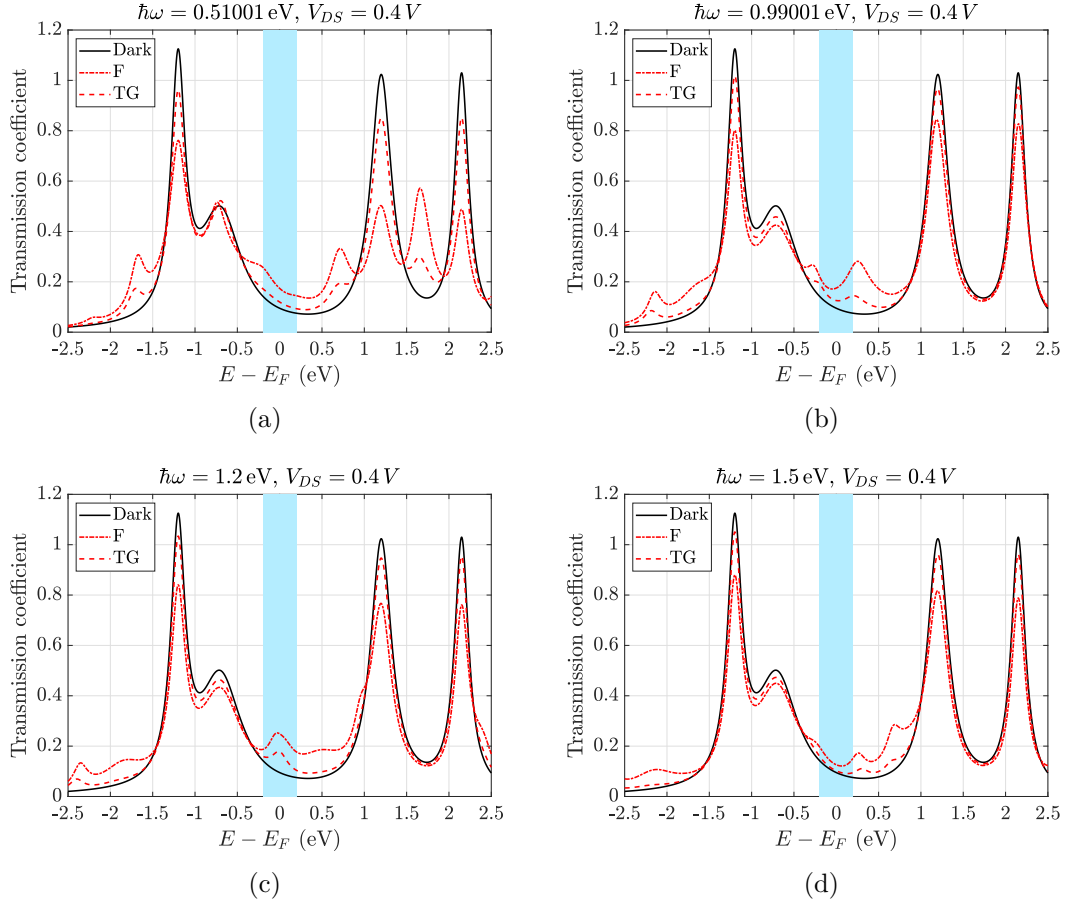


**Figure 3.20:** Transmission spectra for  $V_{DS} = 0.4$  V considering different photon energies. In light-blue is highlighted BW corresponding to  $V_{DS}$ .

It is important to observe that the intensity of the sidebands is greater for not too high value of  $\hbar\omega$ , whereas the ‘dark’ peaks are normalized to a smaller value. In TG this can be understood thinking that the dark peaks are proportional to  $J_0^2(eV_{AC}/2\hbar\omega)$ , while the sidebands to  $J_n^2(eV_{AC}/2\hbar\omega)$  with  $n \neq 0$ . The former are reduced since  $J_0^2(eV_{AC}/2\hbar\omega) = 1$  only for  $\alpha = 0$ , while the latter have a smaller intensity when increasing  $\hbar\omega$  because  $\alpha$  decreases and the  $J_n(\alpha/2)$  tend to values close to zero. Coherently, Floquet predicts the same behavior but with a different value of the peaks. The decrease with  $\hbar\omega$  in Floquet can be justified thinking about the time-dependent Hamiltonian. Indeed the energy levels can be thought as oscillating in time due to the addition of a sinusoidal potential  $U_{AC}(t)$ . If the frequency  $\omega \gg \gamma/\hbar = 1/\tau$ , it means that the levels are oscillating too fast to allow electrons to escape towards the contacts. The average over one period is equivalent to consider the levels still in their position, hence we would have a

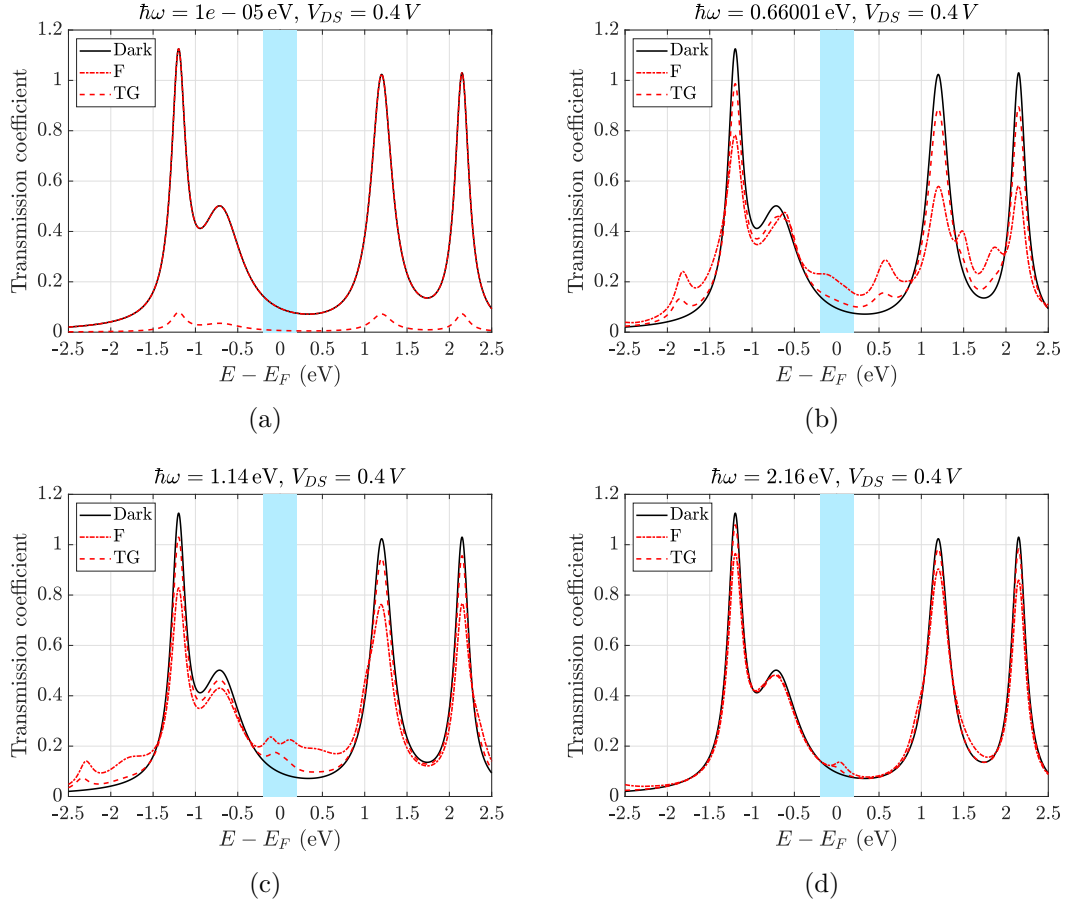


**Figure 3.21:** Transmission spectra for  $V_{DS} = 0.4$  V. Panel (a) is related to the special case  $\hbar\omega = 0$  eV for which TG shows some limitations. Instead panels (b), (c) and (d) are referred to transmission spectra corresponding to current peaks clearly evident in fig. 3.19. In light-blue is highlighted BW corresponding to  $V_{DS}$ .

flow corresponding to the dark current, but other contributions coming from the oscillation are vanished. Of course this is a simplified justification, but it is useful for having a concrete knowledge of what happens.

What just said explains why there are peaks in  $I(\hbar\omega)$ , but do not justify explicitly the reason why the photocurrent increases with  $V_{DS}$ , as shown in fig. 3.22, and why the spectrum seems to change shape. First of all, we must say that the three peaks are always present in the curves, but at large voltages are less evident. Moreover they shift towards lower photon energies. This behavior can be justified by the fact that the BW increases, therefore side peaks can enter into it considering smaller photon energies with respect to low bias condition. Furthermore, as said above, the intensity of the sidebands are larger for not too high values of  $\hbar\omega$ , looking at

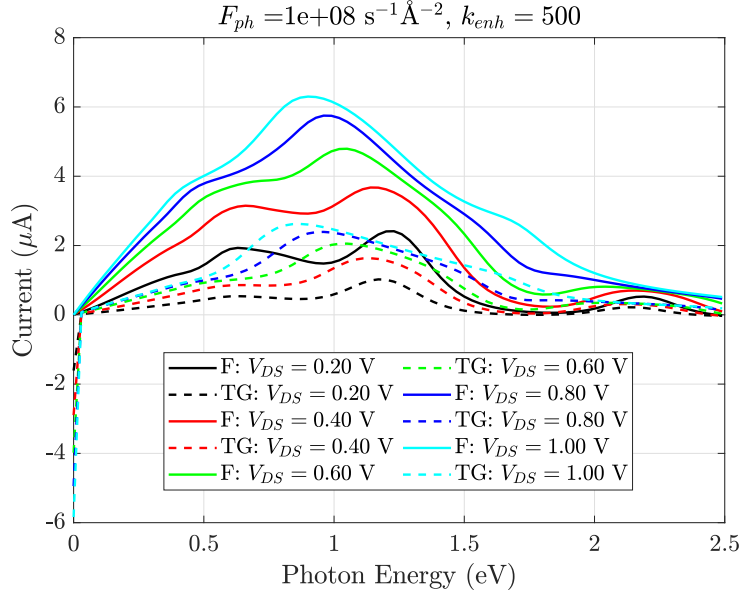


**Figure 3.22:** Photocurrent of the irradiated 3TT junction computed with TG and Floquet for different values of bias.

fig. 3.20 we could say up to 1 eV. Therefore, since for large voltages these peaks are included in the BW, it means that the resulting photocurrent would be larger having a maximum corresponding to the photon energy for which the sidebands have the largest value.

The position of the peaks depend also on charging effects embedded in the potential  $U_{SCF}$ . The transmission spectrum in dark condition is shifted by  $U_{SCF}$ , therefore determining the position of the dark peaks. As a consequence, also the sidebands would be in different position, hence varying their entrance inside the BW. The importance of this effect basically depends on the value of  $U_{SCF}$ . In this example, for the considered voltages, this effect does not play an important role.

What remains to understand is how the current is influenced by the incident photon flux. This analysis is done through the third type of simulation corresponding in MATLAB<sup>®</sup> to string `Uac_cycle`. The parameters chosen for the simulation are the following:

- $V_{DS}$ : array of 5 values in the range from 0 to 1 V equally distant 0.2 V to each other.
- $\hbar\omega$ : one value of photon energy equal to 0.5 eV.
- $F_{ph}$ : array of 251 photon fluxes in the range from  $1 \times 10^6 \text{ \AA}^{-2} \text{ s}^{-1}$  to  $1 \times 10^{11} \text{ \AA}^{-2} \text{ s}^{-1}$ .
- $k_{enh}$ : fixed to 500 for each photon flux.

The total execution time in this case is 20.92 s for TG and 4,353.84 s (72.56 minutes) for Floquet, that are much longer than the previous simulations because of the greater number of points for  $F_{ph}$ . Nevertheless, the time required for each combination ( $V_{DS}, \hbar\omega, F_{ph}$ ) is of  $\approx 0.017$  s for TG and of  $\approx 3.47$  s for Floquet, which are in the same order of magnitude of those reported above.

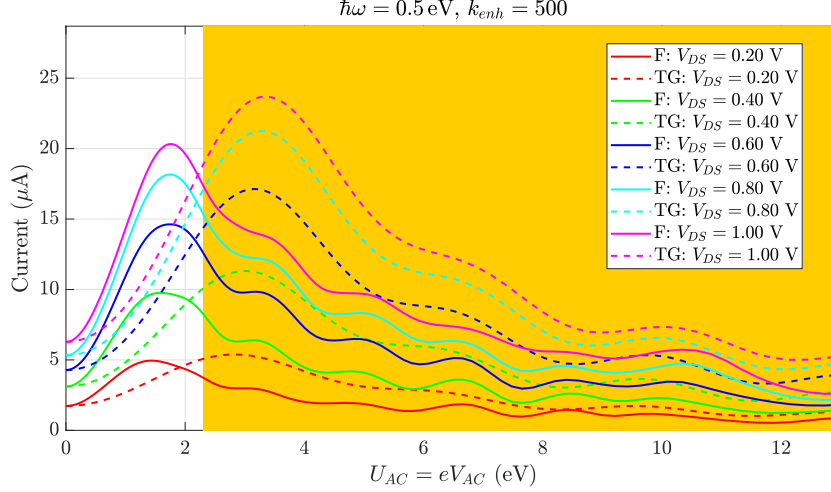


**Figure 3.23:** Simulated current of illuminated 3TT junction using TG and Floquet when the incident photon flux is varied. The region highlighted by the orange rectangle corresponds to incident electric fields that induce the electrical breakdown of air.

The computed current is plotted with respect to the parameter  $U_{AC} = eV_{AC}$  that varies with the incident photon flux. The results for different  $V_{DS}$  are shown in fig. 3.23. It is evident that the general behavior for the two model is similar since the current reaches a maximum at a certain value of  $U_{AC}(eV_{AC})$  and then decreases with an oscillatory behavior. The value of the maximum is greater when  $V_{DS}$  increases, coherently to what said above, with the one predicted by TG greater than the one computed with Floquet. It is interesting to notice that the position of the maximum is different for TG with respect to Floquet, with the former at greater value of  $U_{AC}(eV_{AC})$  with respect to the latter, but in both cases it does not shift too much when the bias is changed. Moreover, all the TG maxima are inside the orange area that corresponds to  $U_{AC}(eV_{AC})$  values related to incident fields greater than  $E_c$ . We should pay attention when considering the values of the current in this region since it is very likely that sparks injected in air can drastically change the conduction properties of the junction. For this reason, the values of the current computed in this region are not reliable.

Focusing on values of  $U_{AC} < 2.3 \text{ eV}$  (thus the threshold for electrical breakdown), the current predicted by Floquet is greater than the one of TG almost for every values of the potential amplitude, whereas in the orange area it is true the opposite.

Furthermore, close to zero, i.e. for values of the photon flux  $\approx 10^6 - 10^7 \text{ \AA}^{-2} \text{ s}^{-1}$ , the current seems to respect a power law with respect to  $U_{AC}$  until it reaches values close to the global maximum. To understand the reason why the current decreases at a certain point with  $U_{AC}$ , we can first think at the TG case. Having in mind the behavior of Bessel's functions depicted in fig. 2.6, an increase of  $eV_{AC}$  would initially decrease  $J_0(eV_{AC}/2\hbar\omega)$  and increase  $J_n(eV_{AC}/2\hbar\omega)$ . However, for a certain value of  $eV_{AC}/\hbar\omega$ , also the  $J_n$  would start to decrease, therefore reducing the intensity of the additional side peaks. As a consequence the current reduces after having reached a maximum. The oscillatory behavior that accompanies the decrease results from the oscillatory behavior of Bessel's functions. It is important to notice that the current can assume values lower than the corresponding dark current, but this information is not reliable, as said above, because this effect happens in the range of critical values of the electric field (orange area).

The general behavior predicted by Floquet is pretty similar, but with the main difference associated to the position of global and local maxima in  $I(U_{AC})$ . The decrease of the current predicted with Floquet can be justified again thinking about the time modulation of the energy levels. If  $U_{AC}$  is large enough, all the levels considered in the 0D model can be shifted far from the BW for a certain time interval during a single oscillation. This means that the time-averaged current can decrease, even to lower values of dark current if the levels spend most of the time outside the BW. Also in this case an oscillatory behavior is associated to the decrease of current, but the oscillation happens with a frequency that seems to be twice the one of TG current. The origin of this oscillation is not clear yet, but its double frequency seems to be related to the fact that in TG the argument of Bessel's functions is proportional to  $eV_{AC}/2$  while in Floquet the parameter used in the computation is  $U_{AC} = eV_{AC}$ .

Another observation concerning fig. 3.23 is that the convergence of Floquet is not guaranteed at large  $U_{AC}$ . In particular we can say that, for the chosen value of  $n_{max} = 16$ , the Floquet simulation converges for  $U_{AC} \lesssim 9 \text{ eV}$ . This means that the peak at 10 eV would change if the number of Floquet modes is increased. From the point of view of transmission probability, the non-convergent result corresponds to a spectrum whose side peaks are not located at the positions determined by  $n\hbar\omega$ , therefore the associated information is not reliable.

Talking about transmission spectrum, it is crucial to understand how it changes when the photon energy is fixed and the flux is varied. In fig. 3.24 I reported six transmission spectra corresponding to increasing values of  $U_{AC}$ , moving from panel (a) to panel (f), all computed with  $V_{DS} = 0.4 \text{ V}$  as applied bias. For a low value of  $U_{AC}$  as in (a), around 0.1 eV, the transmission spectrum is basically the same of EE-BESD since no sidebands are visible. At  $U_{AC} \approx 0.3 \text{ eV}$  (panel (b)), the additional peaks start to appear at distances  $\hbar\omega$  from the dark peaks, but without varying the transmission inside the BW. Further increasing  $U_{AC}$  to 0.5 eV

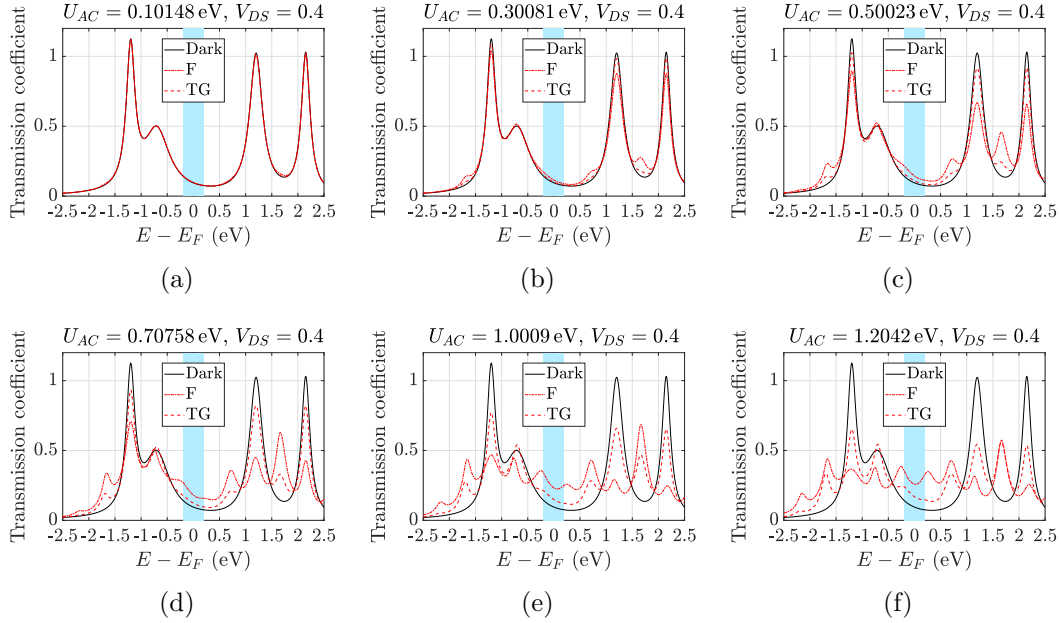


**Figure 3.24:** Transmission spectra of illuminated 3TT junction referred to a photon flux that increases from panel (a) to panel (f). The light-blue box corresponds to the BW determined by the applied bias  $V_{DS} = 0.4$  V.

induces an increase of the intensity of the sidebands, but also a clear increase of the transmission inside BW, that is related to a current amplification with respect to dark condition. Up to this point, multi-photon interactions are negligible. They start to be visible in panel (d) where  $U_{AC} \approx 0.7$  eV. This is clear by looking at the left hand side of the dark peak corresponding to level HOMO-1. Indeed, we can see a small peak distant  $2\hbar\omega$  from the dark peak. Further increasing  $U_{AC}$  would enhance multi-photon processes and additional peaks start to appear also in the rest of the spectrum, as shown in (e), whereas those referred to dark condition decreases. In particular panel (f) represents a situation for which the additional peaks and the dark ones have almost the same intensity.

To summarize, the important information that we can extrapolate from the transmission spectra is that the location of the sidebands are determined by the energy of the incident photons, whereas the intensity is related to the incident photon flux. Multi-photon processes acquire importance only for large enough fluxes and correspond to peaks distant  $n\hbar\omega$  ( $n > 2$ ) from those computed in dark conditions.

The discussion of the third simulation concludes the presentation of the example based on 3TT junction. This section can be considered as a guide to understand the results of EE-BESD-PAT, but also a starting point for future works on this

topic. What remains to do is to compare the simulations with others computed with more sophisticated approaches such as the one implemented in *QuantumATK*. Moreover, also a comparison with respect to experimental results is important to understand if EE-BESD-PAT can be used for fast prototyping of single-molecule optoelectronic devices.

### 3.3.3 Validation

The validation of EE-BESD-PAT is discussed in this section, starting from the comparison with *QuantumATK* and then moving to the experimental validation, done taking into account the measurements of Arielly *et al.* [20] on a SWMJ.

#### Comparison with QuantumATK

*QuantumATK* implements PAT through the first order Born approximation commented in section 2.4. This model allows to estimate the photocurrent component that is ‘linear’ with the incident photon flux. Since in *QuantumATK* it is only possible to simulate one bias at time for different photon energies, I have compared its result with the one of the EE-BESD-PAT simulation `hw_cycle`. Again a single-molecule junction based on 3TT placed between two gold atomic contacts, with orientation [1,1,1], is considered for the comparison. However, even if 3TT junction was already inside the EE-BESD library, I had to perform again *ab-initio* simulations of the electronic structure and of the *IV* curve of the junction for one main reason: I did not have the *ab-initio* simulations of the original work, therefore I could not compute the photocurrent. *QuantumATK* needs the electronic structure of the junction, computed with DFT, at the chosen bias in order to start the photocurrent simulation. As a consequence, I had to include a ‘new’ 3TT junction in EE-BESD, repeating the fitting procedure described in this chapter. For lack of time I have considered a non-optimized geometry of 3TT, but this should not be a problem because the same molecule is considered to compare EE-BESD-PAT with *QuantumATK*. For the DFT simulation of the electronic structure at equilibrium, I have used the LCAO calculator with the settings shown in table 3.3. Then, with the resulting electronic structure, I have computed the *IV* curve using the object “IVCharacteristics”. The setting for this simulation are shown in table 3.4. The transmission spectra for the chosen bias points are computed in addition to the *IV* curve and are used for the fitting procedure. In fig. 3.25(a) is shown in blue the current computed by *QuantumATK*, in red the one coming directly from the Lorentzian fitting of the peaks, while the yellow curve corresponds to the EE-BESD result. From the plots it is clear that the EE-BESD current departs from the *ab-initio* result in the range between 1 V and 2 V. This difference can be reduced improving the fitting, however this is not necessary because is enough to have

LCAO Basis Set	Exchange-correlation: GGA Functional: PBE Van der Waals correction: disabled Pseudopotential: FHI Basis set: DZP
Numerical Accuracy	Density mesh cut-off: 80 Hartree Occupation method: Fermi-Dirac Broadening: 1,000 K $k$ -points: Preset-Density [4.0,4.0,150.0] Å
Iteration Control	Default settings
Device Algorithm	Default settings
Contour Integral Parameter	Default settings
Poisson Solver	Solver type: Conjugate gradient Boundary conditions: (A) direction: Periodic Boundary condition (B) direction: Periodic Boundary condition (C) direction (transport): Dirichlet Boundary condition
Electrode Parameters	Default settings

**Table 3.3:** Settings used for the LCAO calculator to compute the electronic structure of 3TT junction at equilibrium.

$V_{DS}$ range	$V_0 = 0 \text{ V}$ , $V_1 = 3 \text{ V}$ Points: 11
Energy range	$E_0 = -2.5 \text{ eV}$ , $E_1 = 2.5 \text{ eV}$ Points: 151
$k$ -point grid	Density over (A) and (B) direction: [7.0,7.0] Å
Infinitesimal	1e-6 eV
Energy zero parameter	Average Fermi level
Self-energy calculator	Recursion

**Table 3.4:** Setting of “IVCharacteristics” object used to compute the  $IV$  curve of 3TT junction.

a bias point for which the current computed with EE-BESD is equal to the one of *QuantumATK*. Indeed for  $V_{DS} = 0.3\text{ V}$  the two curves are very close and the corresponding transmission spectra are shown in fig. 3.25(b). I have considered this bias for the computation of the photocurrent since the spectra are very similar and should allow to obtain the best comparison between EE-BESD-PAT and *QuantumATK*. To be more precise, the object “IVCharacteristics” does not store the

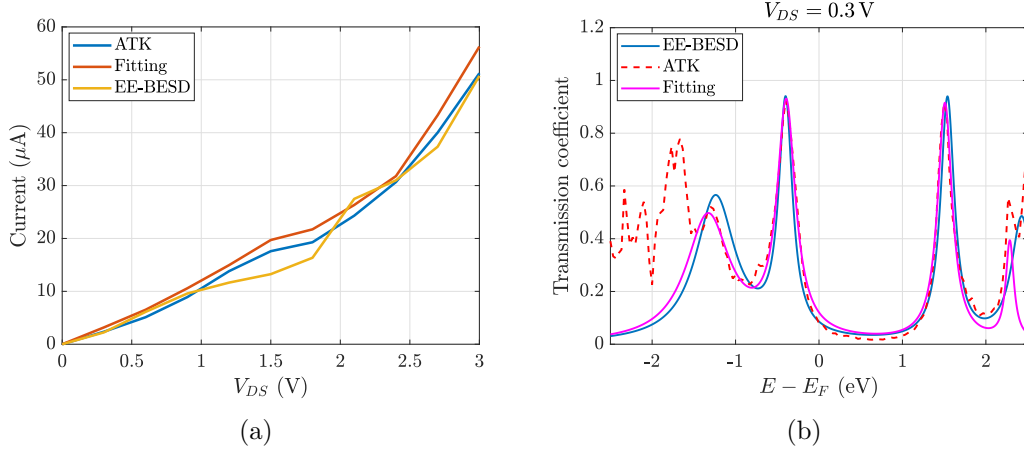


**Figure 3.25:** In panel (a) it is shown the comparison between the  $IV$  characteristics computed with *QuantumATK*, EE-BESD and the one obtained from the Lorentzian fitting. An example of the fitting procedure is depicted in panel (b) where it is shown the fitted transmission spectrum for  $V_{DS} = 0.3\text{ V}$ .

electronic configurations, at each bias point, that are needed as input to compute the photocurrent. Therefore I had to simulate the single bias point, corresponding to  $V_{DS} = 0.3\text{ V}$ , considering the same setting shown above. Then I computed the photocurrent considering the settings of “Photocurrent” object shown in table 3.5. For simplicity I have considered only the linear polarization parallel to transport

Energy range	$E_0 = -2.7\text{ eV}$ , $E_1 = 2.7\text{ eV}$ Points: 99
Photon energy	$E_0 = 0\text{ eV}$ , $E_1 = 2.5\text{ eV}$ Points: 20
$k$ -points grid	Grid type: MonkhorstPackGrid $n_a = 15$ , $n_b = 15$
Polarization	Linear-z [0,0,1]

**Table 3.5:** Settings of “Photocurrent” object considered to compute the current of the illuminated 3TT junction for different photon energies.

direction, that should correspond to maximum coupling between the incident field

and the junction. Setting the same photon energy range in EE-BESD-PAT, between 0 eV and 2.5 eV, we can compare the different models. The photon flux is set to  $1 \text{ \AA}^{-2} \text{ s}^{-1}$ , corresponding to the incidence of one photon per second over an area of  $1 \text{ \AA}^{-2}$ . This is the default setting of *QuantumATK* and a change in the flux corresponds only to a direct multiplication of the photocurrent by  $F_{ph}$  (remember that only the component linear with the flux is computed by *QuantumATK*). Since the shape remains the same, I left the default setting and compared the resulting photocurrent with the one of EE-BESD-PAT.

The computation of the photocurrent by *QuantumATK* took approximately six days to finish, that is far longer than the execution times commented in the previous section. Figure 3.26 shows the results computed with the three models. First of all is important to observe the order of magnitude of the photocurrent. It

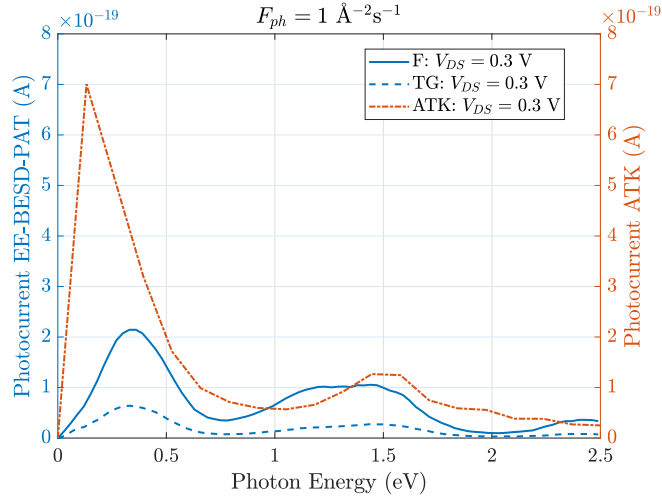


**Figure 3.26:** Comparison between the photocurrents computed with *QuantumATK*, Tien-Gordon and Floquet. The photon energy is varied between 0 eV and 2.5 eV while the photon flux is fixed to  $1 \text{ \AA}^{-2} \text{ s}^{-1}$ .

is the same for each model and equal to  $10^{-19} \text{ A}$ . This value is not strange if we focus on the chosen photon flux. Indeed only one photon per second reaches an area of  $1 \text{ \AA}^{-2}$ , located along the junction, where can interact with one electron in an energy state outside the BW. The interaction can lead the electron to move in a molecular orbital involved in conduction, hence increasing the total current. Considering typical dimensions of a single-molecule junction, only few photons per second can interact with a corresponding number of electrons, therefore the additional charge involved in conduction is a small multiple of the elementary charge, that is proportional to  $10^{-19} \text{ C}$ . This explains the small order of magnitude of the photocurrent. For what concerns the general behavior, the photocurrent of *QuantumATK* shows a peak at  $\hbar\omega = 1.5 \text{ eV}$  and another close to small values of

photon energy. It is likely that the former peak corresponds to absorption events involving electrons, with energy inside the BW, that can ‘jump’ to available states at  $\approx 1.5$  eV. Indeed, for this energy there is a peak in the Projected Device Density Of States (PDDOS), which is the projection of the total DOS of system over the device region, shown in fig. 3.27. The presence of a peak means that there is a local maximum of available states that can accept electrons after having absorbed a photon. The result is a peak in the photocurrent. On the other hand, the peak close to 0 eV should be considered with attention due to the low number (20) of photon energies used in the *ab-initio* simulation and due to possible problem of convergence depending on the considered number of  $k$ -points. A similar shape of the photocurrent is computed by TG and Floquet with the advantage of much faster simulations. The main difference is about the precise position of the peaks and their intensity. In these terms, Floquet performs better than TG, with the hope that, increasing the resolution in photon energy and the number of  $k$ -points of the *ab-initio* simulation, the difference of the peaks close to  $\hbar\omega = 0$  eV can become smaller than the one shown in this figure.

In general we can consider Floquet model as a good approximation of *QuantumATK* in the limit of small coupling between incident field and molecular junction. In future works a further analysis should be done to have more accurate *ab-initio* results for the comparison, but also to understand better the information associated to photon-mediated transmission spectra computed by *QuantumATK*, in order to compare them with the ones commented in the example of the previous section.

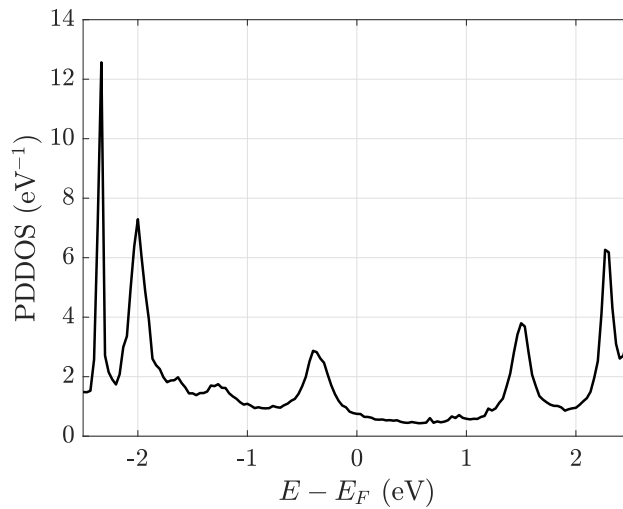


**Figure 3.27:** Projected Device Density Of States of the 3TT junction computed with *QuantumATK*.

### Comparison with experimental results

The second way to validate EE-BESD-PAT is to compare its simulations with some experimental measurement of photocurrent. In Chap. 1 it has been underlined that the number of experimental papers is much lower than the one referred to theoretical studies of PAT in single-molecule junctions. Nevertheless, there is a very well known experimental work that is always cited in the references of most recent papers. It is the work published in 2011 by Arielly and coworkers [20]: They measured the  $IV$  curve of a SWMJ, based on a SAM of octane (C8), when it is illuminated by a laser. This is one of the few article where the entire characteristic is measured under irradiation and not only a single bias point. This allows a full comparison between the results presented by Arielly and the `Vds_cycle` simulation of EE-BESD-PAT. Before showing the comparison, it is worth to describe more in

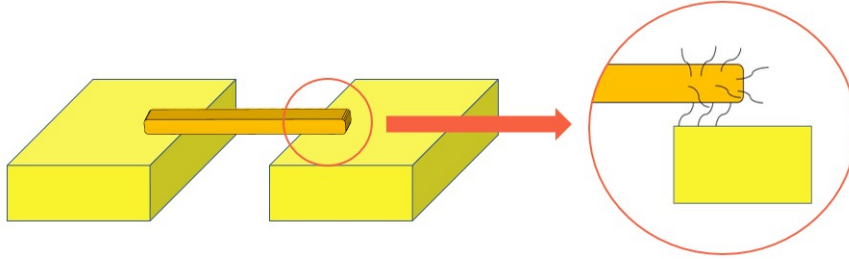


**Figure 3.28:** SWMJ based on C8-SAM that has been studied by Arielly *et al.* [20].

detail the experimental setup. The SWMJ considered by Arielly consists of two microscopic gold contacts connected by a gold nanorod. On the latter is deposited a C8-SAM, before the rod is manipulated through electrophoresis to bridge the two electrodes. Arielly *et al.* verified that a SAM-junction is established between only one end of the rod and one of the electrodes. A representation of the SWMJ can be seen in fig. 3.28. It is important to underline that the measured  $IV$  curve is referred to the SAM-junction. Therefore the current derives from the contributions of different single-molecule junctions, that could interact in some way and deviate the characteristic from the one of a single junction. What is sure is that the order of magnitude would be different with respect to the case of a single C8 placed between two atomic contacts.

Regarding the parameters of the incident radiation, they used a laser with the following specifications:

- $\hbar\omega = 1.89 \text{ eV} \rightarrow \lambda = 658 \text{ nm}$
- $P/A \approx 6.5 \text{ mW}/\mu\text{m}^2 = 6.5 \times 10^9 \text{ W/m}^2$

Since the chosen wavelength can excite surface plasmons, Arielly and coworkers measured the amplification of the field through eq. 2.41, that is generally valid for

junctions based on saturated molecules (for more details see section 2.2). Applying this formula they measured in ambient condition a local amplification of the field equal to  $k_{enh} \approx 550$ . In fig. 3.29 we can see that the field enhancement allows to have a large value of  $eV_{AC} \approx 1.87$  eV corresponding to an incident power density that is lower than the threshold imposed by the electrical breakdown. Starting

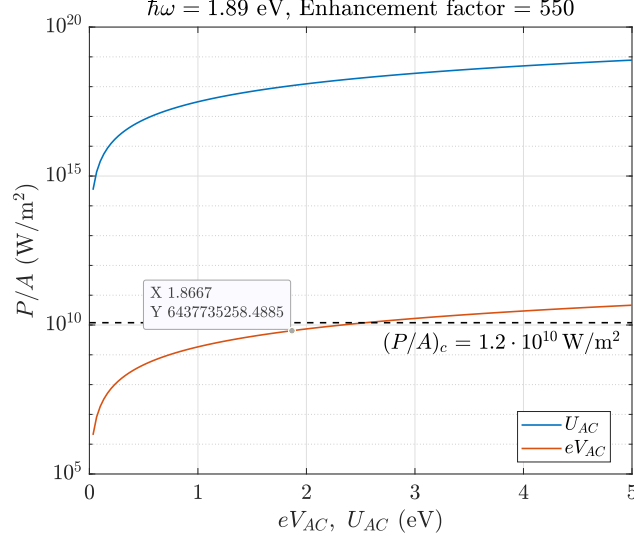


**Figure 3.29:** Incident power density as a function of the parameters  $U_{AC}$  and  $eV_{AC}$ . The field amplification is fixed to  $k_{enh} = 550$ . The shown data tip is referred to approximately the experimental incident power density.

from these quantities we can also compute the incident input flux used for the EE-BESD-PAT simulation, which is equal to  $F_{ph} = 2.147 \times 10^8 \text{ \AA}^{-2} \text{ s}^{-1}$ .

In fig. 3.30 I have reported the  $IV$  characteristics measured in dark and illumination conditions. It is clear that the current is amplified by the incident radiation. However the photocurrent contribution varies with the applied bias, in agreement with what said for the example of the previous section. To make a comparison with EE-BESD-PAT simulations, I had to include in the EE-BESD library the octane molecule. In this case I have first optimized the geometry of the molecule with *ORCA* considering the hybrid DFT functional CAM-B3LYP. The optimized length of the molecule is  $d_{mol} = 1.541$  nm. Then I used the optimized geometry in *QuantumATK* to simulate the  $IV$  curve of a single C8 junction between 0 V and 1.5 V, considering again 11 points. The settings to compute the electronic configuration at equilibrium with the LCAO calculator are the same of table 3.3. In this case I used the object “IVCurve” to compute the current since it allows to store the device configuration for each bias point. The settings of the object are shown in table 3.6. The next step was to fit the transmission spectra at each bias point. For the considered range of  $V_{DS}$ , I have found that three levels are enough

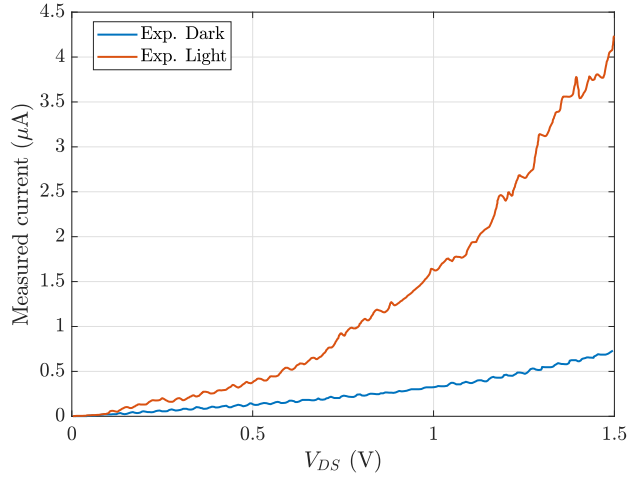


**Figure 3.30:**  $IV$  characteristics of the C8-SAM junction measured in dark and illumination conditions by Arielly and coworkers [20].

$V_{DS}$ range	$V_0 = 0 \text{ V}, V_1 = 1.5 \text{ V}$ Points: 11
Energy range	$E_0 = -4 \text{ eV}, E_1 = 4 \text{ eV}$ Points: 201
$k$ -point grid	Grid type: MonkhorstPackGrid $n_a = 7, n_b = 7$
Infinitesimal	1e-6 eV
Energy zero parameter	Average Fermi level
Self-energy calculator	Recursion

**Table 3.6:** Setting of “IVCurve” object used to compute the  $IV$  curve of C8 junction.

to have the best fitted spectra. Moreover, the fitting procedure was problematic due to the nature of C8. Since it is not a conjugated molecule, the HLG is very high ( $\approx 5.9 \text{ eV}$ ) and the transmission values inside the BW (large at most  $1.5 \text{ eV}$  around  $E_F$ ) are very small, in the order of  $10^{-3}$ . After several attempts, I obtained the EE-BESD current shown in yellow in fig. 3.31(a). The result is satisfying since there is an almost coincidence between the EE-BESD and the *ab-initio* simulation. For completeness I have reported in fig. 3.31(b) the comparison between the transmission spectra at equilibrium, that confirms again the good quality of the fitting procedure.

The next step was to perform the `Vds_cycle` simulation with EE-BESD-PAT

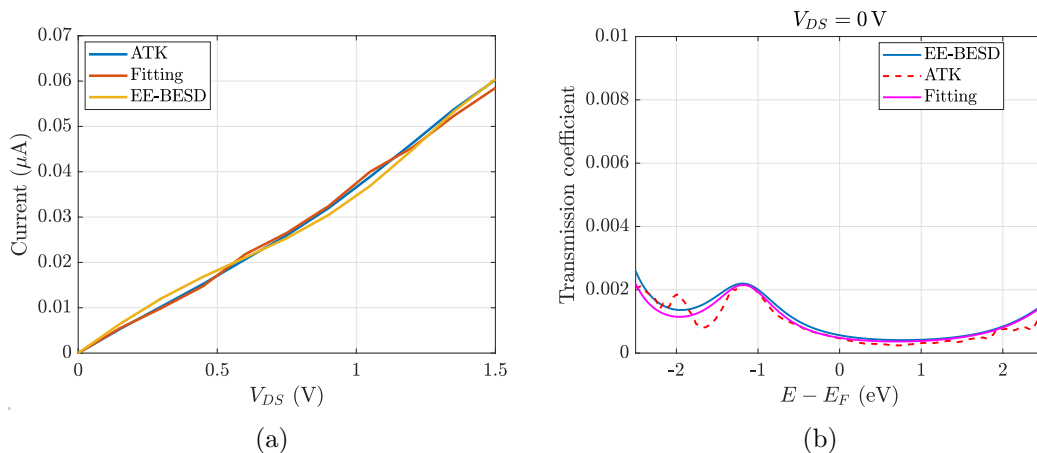


**Figure 3.31:** Comparison between the *ab-initio* and EE-BESD results for the single-molecule junction based on C8. In panel (a) it is evident that the EE-BESD characteristics well reproduce the one computed with *QuantumATK*. Instead in panel (b) it is reported a comparison between the transmission spectra computed at equilibrium. Also in this case EE-BESD gives a result in agreement with *QuantumATK*.

using the same optical parameters of the experiment. The results of the simulation are represented in fig. 3.32 where they are compared with the experimental measurements. Looking at the scales of the plot, we can immediately realize that the simulated current is one order of magnitude lower than that measured by Arielly. This can be justified by the fact that the SWMJ is not properly the system that is simulated by EE-BESD-PAT. As mentioned above, more molecular junctions contribute to the total current, therefore should not surprise that the measured *IV* curve is greater than the one simulated by EE-BESD-PAT. On the other hand, what surprises is the good agreement of the simulated dark current with the one measured by Arielly. The dependence on the applied bias is approximately the same, even if the experimental curve has a more exponential-like behavior, whereas the simulated dark current is more linear.

Concerning the characteristics in illumination condition, the current predicted by TG is not satisfying since the increase due to photocurrent is very small with a relative variation between 12% and 20% shown in fig. 3.32(b). Floquet performs better than TG, but the computed current amplification is still too small with respect to the experimental one. Moreover, its relative variation of current decreases with the applied bias, which is in net contrast with what seen in the experiment.

With the intention to reproduce the experimental result, I tried to change the amplification parameter  $k_{enh}$  that is used to determine the value of  $U_{AC}$ . In particular I considered it twice the original value, that means  $k_{enh} = 1100$ . This choice is not so arbitrary since the considered single-molecule junction is different

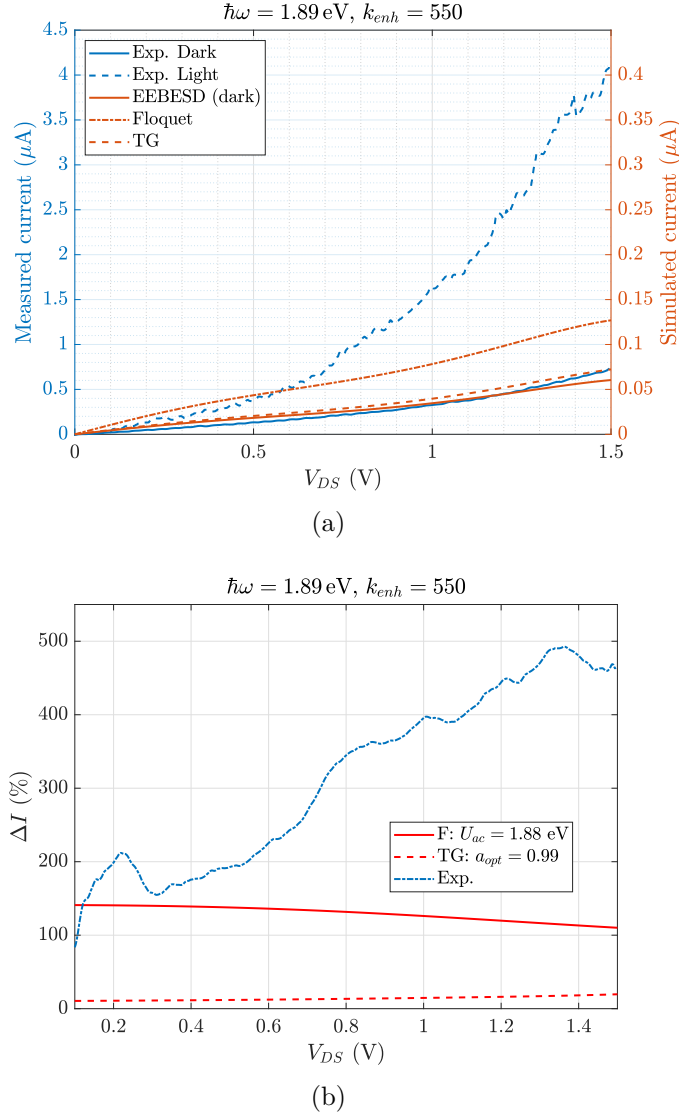


**Figure 3.32:** In panel (a) are depicted the experimental and simulated  $IV$  characteristics in dark and illumination condition for a molecular junction based on C8. The field amplification is fixed and equal to  $k_{enh} = 550$ . Panel (b) shows the relative variation of current, with respect to dark condition, depending on the applied bias.

from the experimental SWMJ, therefore it has a different plasmonic response. Moreover, the field amplification inside a dimer of gold NP can reach also  $10^3$  as order of magnitude, for an excitation wavelength corresponding to the surface plasmon resonance. Therefore a value of  $k_{enh} = 1100$  can be feasible under certain conditions. I repeated the simulation for this enhancement factor obtaining the results in fig. 3.33. There is an evident increase of the simulated photocurrent,

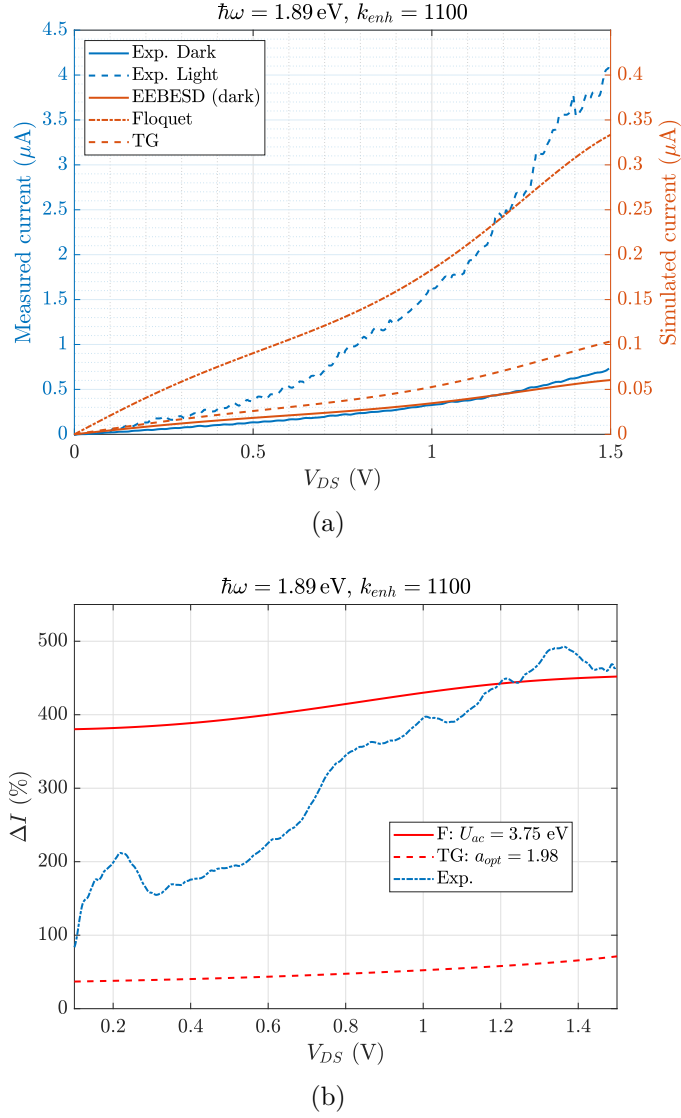


**Figure 3.33:** In panel (a) are depicted the experimental and simulated  $IV$  characteristics in dark and illumination condition for a molecular junction based on C8. The field amplification is fixed and equal to  $k_{enh} = 1100$ . Panel (b) shows the relative variation of current, with respect to dark condition, depending on the applied bias.

with a better agreement of Floquet current with the experimental one for larger voltages. In this case the relative variation for Floquet increases with  $V_{DS}$ , reaching a maximum amplification of approximately 460% at  $V_{DS} = 1.5 \text{ V}$ , that is very close to the experimental result.

This experimental validation confirms that EE-BESD-PAT (especially the Floquet model) can be used to obtain reasonable results when a ‘good’ enhancement

factor is included in the simulation. It can be interesting to develop a FDTD simulator that is able to compute the plasmonic response, taking in consideration the effects that the molecule can have on the plasmonic excitation, as it is done by Galperin *et al.* in [56].

# Chapter 4

## Conclusions

The idea behind this thesis work was to explore the interaction between light and single-molecule junctions. In Chap. 1 I have discussed the importance of studying this interaction. One reason is that light can be exploited as a tool to characterize process variability, which is especially problematic in molecular electronics. A brief introduction of Raman Spectroscopy is given since it is the most used technique to optically characterize a single-molecule junction. Another reason to study this field is that light can be used to control charge transport, giving birth to what is often called “molecular optoelectronics”. An incident electromagnetic radiation on a junction can influence transport properties in different ways. For example it can modify the geometry of the molecule supplying energy to activate an isomerization. This would change the coupling with the contacts and therefore also the current flowing through the molecule. The photoisomerization is at the base of the so called “photoswitches”. On the other hand, neglecting thermal effects, light can directly modulate the current through photo-assisted transport mechanisms which can be exploited for photovoltaic or detecting applications depending on the symmetry of the junction. Moreover, depending on the incident radiation wavelength, PAT can be divide in two types: adiabatic and resonant. In the former, only the energy of the electrons in the contacts is modulated by the incident field, without changing the occupation among the states, while the latter allows transitions between the molecular orbitals during tunneling. Also the excitation of LSP depends on the incident wavelength and must be taken in consideration due to the nanoscale dimensions of single-molecule junctions. Furthermore they can be exploited to locally enhance the electric field, therefore increasing the coupling between junction and electromagnetic field.

In Chap. 2 I commented in depth the three most used models in literature to analyze photo-assisted transport. The simplest and most used model in experimental papers is the one developed by P. K. Tien and J. P. Gordon in the context of superconductors and then adapted to single-molecule junctions. Due to its

simplicity, the model has some crucial problem, already underlined by Büttiker in 1998 [46]. A more complex approach based on NEGF is represented by the Floquet model. It is likely the most studied model to describe PAT in molecular junctions thanks to the review published in 2005 by P. Hänggi and coworkers [30]. The general idea is to exploit the time-periodicity of the Green's functions to solve the time-dependent problem through 'standard' techniques used for steady-state problems. This model has a complexity placed between the one of Tien-Gordon and the one of the Self-Consistent Born Approximation, which is the state-of-the-art technique to include the interaction between electrons and photons in the framework of NEGF theory. An introduction of the SCBA is given because the *ab-initio* software *QuantumATK* used in this work is based on first order Born approximation, that is the non-self-consistent version of SCBA.

Eventually, in Chap. 3 I presented the implementation of Tien-Gordon and Floquet starting from EE-BESD, which is an efficient and effective simulator of the *IV* curve of molecular junctions developed at Politecnico di Torino by the PhD candidate A. Zahir [41]. Using EE-BESD-PAT (the modified version of the original simulator) I have commented the simulation results for a 3TT junction in order to describe PAT and to give details on the limitations of the simulator. Then I tried to validate the approximated models, TG and Floquet, comparing their results with the ones of *QuantumATK* and with experimental measurements. In the end I can say that Floquet performs better than TG with reasonable execution times, much lower than those of *ab-initio* simulations. Moreover, choosing the proper simulation parameters, it can reproduce experimental results with a certain degree of reliability. This allows to think big and imagine to embed EE-BESD-PAT in a circuit level simulator for fast prototyping of 'molecular' photonic circuits. This can be the goal of a future work on this topic.

Another advantage of having implemented EE-BESD-PAT is that I rewritten EE-BESD in terms of non-equilibrium Green's functions, therefore others models based on NEGF could be implemented without too much effort. On the other hand, some works should be done to understand how the simulation parameter  $U_{AC}$  can be modeled in a more physical way. In particular, future works should focus on the analysis of the plasmonic response of the junction, including the effects that the molecule has on the field amplification. Furthermore, the polarization of the field should be taken into account when computing  $U_{AC}$ , hence it must be included in EE-BESD-PAT. Lastly, an additional study must be done to understand better the time-dependent approach adopted by M. Galperin in [49] and [56] used to study non time-periodic perturbation. This approach can be useful if we want to consider general optical input signals, but it is not clear yet if the execution time is short enough for fast design applications.

# Appendix A

## Dirac formalism

This appendix has the goal to briefly review Dirac formalism in order to understand better the reasoning of section 2.3. The following discussion is mainly based on the lectures notes of course “Quantum physics” taught by professor V. Penna in 2018 at Politecnico di Torino, but also on chapter 4 of Datta’s book [40].

In the Schrödinger picture of quantum mechanics the solutions of the Schrödinger equation, hence the wave functions, belong to the space of square integrable functions  $L^2(V)$  where  $V$  is the ambient space. Any normalized state of  $L^2(V)$  represents a wave function describing the initial state of a system or a possible physical state at some time  $t$ . Since the wave functions respect the properties of a linear space,  $L^2(V)$  has the structure of a vector space. Therefore, a linear combination of wave functions still belongs to  $L^2(V)$ , that means superposition principle is valid. Similarly to what is done in linear algebra, we can introduce a basis set of functions whose linear combinations allow to span the whole  $L^2(V)$ . To express a wave function in terms of basis functions is necessary to define a scalar product of the functions in  $L^2(V)$ . It assumes the following form:

$$(\psi, \phi) = \int_V \psi(\vec{x})^* \phi(\vec{x}) d\vec{x} \quad (\text{A.1})$$

Then a system of orthonormal functions  $\{\psi_k, k = 1, 2, \dots, \infty\}$  is defined by:

$$(\phi_n, \phi_i) = \int_V \phi_n(\vec{x})^* \phi_i(\vec{x}) d\vec{x} = \delta_{n,i} \quad (\text{A.2})$$

Note that a discrete index is considered for simplicity, even if it is also common to have physical systems described in terms of basis with a continuous index. A basis set is said complete if any function in  $L^2(V)$  can be represented in terms of its Fourier series obtained with the basis functions:

$$\psi(\vec{x}) = \sum_k c_k \phi_k(\vec{x}) \quad , \quad c_k = (\phi_k, \psi) \quad (\text{A.3})$$

Therefore each wave function can be identified with an infinite sequence of numbers  $c_1, c_2, \dots, c_n, \dots$  that can be viewed as the vectorial components of  $\psi$  with respect to the chosen basis set. This suggests that there exists a one to one correspondence between  $L^2(V)$  and an infinite-dimensional vector space, that is called Hilbert space ( $\mathbb{H}$ ), whose vectors have finite form and are defined over a complex field. This suggestion has been proved with the fundamental theorem of Fisher-Riesz. It states that given an arbitrarily chosen sequence  $c_1, c_2, \dots, c_n, \dots$ , such that

$$\sum_{k=0}^{\infty} |c_k|^2 < \infty \quad (\text{A.4})$$

it is a necessary and sufficient condition to ensure the existence of a function  $\psi \in L^2(V)$  or an equivalent ‘abstract’ vector  $|\psi\rangle \in \mathbb{H}$ , having projections over the elements of a complete orthonormal basis set equal to  $c_k$ .

$$\psi = \sum_k c_k \phi_k \quad \Leftrightarrow \quad |\psi\rangle = \sum_k c_k |k\rangle \quad (\text{A.5})$$

The vectors  $|k\rangle$  are basis vectors of the Hilbert space and are labeled by the corresponding index  $k$ . In the Dirac formalism physical states are represented by vectors in the Hilbert space since there is a direct correspondence with wave functions thanks to Fisher-Riesz theorem. The notation used to indicate vectors is a little different from the usual one. Infinite dimensional row vectors are called ‘bra’ and are indicated by  $\langle a|$ , while infinite dimensional column vectors are called ‘ket’ and are indicated by  $|b\rangle$ . Since they are defined over a complex field, the scalar product in  $\mathbb{H}$  is defined in this way exploiting the convention introduced by Dirac:

$$\langle a|b\rangle = \sum_k a_k^* b_k = (\psi_a, \psi_b) \quad (\text{A.6})$$

where the last equality represents the equivalence between the scalar product defined in  $\mathbb{H}$  with the one defined in  $L^2(V)$ . It is worth underline that a ket vector can be transformed in its dual bra form by doing

$$|a\rangle = \sum_k a_k |k\rangle \quad \Rightarrow \quad \langle a| = \sum_k a_k^* \langle k| \quad (\text{A.7})$$

For what concerns physical operators, in the Dirac picture they are represented by matrices. The matrix elements of a given operator  $\mathcal{O}$  are computed in the Schrödinger picture as:

$$\mathcal{O} \quad \Rightarrow \quad O_{ij} = (\phi_i, \mathcal{O}\phi_j) = \int_V \phi_i(\vec{x})^* \mathcal{O}\phi_j(\vec{x}) d\vec{x} \quad (\text{A.8})$$

With Dirac formalism the elements are indicated by  $O_{ij} = \langle i|\tilde{\mathcal{O}}|j\rangle$  whereas the associated matrix is formally indicated by

$$\tilde{\mathcal{O}} = \sum_i \sum_j |i\rangle O_{ij} \langle j| \quad \Rightarrow \quad (\text{A.9})$$

$$\langle i|\tilde{\mathcal{O}}|j\rangle = \langle i|\left(\sum_m \sum_n |m\rangle O_{mn} \langle n|\right)|j\rangle = \sum_m \sum_n \underbrace{\langle i|m\rangle}_{\delta_{i,m}} O_{mn} \underbrace{\langle n|j\rangle}_{\delta_{n,j}} = O_{ij} \quad (\text{A.10})$$

There are two important properties that relates physical operators with matrices:

- If the physical operator  $\mathcal{O}$  is Hermitian, the corresponding matrix  $\tilde{\mathcal{O}}$  is Hermitian, therefore corresponding eigenvalues are real.
- If the chosen basis functions are the eigenstates of  $\mathcal{O}$ , the corresponding matrix in this basis would be diagonal with entries equal to the eigenvalues of  $\mathcal{O}$ .

Another important consequence of using abstract vectors is that two vectors expressed in two independent bases,  $\mathcal{B}$  and  $\mathcal{B}'$ , correspond to the same physical state if their squared norm is equal:

$$\langle \psi|\psi\rangle = \sum_k |c_k|^2 = \sum_{k'} |c_{k'}|^2 = \langle \psi'|\psi'\rangle \quad (\text{A.11})$$

Therefore the vectors  $|\psi\rangle$  and  $|\psi'\rangle$  correspond to the same state even if expressed with different basis vectors. There exists a class of transformations, called unitary transformations, that allows to move from one basis to another, i.e. allows to change representation of vectors, preserving the norm. This ensures that the probabilistic interpretation is maintained even if the basis is changed. The mathematical object that connects the projections over a basis  $\mathcal{B}$  with the ones of a new basis  $\mathcal{B}'$  is a matrix that satisfies the unitary condition  $\tilde{S}\tilde{S}^\dagger = \tilde{S}^\dagger\tilde{S} = I$ , where  $\tilde{S}^\dagger$  is the adjoint (conjugate transpose) of  $\tilde{S}$  and  $I$  is the identity matrix. The elements of  $S$  represents the projection of the new basis vectors,  $|n'\rangle$ , over the old ones,  $|m\rangle$ , and are computed as

$$S_{mn'} = \langle m|n'\rangle \quad (\text{A.12})$$

Then, the new basis vectors can be expressed exploiting the unitary matrix

$$|n'\rangle = \sum_m S_{mn'} |m\rangle \quad (\text{A.13})$$

Exploiting this relation, is possible to transform the vector components of  $|\psi\rangle$  in the old basis  $\mathcal{B}$  into the ones of the new basis  $\mathcal{B}'$ .

$$c_{n'} = \sum_m S_{nm}^\dagger c_m \quad , \quad c_m = \sum_{n'} S_{mn'} c_{n'} \quad (\text{A.14})$$

Knowing how basis vectors and components change from one basis to another is possible to express the transformation of vector  $|\psi\rangle$ :

$$|\psi\rangle = \sum_m c_m |m\rangle = \sum_m \left( \sum_{n'} S_{mn'} c_{n'} \right) |m\rangle = \sum_{n'} c_{n'} \underbrace{\left( \sum_m S_{mn'} |m\rangle \right)}_{|n'\rangle} = \sum_{n'} c_{n'} |n'\rangle \quad (\text{A.15})$$

The transformation of vectors is said to have a covariant character since the transformation is the same of the basis vectors where the matrix  $\tilde{S}$  is directly involved.

Also physical operators change from one basis to another since the basis vectors used to compute the matrix elements are different. The elements in the new basis are obtained exploiting again eq. A.13:

$$O_{m'n'} = \langle m' | \tilde{O}' | n' \rangle = \sum_{i,j} \langle m' | i \rangle \langle i | \tilde{O} | j \rangle \langle j | n' \rangle \quad \Rightarrow \quad (\text{A.16})$$

$$\tilde{O}' = S^\dagger \tilde{O} S \quad (\text{A.17})$$

The discussion above supplies the main tools to deal with Dirac formalism and understand Floquet model described in section 2.3.

# Appendix B

## Proof of equation 2.122

The starting point to prove eq. 2.122 is the general expression of current when scattering mechanisms are considered. Indeed in these cases current exiting from the central region through contact  $\alpha$  is expressed by eq. 2.28, that is reported here below.

$$I_\alpha = \frac{2e}{h} \int_{-\infty}^{+\infty} \text{Tr}[\Sigma_\alpha^<(E)G^>(E) - \Sigma_\alpha^>(E)G^<(E)]dE$$

Since eq. 2.122 represents only the photocurrent due to absorption events, the first step is to rewrite the lesser and greater Green's function using equations 2.116, 2.117 and 2.118, that are the one implemented in *QuantumATK*. Since only absorption is considered, there would not be in the derivation terms proportional to  $N + 1$ .

Writing explicitly the interacting Green's functions, we can distinguish a term referred to the dark current and a term corresponding to photocurrent. Considering just the trace argument, it will change as follows (the energy dependence is not expressed for simplicity):

$$\Sigma_\alpha^<G^> - \Sigma_\alpha^>G^< = \tag{B.1}$$

$$\Sigma_\alpha^<[G_0^R(\Sigma_\alpha^> + \Sigma_{ph}^>)G_0^A] - \Sigma_\alpha^>[G_0^R(\Sigma_\alpha^< + \Sigma_{ph}^<)G_0^A] = \tag{B.2}$$

$$\Sigma_\alpha^<G_0^R\Sigma_\alpha^>G_0^A + \Sigma_\alpha^<G_0^R\Sigma_{ph}^>G_0^A - \Sigma_\alpha^>G_0^R\Sigma_\alpha^<G_0^A - \Sigma_\alpha^>G_0^R\Sigma_{ph}^<G_0^A = \tag{B.3}$$

$$\underbrace{\Sigma_\alpha^<G_0^> - \Sigma_\alpha^>G_0^<}_{I_{\alpha,dark}} + \underbrace{\Sigma_\alpha^<G_0^R\Sigma_{ph}^>G_0^A - \Sigma_\alpha^>G_0^R\Sigma_{ph}^<G_0^A}_{I_{\alpha,ph}} \tag{B.4}$$

It is clear that in the last equation the first two terms would be the trace argument to compute the dark current whereas the last two are the terms used to compute the photocurrent. The latter can be developed by expressing the self-energies  $\Sigma_{ph}^{\lessgtr}$  and  $\Sigma_\alpha^{\lessgtr}$  considering only absorption and exploiting fluctuation-dissipation theorem. For brevity, in the following I will indicate with  $E^\pm = E \pm \hbar\omega$  the energy shifted

by one energy quanta. Therefore the trace argument to compute the photocurrent becomes:

$$\Sigma_\alpha^<(E)G_0^R(E)\Sigma_{ph}^>(E)G_0^A(E) - \Sigma_\alpha^>(E)G_0^R(E)\Sigma_{ph}^<(E)G_0^A(E) \quad (\text{B.5})$$

$$\begin{aligned} & i f_\alpha(E)\Gamma_\alpha(E)G_0^R(E)\left[NM^\dagger G_0^>(E^+)M\right]G_0^A(E) - \\ & i(f_\alpha(E) - 1)\Gamma_\alpha(E)G_0^R(E)\left[NMG_0^<(E^-)M^\dagger\right]G_0^A(E) = \end{aligned} \quad (\text{B.6})$$

$$\begin{aligned} & i f_\alpha(E)\Gamma_\alpha(E)G_0^R(E)\left[NM^\dagger G_0^>(E^+)M\right]G_0^A(E) - \\ & i(f_\alpha(E) - 1)\Gamma_\alpha(E)G_0^R(E)\left[NMG_0^<(E^-)M^\dagger\right]G_0^A(E) \end{aligned} \quad (\text{B.7})$$

Now, expressing the non-interacting  $G_0^{\lessgtr}$  we would be able to identify the spectral function and its time reversed version. Moreover,  $G_0^{\lessgtr}$  will depend to both contacts since it is related to  $\Sigma_C^{\lessgtr} = \Sigma_{C1}^{\lessgtr} + \Sigma_{C2}^{\lessgtr}$ . Instead of writing everything, a summation over contact  $\beta \in \{C1, C2\}$  is inserted.

$$\begin{aligned} & i f_\alpha(E)\Gamma_\alpha(E)G_0^R(E)NM^\dagger \left[ \sum_{\beta \in \{C1, C2\}} G_0^R(E^+)\Sigma_\beta^>(E^+)G_0^A(E^+) \right] MG_0^A(E) - \\ & i(f_\alpha(E) - 1)\Gamma_\alpha(E)G_0^R(E)NM \left[ \sum_{\beta \in \{C1, C2\}} G_0^R(E^-)\Sigma_\beta^<(E^-)G_0^A(E^-) \right] M^\dagger G_0^A(E) = \end{aligned} \quad (\text{B.8})$$

$$\begin{aligned} & i f_\alpha(E)\Gamma_\alpha(E)G_0^R(E)NM^\dagger \left[ \sum_{\beta \in \{C1, C2\}} G_0^R(E^+)i(f_\beta(E^+) - 1)\Gamma_\beta(E^+)G_0^A(E^+) \right] MG_0^A(E) - \\ & i(f_\alpha(E) - 1)\Gamma_\alpha(E)G_0^R(E)NM \left[ \sum_{\beta \in \{C1, C2\}} G_0^R(E^-)i f_\beta(E^-)\Gamma_\beta(E^-)G_0^A(E^-) \right] M^\dagger G_0^A(E) = \end{aligned} \quad (\text{B.9})$$

Moving the summation over  $\beta$  at the beginning and using the minus sign coming from  $i^2$ , we can rewrite the trace argument. Moreover, exploiting the invariance of trace for cyclic permutations, we can move  $\Gamma_\alpha(E)$  and  $G_0^R(E)$  at the end on the argument. The final result is the following:

$$\begin{aligned} & \sum_{\beta \in \{C1, C2\}} \left[ f_\alpha(E)(1 - f_\beta(E^+))NM^\dagger \underbrace{G_0^R(E^+)\Gamma_\beta(E^+)G_0^A(E^+)}_{A_\beta(E^+)} M \underbrace{G_0^A(E)\Gamma_\alpha(E)G_0^R(E)}_{\tilde{A}_\alpha(E)} - \right. \\ & \left. (1 - f_\alpha(E))f_\beta(E^-)NM \underbrace{G_0^R(E^-)\Gamma_\beta(E^-)G_0^A(E^-)}_{A_\beta(E^-)} M^\dagger \underbrace{G_0^A(E)\Gamma_\alpha(E)G_0^R(E)}_{\tilde{A}_\alpha(E)} \right] \end{aligned} \quad (\text{B.10})$$

In the equation above we have identified the spectral functions that are expressed in eq. 2.122. The last step is to define the transmission coefficients  $T_{\alpha, \beta}^\pm$ . This is now

easy since is enough to put inside the trace operator what we have just derived.

$$T_{\alpha,\beta}^+(E) = N \text{Tr} \left[ M^\dagger A_\beta(E^+) M \tilde{A}_\alpha(E) \right] \quad (\text{B.11})$$

$$T_{\alpha,\beta}^-(E) = N \text{Tr} \left[ M A_\beta(E^-) M^\dagger \tilde{A}_\alpha(E) \right] \quad (\text{B.12})$$

Lastly, we can use these transmission coefficients to evaluate the photocurrent:

$$I_{\alpha,ph} = \frac{2e}{\hbar} \int_{-\infty}^{+\infty} \sum_{\beta \in \{C1, C2\}} f_\alpha(E) [1 - f_\beta(E^+)] T_{\alpha,\beta}^+(E) - [1 - f_\alpha(E)] f_\beta(E^-) T_{\alpha,\beta}^-(E) dE \quad (\text{B.13})$$

The sign of the two terms are opposite with respect to eq. 2.122 because I have assumed an opposite convention. Here the current is going from the device region towards the contact whereas in eq. 2.122 the current is going from the contact to the central region. However, the magnitude of the induced photocurrent is the same and this concludes the proof of eq. 2.122.



# Bibliography

- [1] R. P. Feynman. «There's Plenty of Room at the Bottom». In: Talk at the Annual Meeting of the American Physical Society at Caltech. 1959. URL: <https://web.archive.org/web/20070427214433/http://www.its.caltech.edu/~feynman/plenty.html> (cit. on p. 1).
- [2] F. Mo. «Molecular Electronic Sensors Modeling: From Theory to Applications». M. Eng. thesis. Torino, Italy: Politecnico di Torino, Oct. 2020 (cit. on pp. 1, 2).
- [3] M. Galperin and A. Nitzan. «Molecular optoelectronics: the interaction of molecular conduction junctions with light». In: *Phys. Chem. Chem. Phys.* 14 (26 2012), pp. 9421–9438. DOI: 10.1039/C2CP40636E (cit. on pp. 3, 4, 13, 21).
- [4] S. Kaneko et al. «Site-Selection in Single-Molecule Junction for Highly Reproducible Molecular Electronics». In: *Journal of the American Chemical Society* 138.4 (2016), pp. 1294–1300. DOI: 10.1021/jacs.5b11559 (cit. on p. 8).
- [5] S. Kaneko, K. Yasuraoka, and M. Kiguchi. «Bias Voltage Induced Surface-Enhanced Raman Scattering Enhancement on the Single-Molecule Junction». In: *The Journal of Physical Chemistry C* 123.11 (2019), pp. 6502–6507. DOI: 10.1021/acs.jpcc.8b11595 (cit. on p. 8).
- [6] H. Bi et al. «Voltage-Driven Conformational Switching with Distinct Raman Signature in a Single-Molecule Junction». In: *Journal of the American Chemical Society* 140.14 (2018), pp. 4835–4840. DOI: 10.1021/jacs.7b12818 (cit. on p. 8).
- [7] H. Bi et al. «Optically Induced Molecular Logic Operations». In: *ACS Nano* 14.11 (2020), pp. 15248–15255. DOI: 10.1021/acsnano.0c05513 (cit. on p. 9).
- [8] D. Dulic', S. J. van der Molen, et al. «One-Way Optoelectronic Switching of Photochromic Molecules on Gold». In: *Phys. Rev. Lett.* 91.20 (Nov. 2003), p. 207402. DOI: 10.1103/PhysRevLett.91.207402 (cit. on pp. 9–11).

- [9] Y. Kim. «Photoswitching Molecular Junctions: Platforms and Electrical Properties». In: *ChemPhysChem* 21.21 (2020), pp. 2368–2383. DOI: 10.1002/cphc.202000564 (cit. on pp. 10, 11).
- [10] L. Chen, A. Feng, M. Wang, et al. «Towards single-molecule optoelectronic devices». In: *Sci. China Chem.* 61 (July 2018), pp. 1368–1384. DOI: 10.1007/s11426-018-9356-2 (cit. on pp. 10, 11, 18, 21, 31).
- [11] J. Zhang and H. Tian. «The Endeavor of Diarylethenes: New Structures, High Performance, and Bright Future». In: *Advanced Optical Materials* 6.6 (2018), p. 1701278. DOI: 10.1002/adom.201701278 (cit. on pp. 11–13).
- [12] S. Osella, P. Samorì, and J. Cornil. «Photoswitching Azobenzene Derivatives in Single Molecule Junctions: A Theoretical Insight into the I/V Characteristics». In: *The Journal of Physical Chemistry C* 118.32 (2014), pp. 18721–18729. DOI: 10.1021/jp504582a (cit. on p. 11).
- [13] Wikipedia contributors. *Diarylethene* — *Wikipedia, The Free Encyclopedia*. [Online; accessed 15-Sep-2021]. July 2021. URL: <https://en.wikipedia.org/wiki/Diarylethene> (cit. on p. 11).
- [14] J. Huang, Q. Li, H. Ren, H. Su, Q. W. Shi, and J. Yang. «Switching mechanism of photochromic diarylethene derivatives molecular junctions». In: *The Journal of Chemical Physics* 127.9 (2007), p. 094705. DOI: 10.1063/1.2770733 (cit. on p. 11).
- [15] X. Zhang, L. Hou, and P. Samorì. «Coupling carbon nanomaterials with photochromic molecules for the generation of optically responsive materials». In: *Nature Communications* 7.11118 (2016), p. 1701278. DOI: 10.1038/ncomms11118 (cit. on pp. 11, 13).
- [16] C. Jia et al. «Conductance Switching and Mechanisms in Single-Molecule Junctions». In: *Angewandte Chemie International Edition* 52.33 (2013), pp. 8666–8670. DOI: 10.1002/anie.201304301 (cit. on p. 12).
- [17] Q.-H. Wu, P. Zhao, and D.-S. Liu. «Electronic Transport of a Molecular Photoswitch with Graphene Nanoribbon Electrodes». In: *Chinese Physics Letters* 31.05 (2014), p. 057304. DOI: 10.1088/0256-307X/31/5/057304 (cit. on p. 12).
- [18] C. Jia, A. Migliore, N. Xin, S. Huang, et al. «Covalently bonded single-molecule junctions with stable and reversible photoswitched conductivity». In: *Science* 352.6292 (June 2016), pp. 1443–1445. DOI: 10.1126/science.aaf6298 (cit. on p. 12).

- [19] E. Orgiu and P. Samorì. «25th Anniversary Article: Organic Electronics Marries Photochromism: Generation of Multifunctional Interfaces, Materials, and Devices». In: *Advanced Materials* 26.12 (2014), pp. 1827–1845. DOI: 10.1002/adma.201304695 (cit. on p. 13).
- [20] R. Arielly, A. Ofarim, G. Noy, and Y. Selzer. «Accurate Determination of Plasmonic Fields in Molecular Junctions by Current Rectification at Optical Frequencies». In: *Nano Letters* 11.7 (2011), pp. 2968–2972. DOI: 10.1021/nl201517k (cit. on pp. 14, 29, 56, 87, 117, 122, 124).
- [21] E. Fung et al. «Too Hot for Photon-Assisted Transport: Hot-Electrons Dominate Conductance Enhancement in Illuminated Single-Molecule Junctions». In: *Nano Letters* 17.2 (2017), pp. 1255–1261. DOI: 10.1021/acs.nanolett.6b05091 (cit. on pp. 14, 20, 57).
- [22] D. Kos, D. R. Assumpcao, C. Guo, and J. J. Baumberg. «Quantum Tunneling Induced Optical Rectification and Plasmon-Enhanced Photocurrent in Nanocavity Molecular Junctions». In: *ACS Nano* 15.9 (2021), pp. 14535–14543. DOI: 10.1021/acsnano.1c04100 (cit. on pp. 14, 28, 99).
- [23] Wikipedia contributors. *Localized surface plasmon* — *Wikipedia, The Free Encyclopedia*. [Online; accessed 29-October-2021]. Jan. 2021. URL: [https://en.wikipedia.org/w/index.php?title=Localized\\_surface\\_plasmon&oldid=1002479206](https://en.wikipedia.org/w/index.php?title=Localized_surface_plasmon&oldid=1002479206) (cit. on p. 15).
- [24] M. Brongersma, N. Halas, and P. Nordlander. «Plasmon-induced hot carrier science and technology». In: *Nature Nanotech* 10 (2015), pp. 25–34. DOI: 10.1038/nnano.2014.311 (cit. on pp. 15, 16).
- [25] J.-C. Lacroix et al. «From active plasmonic devices to plasmonic molecular electronics». In: *Polymer International* 68.4 (2019), pp. 607–619. DOI: 10.1002/pi.5756 (cit. on p. 15).
- [26] P. Reddy, S.-Y. Jang, R. A. Segalman, and A. Majumdar. «Thermoelectricity in Molecular Junctions». In: *Science* 315.5818 (Mar. 2007), pp. 1568–1571. DOI: 10.1126/science.1137149 (cit. on p. 20).
- [27] P. K. Tien and J. P. Gordon. «Multiphoton Process Observed in the Interaction of Microwave Fields with the Tunneling between Superconductor Films». In: *Phys. Rev.* 129.2 (Jan. 1963), pp. 647–651. DOI: 10.1103/PhysRev.129.647 (cit. on p. 21).
- [28] J. C. Cuevas and E. Scheer. *Molecular Electronics: An introduction to Theory and Experiment*. World Scientific Publishing Co. Pte. Ltd., 2010. Chap. 8, 20, Appendix A (cit. on pp. 21, 32, 51).

- [29] Y. Selzer. «Elucidating the Contributions of Plasmon-Induced Excitons and Hot Carriers to the Photocurrent of Molecular Junctions». In: *The Journal of Physical Chemistry C* 124.16 (2020), pp. 8680–8688. DOI: 10.1021/acs.jpcc.0c02196 (cit. on pp. 23, 24).
- [30] S. Kohler, J. Lehmann, and P. Hänggi. «Driven quantum transport on the nanoscale». In: *Physics Reports* 406.6 (2005), pp. 379–443. DOI: 10.1016/j.physrep.2004.11.002 (cit. on pp. 24–26, 28, 33, 58, 61–63, 65, 67, 74, 130).
- [31] M. R. Mazon. «Coherent control of charge and heat transport in semiconductor nanostructures». PhD thesis. Madrid: Universidad autonoma de Madrid, June 2006. URL: [https://repositorio.uam.es/bitstream/handle/10486/2627/1457\\_rey\\_mazon.pdf?sequence=1&isAllowed=y](https://repositorio.uam.es/bitstream/handle/10486/2627/1457_rey_mazon.pdf?sequence=1&isAllowed=y) (cit. on p. 28).
- [32] G. Noy, A. Ophir, and Y. Selzer. «Response of Molecular Junctions to Surface Plasmon Polaritons». In: *Angewandte Chemie International Edition* 49.33 (2010), pp. 5734–5736. DOI: 10.1002/anie.201000972 (cit. on p. 29).
- [33] M. Vadai et al. «Plasmon-Induced Conductance Enhancement in Single-Molecule Junctions». In: *The Journal of Physical Chemistry Letters* 4.17 (2013), pp. 2811–2816. DOI: 10.1021/jz4014008 (cit. on p. 29).
- [34] S. K. Saxena, U. M. Tefashe, M. Supur, and R. L. McCreery. «Evaluation of Carbon Based Molecular Junctions as Practical Photosensors». In: *ACS Sensors* 6.2 (2021), pp. 513–522. DOI: 10.1021/acssensors.0c02183 (cit. on p. 29).
- [35] T. Wang and C. A. Nijhuis. «Molecular electronic plasmonics». In: *Applied Materials Today* 3 (2016), pp. 73–86. DOI: 10.1016/j.apmt.2016.03.001 (cit. on p. 30).
- [36] G. Reecht, F. Scheurer, V. Speisser, Y. J. Dappe, F. Mathevet, and G. Schull. «Electroluminescence of a Polythiophene Molecular Wire Suspended between a Metallic Surface and the Tip of a Scanning Tunneling Microscope». In: *Phys. Rev. Lett.* 112.4 (Jan. 2014), p. 047403. DOI: 10.1103/PhysRevLett.112.047403 (cit. on p. 31).
- [37] N. L. Schneider, J. T. Lü, M. Brandbyge, and R. Berndt. «Light Emission Probing Quantum Shot Noise and Charge Fluctuations at a Biased Molecular Junction». In: *Phys. Rev. Lett.* 109.18 (Oct. 2012), p. 186601. DOI: 10.1103/PhysRevLett.109.186601 (cit. on p. 32).
- [38] S. Kohler, J. Lehmann, and P. Hänggi. «Controlling currents through molecular wires». In: *Superlattices and Microstructures* 34.3 (2003), pp. 419–427. DOI: 10.1016/j.spmi.2004.03.038 (cit. on p. 33).

- [39] U. Peskin and M. Galperin. «Coherently controlled molecular junctions». In: *The Journal of Chemical Physics* 136.4 (2012), p. 044107. DOI: 10.1063/1.3676047 (cit. on p. 33).
- [40] S. Datta. *Quantum Transport: Atom to Transistor*. Cambridge University Press, 2005 (cit. on pp. 36, 131).
- [41] A. Zahir, A. Demarchi, et al. «EE-BESD: molecular FET modeling for efficient and effective nanocomputing design». In: *Journal of Computational Electronics* 15 (2016), pp. 479–491. DOI: 10.1007/s10825-015-0777-y (cit. on pp. 44, 87, 130).
- [42] J. K. Viljas and J. C. Cuevas. «Role of electronic structure in photoassisted transport through atomic-sized contacts». In: *Physical Review B* 75.7 (Feb. 2007). DOI: 10.1103/physrevb.75.075406 (cit. on pp. 49, 54).
- [43] J. K. Viljas, F. Pauly, and J. C. Cuevas. «Photoconductance of organic single-molecule contacts». In: *Phys. Rev. B* 76.3 (July 2007), p. 033403. DOI: 10.1103/PhysRevB.76.033403 (cit. on p. 49).
- [44] C. Oppenländer. «Time-dependent density functional tight binding combined with the Liouville-von Neumann equation applied to AC transport in molecular electronics». PhD thesis. Regensburg: Universität Regensburg, Oct. 2014. URL: [https://epub.uni-regensburg.de/31257/1/Dissertation\\_Oppenl%C3%A4nder.pdf](https://epub.uni-regensburg.de/31257/1/Dissertation_Oppenl%C3%A4nder.pdf) (cit. on pp. 50, 55).
- [45] J. R. Tucker and M. J. Feldman. «Quantum detection at millimeter wavelengths». In: *Rev. Mod. Phys.* 57.4 (Oct. 1985), pp. 1055–1113. DOI: 10.1103/RevModPhys.57.1055 (cit. on pp. 52, 53).
- [46] M. H. Pedersen and M. Büttiker. «Scattering theory of photon-assisted electron transport». In: *Physical Review B* 58.19 (Nov. 1998), pp. 12993–13006. DOI: 10.1103/physrevb.58.12993 (cit. on pp. 60, 130).
- [47] A. Tikhonov, R. D. Coalson, and Y. Dahnovsky. «Calculating electron transport in a tight binding model of a field-driven molecular wire: Floquet theory approach». In: *The Journal of Chemical Physics* 116.24 (2002), pp. 10909–10920. DOI: 10.1063/1.1448292 (cit. on p. 62).
- [48] M. Genske. «Periodically driven many-body quantum systems. Quantum Ratchets, Topological States and the Floquet-Boltzmann Equation». PhD thesis. Köln: Univ. of Cologne, July 2017. URL: [https://kups.ub.uni-koeln.de/7822/1/thesis\\_final\\_A4.pdf](https://kups.ub.uni-koeln.de/7822/1/thesis_final_A4.pdf) (cit. on pp. 62, 65).
- [49] M. Sukharev and M. Galperin. «Transport and optical response of molecular junctions driven by surface plasmon polaritons». In: *Phys. Rev. B* 81.16 (Apr. 2010), p. 165307. DOI: 10.1103/PhysRevB.81.165307 (cit. on pp. 63, 75, 130).

- 
- [50] G. Cabra, I. Franco, and M. Galperin. «Optical properties of periodically driven open nonequilibrium quantum systems». In: *The Journal of Chemical Physics* 152.9 (2020), p. 094101. DOI: 10.1063/1.5144779 (cit. on p. 64).
- [51] L.-Y. H. and H. Rabitz. *Electron transport through a single-molecule junction with multiple pathways under time-periodic fields: A Floquet-scattering formalism*. 2014. arXiv: 1401.4222 [cond-mat.mes-hall] (cit. on p. 68).
- [52] L.-Y. Hsu and H. Rabitz. «Coherent light-driven electron transport through polycyclic aromatic hydrocarbon: laser frequency, field intensity, and polarization angle dependence». In: *Phys. Chem. Chem. Phys.* 17 (32 2015), pp. 20617–20629. DOI: 10.1039/C5CP02663F (cit. on p. 68).
- [53] B. Gu and I. Franco. «Optical absorption properties of laser-driven matter». In: *Phys. Rev. A* 98.6 (Dec. 2018), p. 063412. DOI: 10.1103/PhysRevA.98.063412 (cit. on p. 68).
- [54] D. F. Martinez. «Floquet–Green function formalism for harmonically driven Hamiltonians». In: *Journal of Physics A: Mathematical and General* 36.38 (Sept. 2003), pp. 9827–9842. DOI: 10.1088/0305-4470/36/38/302 (cit. on pp. 68, 70).
- [55] G. Stefanucci, S. Kurth, A. Rubio, and E. K. U. Gross. «Time-dependent approach to electron pumping in open quantum systems». In: *Phys. Rev. B* 77.7 (Feb. 2008), p. 075339. DOI: 10.1103/PhysRevB.77.075339 (cit. on pp. 68, 71, 74, 92, 98).
- [56] Alexander J. White, Maxim Sukharev, and Michael Galperin. «Molecular nanoplasmonics: Self-consistent electrostatics in current-carrying junctions». In: *Phys. Rev. B* 86.20 (Nov. 2012), p. 205324. DOI: 10.1103/PhysRevB.86.205324 (cit. on pp. 75, 128, 130).
- [57] *QuantumATK S-2021.06 Documentation*. Synopsys. 2021. URL: <https://docs.quantumatk.com/manual/manual.html> (cit. on pp. 75, 81).
- [58] L. E. Henrickson. «Nonequilibrium photocurrent modeling in resonant tunneling photodetectors». In: *Journal of Applied Physics* 91.10 (2002), pp. 6273–6281. DOI: 10.1063/1.1473677 (cit. on pp. 75, 84).
- [59] J. Chen, Y. Hu, and H. Guo. «First-principles analysis of photocurrent in graphene *PN* junctions». In: *Phys. Rev. B* 85.15 (Apr. 2012), p. 155441. DOI: 10.1103/PhysRevB.85.155441 (cit. on p. 75).
- [60] L. Zhang et al. «Generation and transport of valley-polarized current in transition-metal dichalcogenides». In: *Phys. Rev. B* 90.19 (Nov. 2014), p. 195428. DOI: 10.1103/PhysRevB.90.195428 (cit. on pp. 75, 82).

- [61] M. Palsgaard, T. Markussen, T. Gunst, M. Brandbyge, and K. Stokbro. «Efficient First-Principles Calculation of Phonon-Assisted Photocurrent in Large-Scale Solar-Cell Devices». In: *Physical Review Applied* 10.1 (July 2018). ISSN: 2331-7019. DOI: 10.1103/physrevapplied.10.014026 (cit. on pp. 75, 84).
- [62] M. Palsgaard et al. «Stacked Janus Device Concepts: Abrupt pn-Junctions and Cross-Plane Channels». In: *Nano Letters* 18.11 (2018), pp. 7275–7281. DOI: 10.1021/acs.nanolett.8b03474 (cit. on pp. 75, 84).
- [63] U. Aeberhard. «A microscopic theory of quantum well photovoltaics». PhD thesis. Zürich: ETH, 2008. URL: <https://www.research-collection.ethz.ch/handle/20.500.11850/150994> (cit. on pp. 75, 77).
- [64] J. K. Viljas, F. Pauly, and J. C. Cuevas. «Modeling elastic and photoassisted transport in organic molecular wires: Length dependence and current-voltage characteristics». In: *Phys. Rev. B* 77.15 (Apr. 2008), p. 155119. DOI: 10.1103/PhysRevB.77.155119 (cit. on p. 99).